The assessment of chemical short range order in multi-principal element alloys using total scattering

Benjamin E. Jolly

Department of Materials Science and Engineering, Centre for Doctoral Training in Advanced Metallic Systems

University of Sheffield

May 13, 2026

'It is a truth universally acknowledged, that a single phase solid solution in possession of a good number of constituent elements, must be in want of atomic ordering.'

B. E. Jolly

Acknowledgements

It is a rare and wonderful thing to have the opportunity to acknowledge so many people for their respective roles in my life. If I were to take nothing else from this experience, their support would be more than enough.

I owe, of course, an enormous debt of gratitude to my supervisors and mentors for their guidance over the four years of my doctoral research. Lewis - thank you for your genuine engagement with my work, your care and consideration in my lowest moments, and your near-boundless scientific enthusiasm. The uncountable hours perched in meeting rooms discussing the rotations of points in space made all of the work in this thesis feel much less daunting. Kathy - without your original suggestion that I could even attempt a PhD (never mind succeed in attaining one) I can confidently say that I would never have believed myself capable of producing this work. Your support has continued beyond the pages of this thesis, and I consider myself all the more fortunate for it.

To those lucky few blessed with the opportunity to share an office with me, I owe an apology: I'm sure that your work would have been much more fruitful without my endless verbal nonsense. But to all of you, I owe an equal thanks: to Fran - for keeping me grounded, for the camaraderie, and for reminding me that life existed outside of the walls of H6; to Josh - for the laughs, the football chatter, and the opportunity to throw my code at someone else for my own peace of mind; to Matt - for the kindness, a sofa to sleep on, and somehow allowing me to return home in one piece after sharing many, many hours of beam-time; and to Mimi - for the motivational speeches, the generosity, and the lunch time inspiration. I'm not sure that I can fully express how much the support from all of you has kept me going.

Beyond the confines of the Hadfield Building, I also want to express a brief thank you to the Sheffield community that kept me moving: to Mike - for our early-morning gym sessions, which will never be surpassed; to Jacob - for being the wittiest verbal sparring partner, even when I needed a lighter touch; and to Will - for your compassion, and your generosity. Without you all, Sheffield would not feel as close to home as it has done.

Further thanks are owed still, to the friends that have shaped me along the way, and in many cases escaped the hills of South Yorkshire: to Sam - for being my bonus brother across the last decade of our lives, through thick and thin; to Brenna - as my travel buddy, for your gentle and unwavering friendship; to Jen - for never once letting me get too big for my boots, and still somehow making me feel twice as tall; and to Alfie, Dom, and Joe - for somehow carrying me through the shared gauntlet of an undergraduate Physics degree.

To the wider members of the MOSAIC Group: Niels, Joe, Tom, Erin, Greg - you have all kept me sane at one time or another, in ways that I'm sure many of you haven't even noticed. For this, again, I am grateful. And to our Scandinavian contingent, I owe a further gratitude: Monika - for the shared moments of insanity, and the moments of triumph that followed; Yao - for your patience, as I tried to condense my work into something less incoherent to share with you; Tobias - for your ever-sarcastic friendship, and agreeing to permanently ink yourself alongside me; and Veronica - for your grace, your genuine compassion, and your wisdom. I hope that each and every one of you understands the impact that you have had on me along the way.

Finally, of course, a note for my family, without whom I would not be where I am today. To Sam and Phoebe - thank you for never taking me too seriously, and for (quietly) being my biggest cheerleaders. I am phenomenally proud of the people that you are both becoming, and it has been the privilege of a lifetime to watch you grow. And most importantly, to Mum and Dad - I can never fully repay the debt that I owe to you for the life that you have given me. From the books read to me as a child, to the hours wandering museum halls - you fostered in me the inquisitiveness and the love for learning that I needed to make this possible. For all of the unconditional love, support and motivation - I cannot thank you enough.

Contents

List of Figures

List of Tables

Glossary of Acronyms

(C)SRO - (Chemical) Short Range Order
LRO - Long Range Order
MPEA - Multi-Principal Element Alloy
HEA - High Entropy Alloy
CCA - Complex Concentrated Alloy
DFT - Density Functional Theory
SQS - Special Quasirandom Structures
ML - Machine Learning
WC - Warren-Cowley (Parameter)
(HR/S)TEM - (High-Resolution/Scanning) Transmission Electron Microscopy
EDS/EDX - Energy Dispersive (X-ray) Spectroscopy
EXAFS - Extended X-ray Absorption Fine Structure Spectroscopy
NMR - Nuclear Magnetic Resonance
APT - Atom Probe Tomography
(R)MC - (Reverse) Monte Carlo
FCC - Face Centred Cubic
BCC - Body Centred Cubic
MSAD - Mean-Squared Atomic Displacements
HAADF - High Angular Annular Dark Field
CTE - Charge Transfer Effect
PDF - Pair Distribution Function
FWHM - Full Width Half Maximum
TOF - Time of Flight (Diffractometer)
Mantid - Manipulation & Analysis Toolkit for Instrument Data
GSAS(-II) - General Structure Analysis System (-II)
ICSD - Inorganic Crystal Structure Database
SToG - S(Q) to G(r)

(I)FFT - (Inverse) Fast Fourier Transform
ICP-OES - Inductively Coupled Plasma Optical Emission Spectroscopy
CIF - Crystallographic Information File

Abstract

'Short-range order' (SRO) - preferential atomic ordering behaviour deviating from a statistically random distribution of elements within a local region - is acknowledged across the literature as a contributor to the mechanical properties of crystalline materials. Multi-principal element alloys (MPEAs) may possess some form of statistical SRO, evidenced by their unique properties. Analytical complexities, however, have hindered efforts to quantify and describe atomic ordering. While local order has been identified in *binary* alloys, the efficacy of the method is not established for chemically complex systems.

This work seeks to develop a novel analytical method for the investigation of SRO in multi-principal element alloys (MPEAS) using total scattering. Firstly, neutron total scattering data is used to perform pair distribution function analysis on the CrCoNi MPEA. Modelling of the CrCoNi system to cryogenic temperatures demonstrates the local formation of the $L1_2$ structure.

Analysis of the CrFeCoNi MPEA is subsequently performed. This investigation is used to demonstrate the increase in analytical complexity with increased quantities of constituent elements, and provides a logical step towards the analysis of traditional 'high-entropy alloy' (HEA) systems. Through a neutron total scattering investigation at raised temperatures, it is shown that the CrFeCoNi alloy *also* presents with a local $L1_2$ structure.

Finally, a novel framework for the investigation of SRO is presented. Building on the prior methods, this framework has been used to generate an associated software available for use across a range of crystal structures. Test cases are presented from a variety of material domains as a proof of concept.

In summary, this work shows the effectiveness of the total scattering and large-box modelling method in the investigation of atomic SRO in chemically complex materials. It is hoped that the successful development of novel, generalised analytical methods will provide the crystallographic community with the tools to investigate SRO more widely.

Chapter 1

Background

1.1 Short-Range Order

It is commonly accepted in the metallurgical literature that purportedly 'randomly distributed', single-phase alloys are likely to possess some degree of atomic-scale ordering. In an ideal metallic solid solution, ordering transitions are accepted to occur across temperature regimes: at very high temperatures, the entropic term of the Gibbs free energy dominates the enthalpic term, maximising the randomness of atomic distributions; as the temperature of the sample is reduced, enthalpy begins to dominate the system, and preferential ordering is introduced. It is within this enthalpic region that the long-range crystallographic structures typically associated with metallic materials form [1].

Historically, solid solutions in the entropy-dominant region have been assumed to possess an entirely (statistically) random distribution of constituent elements. The transition from entropy-driven to enthalpy-driven atomic ordering behaviour has, by extension, typically been treated as an instantaneous boundary - i.e. as a first order phase transition - whereby atoms order themselves from the disordered state immediately upon cooling beyond the critical temperature. In this model, limited consideration is given to the intermediary stages of ordering - the formation of *locally* ordered regions within an otherwise seemingly 'random' distribution of constituent elements. This intermediate ordering stage is known as 'Short Range Order' (SRO).

SRO - also referred to in the literature as 'chemical short-range order', or CSRO - may be defined as the preferential nearest-neighbour occupancy of atoms to within a few coordination shells, in a manner not easily predicted by basic probabilistic modelling [2], [3]. Where basic models might assume that preferential ordering in a random solid solution would be dictated entirely by the

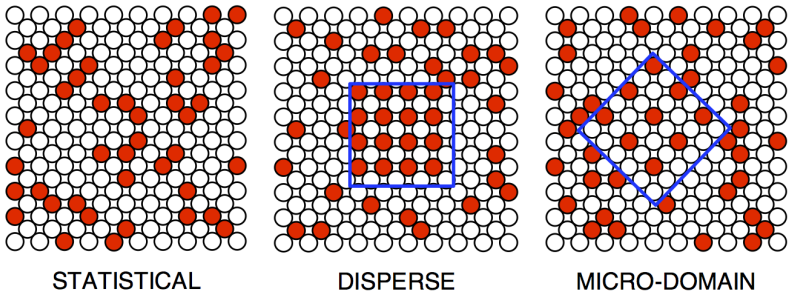

Figure 1.1: The three commonly described forms of SRO: statistical, disperse, and micro-domain models. The following work concerns itself primarily with a statistical description of ordering behaviour. Figure provided by Owen *et al.* [4].

proportion of a given element in that material, SRO-type behaviours are more complex. Though three forms of SRO have historically been described - micro-domain and disperse ordering potentially falling into this category under certain descriptions - the following work will concern itself primarily with statistical SRO descriptions (Figure 1.1). This ordering stands in contrast to more well-researched long-range ordered (LRO) structures - such as the crystallographic periodicity of traditional metallic systems - occurring instead over distances on the scale of interatomic distances.

Given the relative disparity in research on the formation and mechanical behaviours of LRO structures versus the presence of SRO, it is no surprise that the overall impact of SRO on the performance of alloys is less well understood. It has long been suggested that retained SRO can impact physical properties - including yield strength, dislocation motion, and resistance to radiation damage - with limited empirical evidence for this assertion presented simultaneously [5][6].

As a brief aside, it should be clarified that the short-range order discussed in the following work refers specifically to atomic occupation on a crystalline lattice, and is distinct from the positional short-range order more widely discussed in the field of glasses [7]. Additionally, it is worth highlighting the ongoing debate within the wider community on the definition of SRO itself. SRO, as a term, has been used to describe nano-regions of ordered domains - perhaps the nucleation point for many LRO structures - or even local clusters of like atomic species. The question remains, then, as to the size or scale at which a short-range ordered region is deemed to have become a long-range ordered structure, or phase. A statistical description of order concerns the manner in which the nominal stoichiometry of a given material differs from the proportion of atoms in a given coordination shell about a given lattice site. A *disperse* model of order might possess a nanoscale *region* of order with a stoichiometry that does not match the stoichiometry of the remaining lattice; a *micro-domain*,

on the other hand, will possess an ordered region with an equivalent stoichiometry to the wider lattice, differing only by the extent of ordering in that region.

Ultimately, the following work opts to use the local, statistical definitions of SRO presented above to describe homogeneous chemical short-range order.

1.2 Multi-Principal Element Alloys

Multi-Principal Element Alloys (MPEAs) are an emerging class of specialised alloy systems, typically comprising three or more metallic elements in solid solution at near-equiatomic concentrations. Variously also known as High-Entropy Alloys (HEAs) or Complex Concentrated Alloys (CCAs), these systems have gained significant traction across a range of technical applications for their wide compositional space and associated - often unique - mechanical properties [8], [9], [10]. The random distribution of constituent elements is believed to favour the formation of a single-phase solid solution above the formation of potentially deleterious intermetallic phases, through entropy stabilisation, by extension providing enhancement to existing macroscopic behaviours [11].

High Entropy Alloys were first deliberately synthesised and reported upon by Yeh *et al.* [12] and Cantor *et al.* [13] in 2004. Yeh initially established a series of 'governing principles' for these new materials, in an attempt to explain the origins of their impressive mechanical response. For success, each alloy must necessarily possess:

1. High configurational entropy - driven by compositional complexity - leading to the formation of single-phase solid solutions.
2. A severely distorted lattice, primarily caused by the difference in atomic radii of constituent elements.
3. Sluggish diffusion kinetics, caused by the formation of local, low-energy diffusion traps.
4. A poorly defined, so-called 'cocktail effect', providing additional enhancement to mechanical properties.

Though the validity of these principles will be discussed in the following sections, they continue to influence thinking under the MPEA banner. In particular, it can be quickly noted that three of the four 'tenets' concern the local behaviour of constituent elements. The purportedly 'high entropy' of constituent atomic species and lattice distortion effects are governed entirely by atomic distributions; these distributions are believed to give rise in turn to increased normalised activation energies for diffusion phenomena [14], [15]. The requirement for high entropy specifically necessitates the random distribution of constituent elements in solid solution: the enthalpic contributions to the Gibbs free energy may only be overcome if the configurational entropy of the system is high.

The supposed randomness of atomic distribution ultimately creates friction with a more modern understanding of atomic dynamics and the probabilistic modelling briefly touched upon in Section 1.1. The description of randomness in such systems has been acknowledged as an oversimplification for many years, and the likely presence of SRO has, by extension, been an accepted but largely untested phenomenon. Furthermore, the SRO hypothesised in MPEAs has been proposed as a potential origin for many of the remarkable mechanical properties of the alloys [16], though to date many of these suggestions remain empirically unproven.

1.3 Methods for the Elucidation of SRO

The absence of any formal, definitive experimental determination of SRO in MPEAs is not for lack of investigation. Broadly, the existing investigations into atomic ordering behaviours in random solid solutions may be divided into three approaches: predictive and modelling techniques, used to preempt the existence of SRO; inference of SRO via indirect characterisation; and direct experimental characterisation.

1.3.1 Predictive and Modelling Techniques

As a generalisation, the majority of existing studies on SRO-type behaviours in MPEAs are predictive in nature. Nonetheless, such studies represent an excellent starting position for the investigation of SRO, not least because they can provide interesting insights into macroscopic material responses. Models can range in complexity, from simple empirical models to more complex, first-principles calculations. Simplified empirical models, for instance - such as those used to calculate atomic size mismatch - have been used in a number of studies to establish local lattice effects and their impact on mechanical properties [17].

The most common form of predictive modelling in the investigation of local chemical ordering is Density Functional Theory (DFT) [18]. *Ab initio* ('from first principles') calculations are performed to predict material behaviours via the simulation of electronic structure. Structural properties may be reconstructed through the iterative application of summed potentials and exchange-correlation functionals to a given model. As a method for the analysis of atomic behaviours, DFT is often well regarded, and many existing studies have shown strong agreement with experimentally observed mechanical properties. It remains, however, predictive in nature - it cannot provide more than an approximation of atomic structure, even at its most complex. It is limited by the size and complexity of its models - as the computational requirements for larger, more chemically complex structures rapidly escalate - making it a poor predictor for MPEAs in particular. Efforts have been made to adapt the method for this exact purpose, with the introduction of Special Quasirandom Structures (SQS) [19] and machine learning (ML) potentials trained on larger models [20], [21]. These ML

potentials are computational models that use ML algorithms - trained on high-accuracy quantum mechanical data - to predict the forces and energy between atoms, thereby allowing reconstruction of atomic ordering.

The method is still severely limited by standard computational restrictions, largely due to the increased size of model required for simulation; traditional DFT methods typically use boxes containing a few hundred atoms, while ML methods employ boxes containing tens of thousands of atoms.

1.3.2 Direct & Indirect Characterisation of SRO

Indirect Characterisation

The other two forms of characterisation - both direct and indirect - are both experimentally derived, but differ significantly in their impact and reliability. The inference of SRO is perhaps as widespread as the use of predictive modelling methods, and has a long-standing history in the metallurgical literature. The correlation between material properties and atomic structure is well established, and it therefore follows that local or short-range atomic structure has a non-negligible impact on mechanical response. [22]

Inferential studies, however, can never be used to conclusively describe local atomic ordering. A complete description of SRO-type behaviours would ideally include a qualitative description of the atomic motifs most commonly encountered in a given material, parallel to any numerically quantitative description. Many current indirect characterisation techniques reduce the description of SRO to a single, one-dimensional parameter or value, immediately averaging the overall result and removing any spatial component to the distribution of atomic species. To resolve this concern, a number of characterisation techniques have been developed to directly probe local chemical environments.

Transmission Electron Microscopy (TEM)

As mentioned briefly above, many existing TEM studies make use of inferential analysis to establish the presence of SRO in metallic samples [23]. The technique cannot, however, physically demonstrate ordering at the level of individual atoms. With the increasing resolution of modern electron microscopes, it is not unreasonable to suggest that the technique will increasingly feature in local structural investigations - and indeed has already been used to demonstrate order via atomic column mapping, outlined below - but the likelihood of using TEM analysis in isolation without supporting evidence is slim.

The same may be said of EDS line-scanning using TEM instruments. EDS - or Energy Dispersive X-ray Spectroscopy - is a form of characterisation used to analyse the chemical composition of thin samples. As the TEM beam is passed over the sample, the electrons interact with the internal structure of the material, producing characteristic X-rays. The wavelengths of these X-rays are unique to a given chemical species, this technique may be used to identify the presence of particular atoms, or their variation over a region [24]. In the case of line-scanning, the beam is passed over the material in a straight line, effectively providing information on the *average* variation in chemical composition over a region. In this fashion, it has been used at higher resolutions to suggest the local atomic bonding preferences of metallic materials. The technique is, however, ultimately an averaging of chemical concentration for a given atomic *column*, and corrections for X-ray intensities are likely to introduce further complexity. With information provided in only a single dimension -

i.e. variation along the scanning direction - it is difficult to assess local atomic configurations with any degree of certainty.

As a final note on TEM analysis, a recent study by Walsh *et al.* sought to reappraise the efficacy of investigating SRO through analysis of diffuse streaking in TEM images [25]. In doing so, the group found that such diffuse 'wings' cannot be exclusively linked to atomic ordering behaviours. Instead, Walsh suggests that 'symmetry-breaking effects' - a broad ranging group of potential phenomena - may also explain their presence, placing many existing studies under increased scrutiny. Further to this, investigations by Coury *et al.* expand upon this idea considerably, attributing the presence of diffuse scattering to internal reflections: first-order Laue zones lying just above or below the extent of the Ewald sphere of the beam. Samples that are not sufficiently prepared - i.e. those that were too thin, or containing atoms of approximately equal scattering lengths - would therefore produce a greater degree of 'diffuse' scattering, thereby calling existing 'evidence' for SRO into question.

Extended X-ray Absorption Fine Structure (EXAFS) Spectroscopy

Extended X-ray Absorption Fine-Structure Spectrocopy - frequently abbreviated to EXAFS - is an increasingly common form of analysis used to identify or corroborate the presence of SRO in materials. The technique is particularly useful for the analysis of ordering over very short-distance, and is typically limited to information within the first nearest-neighbour shell. EXAFS is used to analyse the so called 'fine structure' just above the X-ray absorption edge of the material ; these edges are a consequence of incident photons matching the binding energy specific to a given atom type. By extension, it is therefore possible to assess the local region around atoms of a specific chemical species [26].

While this form of analysis may represent a powerful tool for the study of local structure in simple materials, and has been rapidly adopted by the community, its use in the analysis of complex structures is not well supported. Chemically complex systems, such as MPEAs or other materials with many constituent elements, require equivalently complex analysis [27]. In many cases, the overlap of X-ray absorption edges between chemical species has a deleterious effect on the quality of the data produced by the technique [28]. It is also worth noting that quantitative analysis - specifically obtaining highly accurate values for parameters like the coordination number and the Debye-Waller factor - is inherently difficult. For this reason, it has not been used to great effect in the study of local order in MPEAs.

Nuclear Magnetic Resonance (NMR)

Nuclear Magnetic Resonance (NMR) spectroscopy is a further method sometimes used in the analysis of crystalline materials. A number of studies, however, have used the technique to investigate local structure and ordering behaviours [29]. Atoms held in a constant magnetic field align the

magnetic spins of their nuclei; a second, weaker oscillating magnetic field is then applied to the system, disturbing this alignment and causing the emission of characteristic radiation according to the species of the nuclei. Such characteristic radiation possesses a shift in energy, brought about by shielding - the interaction of the electron field with the nuclear field - that is characteristic of the local environment. This can then be subsequently used to generate chemical spectra for a given material, ultimately providing insight on composition and structure.

Given the requirement for atoms with non-zero spin quantum numbers to perform this type of characterisation, many MPEAs are not easily analysed in this manner. MPEAs do not often contain spin-active elements, and those with zero spin do not possess the pre-requisite magnetic dipole moment for perturbation. NMR spectroscopy may, however, still provide key information on the prevalence of specific bonding pairs: each bonding type possesses an energy range over which an NMR peak may be observed [30]. Though a useful indicator of potential local ordering preferences, the technique is limited to a distance of only a few coordination shells from a given atom of interest, reducing its efficacy in determining statistical SRO-type behaviour. [31]

Atom Probe Tomography (APT)

Atom Probe Tomography (APT) is a local characterisation technique used to assess atomic structures and chemical variations over small, three-dimensional volumes (less than 50,000nm^3). Given that this is close to atomic-scale resolution, it stands to reason that the technique can be used effectively in the analysis of SRO. Specimens are shaped into atomically-thin needles (tip radii typically formed in the range of 50-100nm), and placed under a strong electric field at cryogenic temperature. A high voltage is then passed through the tip, ionising the surface atoms of the material. The atoms themselves then 'field evaporate', overcoming their binding energy and accelerating away from the tip towards detectors. These detectors can then identify the original location and species of the atom, producing a three-dimensional reconstruction of the tip at the atomic scale from many two-dimensional images of atomic 'layers' [32].

Though an excellent tool for the discernment of chemical segregation in three-dimensional space - potentially providing a wealth of local structural information - the technique is, by definition, destructive. It is therefore a moderately costly technique, even for the small samples associated with the analysis. Equally, it is not straightforward to assess non-chemical local structural effects, such as offsite displacements; many studies therefore combine its use with TEM techniques for broader crystallographic analysis. As a final note, there is an inherent difference between the resolution produced in the z 'depth' direction versus that of the x or y; depth resolution is achieved through precise time-of-flight measurement, while the lateral resolution is reduced by trajectory aberrations, predominantly caused by tip geometry. [33]

1.4 Total Scattering & Pair Distribution Function Analysis

The development of Total Scattering - both using neutrons and X-rays as incident radiation sources - presents a considerable opportunity to address the concerns of existing characterisation techniques. Though a long-standing form of direct structural characterisation in the study of amorphous glasses and non-crystalline solids, its application to metallic systems is a comparatively recent development [34].

The basis of total-scattering diffraction is the combination of traditional Bragg peak analysis with a simultaneous evaluation of diffuse scattering data to establish local structural information. When performing a traditional diffraction analysis on an ideal, ordered crystal lattice, sharp diffraction maxima are brought about by constructive interference according to Bragg's Law. Diffuse scattering, however, has been suggested to be caused by local deviations in the lattice. Both static displacement and chemical variation - i.e. effects that break the perfect periodicity of the lattice - can cause the 'imperfect' scattering of incident radiation over short distances. In reciprocal space, long-range real-space features demonstrate narrow diffraction peaks; such short-range real-space features, then, appear as broad, diffuse signals such as discs, or streaking.

Diffuse scattering - for all of the complexities involved in its analysis - may therefore be indicative of SRO-type behaviour; taken in tandem with traditional crystallographic information, it is therefore possible to reconstruct the likeliest atomic structure for a given material to a distance of many coordination shells. The following work will primarily focus analysis on the use of neutron total scattering. For neutrons, the basic scattering function [35] is given by:

$$S(\vec{Q}) = \frac{1}{N} \sum_{i,j} \langle\ b_i b_j \exp i\vec{Q}.(\vec{r}_i - \vec{r}_j) \rangle \tag{1.1}$$

where $\vec{Q}$ is the scattering vector, or momentum transfer, of incident neutrons; N is the number of atoms in the system (or more generally, the number of 'scattering objects'); $\vec{r}$ the instantaneous position of atoms; b is the atomic scattering length; and i and j are atomic labels. To be entirely clear, b_i is therefore the atomic scattering length of an atom of species 'i'. Q, in this instance, is the associated magnitude of the scattering vector; for simplicity, this may be expressed in the form:

$$Q = |\vec{Q}| = \frac{2\pi}{d} \tag{1.2}$$

where d is the interplanar spacing of a crystallographic sample. For a crystal containing translational periodicity, and with the substitution of vectors, this expression ultimately condenses to a form in which the sharp intensity maxima correspond to the Bragg condition:

$$n\lambda = 2d\sin\theta \tag{1.3}$$

where λ is the wavelength of incident radiation; d is the interplanar spacing of the lattice planes; and θ is the angle of scattering. In this case, the perfect periodicity of lattice planes produces sharp, well-defined maxima from the constructive interference caused by atoms located on ideal lattice sites with discrete crystallographic coordinates. However, Equation 1.1 may also be adapted for non-periodic (amorphous) materials in a generalised form to account for the diffuse scattering caused by deviations from the average structure. Assuming that the sample is a crystallographic powder, the spherically averaged form of the scattering function may ultimately be written as follows:

$$S(Q) = \frac{1}{N}\sum_{i,j} b_i b_j \frac{sin(Q|r_i - r_j|)}{Q|r_i - r_j|} \tag{1.4}$$

Self-scattering arises from the interaction of individual atoms with incident neutrons without correlation to their neighbours or other atoms in the system. The self-scattering term for the scattering function may therefore be separated, in the form:

$$S(Q) = \frac{1}{N}\sum_{i} \bar{b_i^2} + \frac{1}{N}\sum_{i,j} \bar{b_i}\bar{b_j} \frac{\sin(Q|r_i - r_j|)}{|r_i - r_j|} \tag{1.5}$$

Equation 1.5 may then be written in the simplified form:

$$S(Q) = F(Q) + \sum_{i} \left(c_i {b_i}^2\right) \tag{1.6}$$

where Q is the magnitude of the scattering vector; c_i is the concentration of atom ; and $F(Q)$ is described by the expression:

$$F(Q) = \rho_0 \int_0^\infty 4\pi r^2 G(r) \frac{\sin(Qr)}{Qr} dr \tag{1.7}$$

such that r is the magnitude of the difference in atomic position, $(\vec{r}_i - \vec{r}_j)$; and ρ_0 is the average density of the sample structure. Here, the $F(Q)$ describes the scattering from the sample, excluding self-scattering behaviour. Mathematically, it represents a spherically averaged Fourier transform corresponding to the structure of the sample from which incident radiation is scattered.

The $G(r)$ term in Equation 1.7 is known as the Pair Distribution Function (PDF). The PDF may be interpreted as a weighted histogram of interatomic distances for atoms in the material

of interest, provided in real-space terms. Mathematically speaking, the $G(r)$ is in fact an *inverse* Fourier transform of Equation 1.6, representing a conversion from the more traditionally understood Q-space diffraction pattern to the real-space distribution of constituent atoms, as expressed by:

$$G(r) = \frac{1}{(2\pi)^3 \rho_0} \int_0^\infty 4\pi Q^2 \; F(Q) \frac{\sin(Qr)}{Qr} dQ \tag{1.8}$$

This represents a Fourier transform integration across all of space from the origin to infinity. In practical terms, this is not achievable; a diffractometer cannot collate data over infinite space. As such, the following modification is made to Equation 1.8 to impose limit constraints on the Fourier transform:

$$G(r) = \frac{1}{(2\pi)^3 \rho_0} \int_{Q_{\text{max}}}^{Q_{\text{min}}} 4\pi Q^2 \; F(Q) \frac{\sin(Qr)}{Qr} dQ \tag{1.9}$$

where Q_{max} and Q_{min} are imposed boundary conditions corresponding to the maximum and minimum values of the magnitude of the scattering vector. PDFs, as the name suggests, are composed of a series of partial functions corresponding to the distributions of atomic pairs and weighted by the associated neutron scattering lengths of the pairs. In a binary system, for instance, there would be three total partial PDFs corresponding to the like and dislike atomic pairings: A-A, B-B, and A-B. The $G(r)$ may therefore also be written in terms of these constituent partial functions, as follows:

$$G(r) = \sum_{i,j} c_i c_j b_i b_j (g_{ij}(r) - 1) \tag{1.10}$$

where c is the concentration of an atomic species; and $g_{ij}(r)$ is the partial function associated with the pair ij as given by:

$$g_{ij}(r) = \frac{1}{4\pi r^2 \rho_i} \frac{dn_{ij}(r)}{dr} \tag{1.11}$$

where $n_{ij}(r)$ is the total number of atoms over a distance of r to $r + dr$; and ρ_i is the number density of the chemical species, i.

Peaks in the total PDF correspond to the distances at which particular atoms are found from a given origin. Each peak therefore also represents a given coordination shell for the material of interest: the first peak in the PDF corresponds to the shortest correlated distance from an atom at the origin, and therefore represents the first coordination shell, and so on (Figure 1.2). It is not difficult, then,

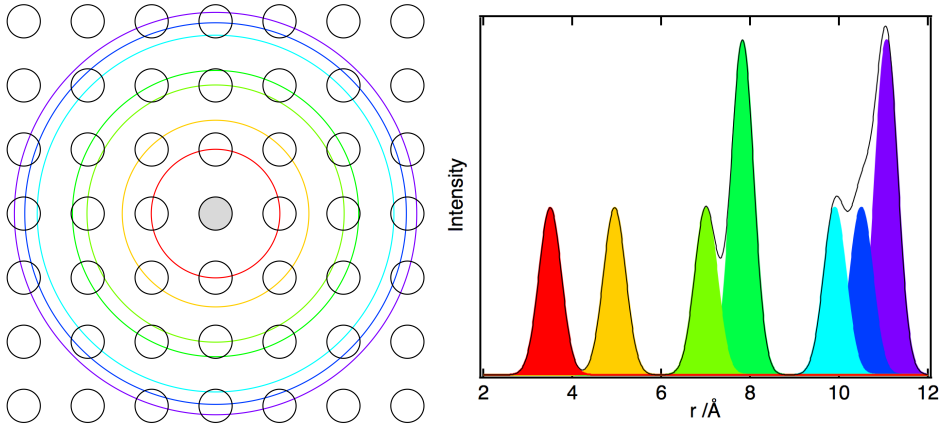

Figure 1.2: A diagram demonstrating the coordination shells of a lattice in two-dimensions (Left) and the associated peaks (coloured) of a simple PDF function (Right). Figure provided by Owen *et al.* [36].

to see the manner in which one might construct an overall picture of the local ordering from such a function. Both the $F(Q)$ and $G(r)$ functions represent the core of total scattering theory for this reason, and the Fourier transform relationship between these functions is integral to large- and small-box modelling. By collecting Bragg data according to traditional diffraction analysis methods, it is possible to use expected crystallographic information in combination with the calculated $F(Q)$ and $G(r)$ to produce a full descriptive model of both the long- and short-range properties of the sample in question in three dimensions.

As a note, on the $G(r)$: British and American conventions on the form of the PDF differ significantly. The following work specifically uses the British convention, which states that the $G(r)$ tends to 0 at high-r, and to $-\langle b\rangle^2$ at low-r; the British $D(r)$, then, is an r-scaled form of the $G(r)$, tending to 0 at high$r$ and $-4\pi\rho r\langle b\rangle^2$ at low-r. In the American convention, the $G(r)$ is actually equivalent to the British $D(r)$, which may cause confusion if left unstated.

1.5 Quantifying SRO

1.5.1 Warren-Cowley Parameters

All of the characterisation techniques described above can provide evidence for SRO-type behaviours, but the quantification of these phenomena requires further treatment. There are a number of existing techniques for the description of SRO in crystalline materials, but the most ubiquitous and commonly understood method is the use of Warren-Cowley parameters. As a longstanding form of quantification, Warren-Cowley parameters were initially formulated as an analytical method for binary structures. For a given coordination shell, a single-dimensional parameter (α) is calculated to describe the relative abundance of atomic pairs in that shell [37] using the following expression:

$$\alpha^{AB} = 1 - \frac{P^{AB}}{c_B} \tag{1.12}$$

where P^{AB} is the probability of finding an atom of species B in a given coordination shell a distance away from an origin atom of species A; c_B is the atomic fraction of B atoms in the system; and α^{AB} is then the Warren-Cowley parameter for atomic pair $A-B$ in the selected coordination shell. A preference for like-species bonding produces an α value of 1 (as P^{AB} tends towards zero). An entirely random distribution of constituent elements produces an α value of 0, as P^{AB} converges on the atomic fraction. Negative values of α represent a preference for dislike bonding pairs, as the probability of finding an atom B in a given coordination shell becomes greater than its concentration in the bulk.

Long-range ordered (LRO) binary structures will demonstrate a characteristic oscillation of values through coordination shells; the $L1_2$ structure, for instance, demonstrates an alternating series of Warren-Cowley parameters, with successive positive and negative values in each coordination shell (Figure 1.3). SRO-type behaviours, however, are likely to demonstrate strong ordering preferences in the first few coordination shells, with decreasing intensity at greater distances.

Expanding upon this further for systems of greater chemical complexity, such as MPEAs, the 'Pairwise Multicomponent' Warren-Cowley parameters were formulated [37], such that:

$$\alpha_m^{AB} = \frac{p_m^{AB} - c_B}{\delta^{AB} - c_B} \tag{1.13}$$

wherein p_m^{AB} is the probability of finding an atom of type B in shell m; and δ^{AB} is an integer parameter, such that δ=0 when A and B are dislike atomic species and δ=1 when they are like atomic species.

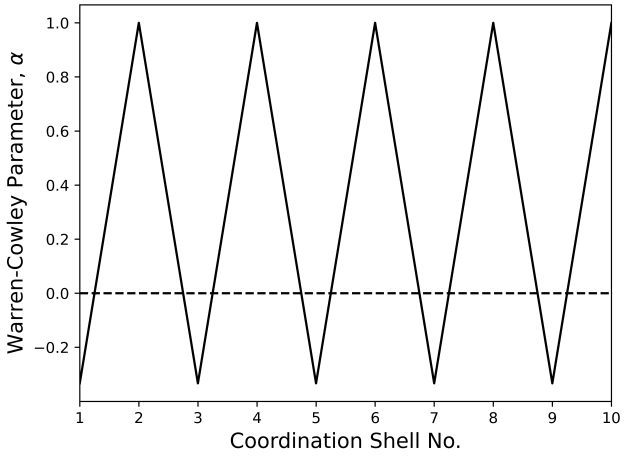

Figure 1.3: The oscillating Warren-Cowley parameters of a long-range ordered $L1_2$ structure to a distance of 10 coordination shells.

This expression condenses to the original formulation of the Warren-Cowley parameter for binary structures.

Such quantification of pair bonding is a necessary step in the analysis of local order, but the use of Warren-Cowley-type analysis is not without its drawbacks. Importantly, such analysis reduces the description of SRO in the system into a parameter with only a single dimension. Some of the nuance in the analysis is lost, particularly with regards to local atomic ordering; one cannot entirely deduce the enhancement of particular atomic motifs, nor their distribution throughout a given material from Warren-Cowley parameters alone.

1.5.2 Clapp Configurations

Though Warren-Cowley parameters provide a good initial overview of the likely ordering behaviours in crystalline materials - particularly for simple chemical systems - they provide an overall reductive description. Collapsing three-dimensional structural information into a single-dimensional value removes the nuance of the analysis, and fails to provide information on the exact orientation or distribution of atoms in real-space. For this reason, novel methods for describing atomic configurations are becoming increasingly prevalent.

An alternative method for the description of ordering behaviours in a crystal lattice are 'Clapp configurations'. First outlined by Phillip Clapp in 1971 [38], Clapp configurations are numeric descriptors of atomic configurations or motifs corresponding to occupation of nearest-neighbour

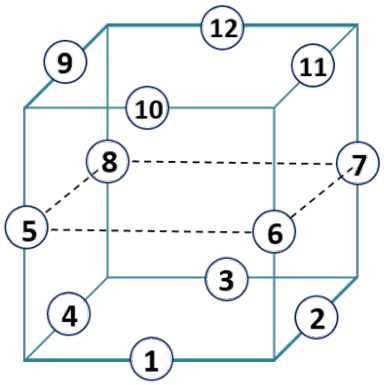

k	Occupied Positions					
-1						
1						
2	6					
3	6	7				
4	5	7				
5	6	12				
6	6	11				
7	5	6	7			
8	5	6	12			

Figure 1.4: The enumerated atomic positions of an FCC unit cell (left) and associated, short selection of Clapp labels for this system.

positions of a given lattice site. For any atom in a binary system of 'A' and 'B' type atoms with n nearest neighbours, there exist 2^n possible atomic configurations of the unit cell. For an atom in an FCC unit cell with 12 nearest neighbours, there is therefore an absolute maximum of 4096 possible configurations of atoms that are theoretically capable of developing in a binary lattice. Condensing this number via symmetry and orientational considerations - as many atomic configurations are functionally equivalent when the unit cell is rotated - Clapp enumerated 144 unique arrangements of the FCC unit cell according to a geometric convention. An equivalent treatment for the BCC unit cell identified 256 possible configurations of nearest neighbour atoms, and a much reduced 22 unique configurations associated by symmetry.

This generalised description of unit cell arrangements, based entirely on the enumeration of atomic positions, is a useful tool in the discernment and description of SRO behaviours in binary systems. The labelling system devised by Clapp can be used to denote both the number and type of atoms in a unit cell, with incorporated conventions for like and dislike bonding. Thus, for any such system in which the positions of atoms are 'known' or reconstructed, it is possible to determine the frequency with which certain local structural motifs appear in the system in three-dimensions. Extending this concept, it is also theoretically possible to determine the configurational *pathways* of randomly distributed binary materials: configurations of atoms with similar common motifs - i.e. configurations that are equivalent but for the presence or position of a single atom - are more likely to be enhanced simultaneously than those that differ structurally. It is then possible to extrapolate from the enhancement of associated configurations to a likeliest 'pathway' indicative of the manner in which a randomly distributed system might order itself [35]. More simply, too, the most enhanced structural motifs in the system can provide insight into the factors that drive the formation of particular atomic configurations.

The application of Clapp configurations has already proven useful in the description of SRO for binary materials. Work by Owen *et al.* [39], for instance, demonstrated the atomic ordering behaviours of the oft-cited Cu_3Au binary alloy using a combination of PDF analysis and large-box modelling, applying Clapp configurations as a form of structural analysis. The study confirmed that the system undergoes an ordering transition at approximately 400°C, as anticipated by the literature. Importantly, however, a gradual increase in statistical ordering was identified across a region of 400-500°C, demonstrating the emergence of long-range order (LRO) from SRO-type behaviours. Enhancements to the C-1, C7, C16 ad C34 configurations identify the formation of the $L1_2$ structure; the C16 configuration itself represents the $L1_2$ unit cell, while its companion configurations represent a deviation of one or two dislike atoms from the C16 structure. In this fashion, it is possible to map the increase in enhancement to the C16 configuration - and simultaneous enhancement to its 'family' of associated configurations - with heating or cooling to demonstrate the creation or degradation of the $L1_2$ structure (Figure 1.5) [1].

Extending this concept to more compositionally complex multicomponent systems is non-trivial. Due to the limitation of the techniques available at the time, Clapp was more concerned with studies concerning binary systems, with non consideration given to those of a higher order. The extension of this concept to systems of greater complexity is discussed in Chapters 2 and 3.

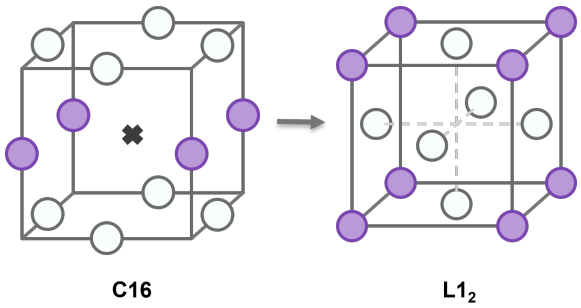

Figure 1.5: A diagram demonstrating the link between the $L1_2$ structure and the C16 configuration, as outlined by Clapp.

[1] This is further discussed, at length, in Chapter 3.

1.6 SRO in MPEAs

The techniques described above have, therefore, been employed in the identification of local ordering behaviours to varying degrees of success. Perhaps the most widely studied of the so-called 'High Entropy Alloys' is the CrMnFeCoNi quinary system, a system so ubiquitous that is has been adopted by the community as the 'exemplar HEA'. As a purportedly randomly distributed, single-phase equiatomic solid solution with an FCC crystal structure, the origins of its unique property enhancements - including heightened strength, ductility, and fracture toughness - are not well understood. Indeed, CrMnFeCoNi demonstrates cryogenic strength-ductility properties that outperform many existing structural alloys [40], and equally impressive radiation resistance properties [41], yet the source of these properties remains unexplained. As one of the first MPEAs to be fabricated and mechanically tested, this is perhaps surprising. Many investigations have pointed towards the local order of the alloy to begin providing an explanation for these behaviours, whether attributable to the randomness of distribution in constituent elements or to an as-yet unseen, untested form of local atomic order.

Modelling for this system is extensive. A 2022 study by Mizuno *et al.* made use of a hybrid approach for the simulation of local order in the system, combining first-principles calculations with Monte-Carlo relaxation to produce a physically representative model [42]. FCC supercells containing 125 randomly distributed atoms of the constituent atomic species were generated and relaxed using the combined MC-DFT approach, with Warren-Cowley parameters subsequently calculated to demonstrate potential ordering. The study noted a relative enhancement in the number of Cr-Fe, Cr-Co, and Cr-Ni bonds, potentially indicating an average preference for dislike bonding in the Cr atoms of the system. This Cr segregation is then ascribed to the formation of an $L1_2$ structure in the system, with Cr atoms forming the corners of the FCC unit cell. The authors of the investigation use these findings to evidence the potential increase in elastic modulus of the alloy, though they present no experimentally determined values to support this assertion.

Given the impressive capabilities of the CrMnFeCoNi MPEA, and the large compositional space afforded by its constituent elements, an ecosystem of alloys derived from the original composition has since gained a considerable traction in the engineering community. The FCC VCoNi alloy, for instance, is a refractory ternary alloy of interest building upon the framework of the CrMnFeCoNi alloy, with a specific focus on the CoNi binary. As with the CrMnFeCoNi alloy, VCoNi has demonstrated considerable strength properties at room temperature, along with a promising resistance to hydrogen-embrittlement, both of which are of potential interest to the nuclear energy sector [43]. A study by Sohn *et al.* in 2019 [44], operating under the assumption that the material must possess some form of SRO, investigated the role of severe lattice distortion in the enhancement of mechanical properties in the VCoNi alloy. Using *ab initio* DFT calculations, the study identified

large 'mean-squared atomic displacements' (MSAD) in the system, indicating large local lattice distortions at nearly double the size of MSAD values calculated for CrMnFeCoNi. A concurrent increase in the strength and yield stress of the material is used to suggest a link between alloy grain size, lattice distortion, and improved mechanical properties, though limited empirical evidence is again provided for these results.

Similarly, a number of investigations have opted for a substitutional approach, replacing the constituent elements of the CrMnFeCoNi with alternative metallic species. The FCC FeCoNiCuPd system, for instance, has been suggested to demonstrate SRO in a Monte Carlo-DFT study by Chen *et al.*. [45] Using TiFeCoNiCu as a point of comparison, the authors note an increase in SRO when each FeCoNiCuPd supercell is energetically relaxed. The same behaviour is not identified in the TiFeCoNiCu simulation, attributed by the authors to a (somewhat nebulously defined) 'chemical affinity' parameter. The finding in this instance is used to explain the high yield strength of CrFeCoNiPd samples, though as with prior studies there is only limited physical support provided in the study for this assertion.

There of course exists a wide array of material not based on the CrMnFeCoNi formula. TiZrNbTa, for instance, is a single-phase BCC MPEA noted for its interesting behaviour in response to oxygen-rich environments. A study by Wang *et al.* made use of High-Resolution TEM (HRTEM) and High Angular Annular Dark Field (HAADF) imaging to assess the extent to which the TiZrNbTa lattice is distorted [46]. The authors hypothesise that the severity of local lattice distortion effectively controls oxygen diffusion: severely distorted regions of the lattice (i.e. those rich in Ti-Zr pairs) hinder the diffusion of oxygen through the material, increasing the oxidation levels in the local environment. The study fails, however, to provide evidence for SRO outside of the presence of diffuse 'wings' in the TEM images, potentially indicating a requirement for further analysis.

Akin to the derivatives of CrMnFeCoNi, the TiZrNb ternary acts as a basis for a number of other alloys suspected of possessing unique SRO and properties, including the TiZrNbHf and TiZrNbHfTa MPEAs. *Ab initio* DFT and Warren-Cowley parameter calculations by Zhang *et al.* [47] demonstrate an increased preference in TiZrNbHf supercells for Nb-Hf and Ti-Zr atomic pairs, in agreement with prior experimentally derived findings. Further DFT calculations by Tong *et al.* on the TiZrNbHfTa system demonstrate a low atomic size mismatch, seemingly against expectations derived from calculated lattice distortions. The lattice distortions in both systems are substantial, potentially illustrating the origins of their high phase stability and impressive plasticity [48]. The authors attribute this overall discrepancy to the charge transfer effect (CTE), which reduces the difference in atomic radii between constituent elements.

The above list of complex metallic systems is, naturally, not exhaustive, and the compositional space afforded by MPEAs is near countably-infinite. The number of investigations into SRO,

however, is comparatively low. Indeed, discrepancies continue to exist between the number of studies into MPEAs of differing crystal structures, with the number of FCC alloys assessed for their local structure far outnumbered by their BCC counterparts. The existing concerns around the efficacy of analysis methods also presents an ever-widening concern for the community: there are few methods that can be used incisively to determine the form and quantity of SRO in chemically complex materials. It is for this reason that the continued invention and development of direct characterisation techniques remains a priority for the MPEA research sector.

1.6.1 Existing Pair Distribution Function Analyses in MPEAs

Given that the total scattering diffraction technique allows for a near-complete description of local ordering behaviours, a number of studies have employed PDF analysis in the study of atomic structure in MPEAs. Indeed, total scattering may represent a significant bridge between existing modelling efforts - which commonly do not provide empirical data for comparison - and mechanical studies, through the simulated reconstruction of crystal structure from experimental data.

The ubiquity of the CrMnFeCoNi alloy is further demonstrated by the number of PDF studies that are already beginning to appear around the material and its derivatives. One such study by Owen *et al.* in 2017 sought to identify the extent to which chemical complexity impacts the local lattice distortion of the CrMnFeCoNi MPEA [39], using PDF data collected at the ISIS Neutron and Muon Source. The authors draw a link between the distribution of distances between atomic pairs - assessed using partial pair distribution function peak widths - and the atomic size misfit of the material to determine lattice strain. Chemical complexity in the alloy did not appear to impact the severity of local lattice strain when compared to alloys with fewer atomic species, with both CrNi and CrCoNi demonstrating near-equivalent lattice strain. CrMnFeCoNi, however, was noted to possess a lower melting temperature than its less chemically complex counterparts; the authors note that this would cause a larger degree of peak broadening in the PDF, due to the contributions of thermal oscillations to atomic positions. To clarify this result, therefore, a further study was conducted by Owen *et al.* in 2024 to present a method for the isolation of static and thermal contributions to peak widths [49]. It was determined that - even at low temperature - the thermal offsite displacements of CrMnFeCoNi and CrCoNi samples outweigh the static offsite displacements of the sample. The evidence presented, then, for the severe distortion of the crystal lattice in MPEAs, was deemed insufficient.

This result was further supported and elaborated by a study in 2021 by Thirathipviwat *et al.* [50], who sought to assess lattice strain against a number of mechanical properties in the CrMnFeCoNi alloy. PDF analysis was performed by the group using X-ray data diffraction data (High Resolution Powder Diffraction Beamline P02.1, PETRA III, DESY, Germany), and identified no correlation between chemical complexity and the severity of lattice distortion. FeNi, FeCoNi, CrFe-

CoNi, and CrMnFeCoNi samples demonstrated approximately equivalent atomic size misfit values (0.65-1.18%), likely due to their approximately equivalent atomic radii, and by extension the mechanical performance of each (yield strength and microhardness) was found to vary over a very narrow range.

Equivalently, in the BCC MPEAs, a number of studies have made use of total scattering techniques to determine local structure. A study by Nygård *(*et al.) [51] made use of a Reverse Monte Carlo (RMC) method to assess the severity of lattice distortion in simulated supercells of BCC MPEAs. For TiVNb, TiVZrNb, and TiVZrNbHf, it was determined that lattice distortion scaled somewhat with additional elemental additions, with the Full Width Half Maxima (FWHM) values of PDF peaks increasing with increased chemical complexity. The study does not, however, account for thermal broadening in the PDF peaks, and further work is required in this regard to confirm the findings of the investigation. Analysis of the supercells generated using the RMC methodology demonstrates the potential ordering of atomic species; the calculation of WC parameters for the first coordination shell appears to show the increased likelihood of like Nb pairing in TiVZrNb, and like Hf pairing in TiVZrNbHf, though the validity of the result requires further assessment. A separate study by Guo *et al.* in 2013 appears to suggest similar lattice distortion effects [52]. The investigation identified discrepancies between a simulated PDF calculated for the ZrNbHf ternary and equivalent neutron diffraction data, which the authors use as evidence for severe local distortions in the BCC crystal lattice.

As is perhaps evident from the above review of existing studies, many investigations into local order using PDFs have, to date, focused their attention on the distortion of the crystal lattice. Previously described studies by Owen *et al.* [39], however, have demonstrated the potential utility of applying PDF analysis in the analysis of SRO in binary metallic materials. Expanding upon this work - extending the analysis from binary alloys to systems of greater chemical complexity - is one avenue of investigation that could yet provide a wealth of local structural information.

1.7 Outline of work

The following work will therefore seek to assess the suitability of applying the total-scattering method to the analysis of SRO in systems of greater chemical complexity. This will require a feasibility study of the characterisation technique itself - which, as described above, has previously only been used in the investigation of chemical ordering in binary materials - as well as the development of novel and existing structural quantification techniques. Chapter 2 will outline some of the standard total scattering methodology used throughout this thesis.

Chapter 3 will seek to establish the feasibility of applying the total scattering method to a system of greater chemical complexity - namely, the ternary CrCoNi MPEA. The work undertaken therein may be sub-divided into three primary investigations: the first explores the capabilities of the method in reproducing the atomic-scale ordering of the alloy in question; the second will demonstrate the applicability of Clapp-style configurational analysis for ternary systems; and the third will establish the extent to which the method is capable of distinguishing between unique configurational results. Chapter 4 will then expand upon the work outlined in Chapter 3 directly, applying the total scattering method and associated structural quantification techniques to the quaternary CrFeCoNi MPEA, representing an incremental increase in chemical complexity.

Chapter 5 will present a novel framework for the analysis of SRO in crystalline materials. This will involve both the adaptation and generalisation of the existing Clapp method for systems of reduced symmetry, as well as the production of a bespoke software package for the application of this analysis technique. A series of test cases spanning a range of common crystalline materials (not limited to metallic systems) is presented as a proof of concept.

Finally, the conclusions for the above studies and a brief overview of potential future avenues of investigation will be presented as part of a summary in Chapter 6.

Chapter 2

Experimental & Analytical Methods

The following chapter represents an overview of the techniques employed in the analysis of SRO in MPEAs. This work proposes the use of total scattering diffraction - in this instance, using neutrons as an incident radiation source - in combination with Clapp configurational analyses to identify local atomic ordering in chemically complex materials. Where necessary or relevant, further methodological detail is provided in each experimental chapter to expand upon the descriptions provided herein.

2.1 Neutron Diffraction & Powder Metallurgy

2.1.1 Polaris, ISIS Neutron & Muon Source

The following work is primarily concerned with the analysis of neutron diffraction data, as collected using the Polaris diffractometer at the ISIS Neutron & Muon Source (Oxfordshire, UK) [53]. Polaris is a high-intensity, medium-resolution Time-of-Flight (TOF) powder diffractometer. Incident neutrons are produced using a spallation source: high-energy protons are pulsed and guided to bombard a heavy metal target within the ISIS facility, producing secondary pulses of high-energy, high-flux neutrons for use across a range of instruments.

More specifically, Polaris receives a beam of 'polychromatic' (or 'white') neutrons, moderated through water. Spallation sources - unlike nuclear reactor sources, which typically make use of monochromated neutron beams - therefore produce a range of neutron energies across the beam

pulse, with the moderator used to favourably 'shape' the energy spectra. Each of the detectors measures the time between the collision of the neutron pulse with the target and subsequent neutron detection; it is then possible to relate this time of flight and distance travelled to calculate neutron velocities and momenta. The De Broglie wavelength, λ_{DB} of a given object is given by:

$$\lambda_{\mathrm{DB}} = \frac{h}{mv} \tag{2.1}$$

where m is the mass of the particle; v is its velocity; and h is Planck's constant. It is therefore possible to convert between the measured neutron TOF and its wavelength, or energy. Detectors of the Polaris diffractometer are stationed at discrete angles; detected neutrons therefore necessarily also possess discrete scattering angles, θ. Using Bragg's Law:

$$\lambda = 2d \sin\theta \tag{2.2}$$

where d is the interplanar spacing of the sample lattice, it is entirely possible to relate neutron TOF to the crystallographic structure of a given sample.

Polaris provides two key benefits in the context of a neutron total scattering investigation. The first is the broadness of data in Q-space that it is possible to collect on the diffractometer. The advantage of this is twofold: firstly, evidence of diffuse scattering in the low-Q region may be obscured by the presence of Bragg peaks, thereby requiring a larger range of data for observation; secondly, an ideal PDF would be produced with as large a value of Q_{max} as possible, for the most accurate Fourier transform calculation. As Polaris is capable of achieving Q_{max} values of greater than $30\mathring{A}^{-1}$, it is ideally placed for use in total scattering analysis. The second benefit of Polaris is the ability to place samples of interest in a vacuum tank environment, which naturally decreases background contributions to the signal, thereby improving overall signal to noise ratio.

It is worth re-mentioning that X-ray total scattering investigations are entirely feasible scientifically. In the context of the analysis of MPEAs, however, the use of X-rays as an incident radiation source for scattering may be problematic, depending upon the composition of a given alloy. Many of the metallic elements used in the manufacture of MPEAs possess similar atomic numbers, as evidenced by their proximity to one another in the periodic table. Electromagnetic scattering scales with atomic number, thereby making adjacent atomic species near-indistinguishable from one another and obscuring the ability to identify the enhancement of particular atomic structures. Neutrons, however, do not suffer the same concerns: scattering lengths vary by atomic energy and may possess both positive and negative values. Given that the value of atomic energy may be wildly different for adjacent species, it is therefore more likely to distinguish configurational motifs in the system when using neutron scattering.

2.1.2 Powder metallurgy

Total scattering requires, by definition, the use of powder samples, such that isotropic scattering data may be collected across all of Q-space. Concerns may be raised, therefore, over the introduction of sample texture through the manufacture and processing of the powder material. In order to address this particular consideration in each of the following experimental chapters, the atomisation of alloy samples is performed to produce a crystallographic powder. Gas atomisation - the technique performed for both practical investigations in this work - involves the heating and melting of alloys prior to blasting with inert argon gas. This ideally produces approximately spherical powder particulates of the alloys of interest, in a random quenched form. Samples in this body of work are subsequently heat treated to produce chemical homogeneity and remove dislocations from the material as required.

2.2 Total Scattering Diffraction

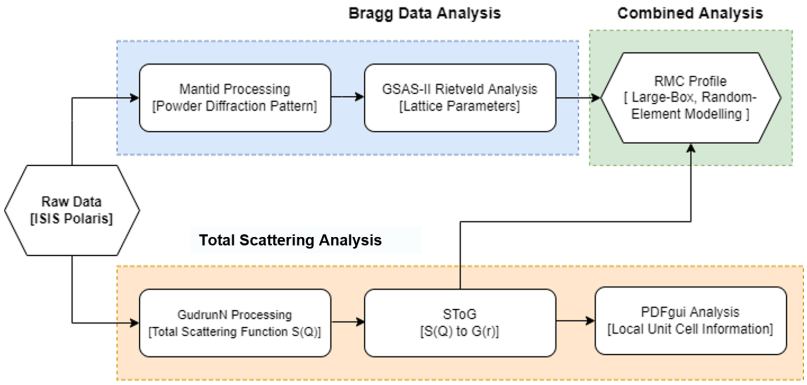

Figure 2.1: A flowchart demonstrating the various data processing stages associated with the neutron total scattering process. Note: each stage here is presented for a specific piece of software used for the work presented in this thesis. Alternative softwares are available for the processing of neutron total scattering data, and are increasingly employed by researchers.

As described previously, neutron total scattering requires the collection and processing of both traditional Bragg data and background, diffuse scattering collectively. The techniques required to process these data are, therefore, complementary but distinct. A flow chart, presented in Figure 2.1, demonstrates the stages of the total scattering analysis process; the following sections address the majority of these stages in turn, and in the order that each was applied in the following experimental chapters.

2.2.1 Mantid Processing

Mantid is a software capable of processing and analysing the data produced by neutron sources. Its role is, in summary, to collate raw neutron diffraction data and perform necessary data merging across banks of the diffractometer, ultimately producing files that are compatible with later processing software.

The Polaris diffractometer (as described in Section 2.1.1) possesses 3008 detector tubes, spread across five grouped banks. Though nominally stationed at discrete angles, these detector banks each have an associated range over which neutron detection can occur, in turn impacting the path length for incident neutrons. Each diffraction cycle therefore requires an initial calibration for all detectors, a calculation that Mantid ultimately uses to group diffraction data coherently. The data is also normalised against a Vanadium standard - selected for its near-zero neutron scattering length - to place all data along a calibrated scale.

2.2.2 GSAS-II

Following Mantid processing, the analysis of data may begin. GSAS-II (General Structure Analysis System II) [54] is a software package commonly used in the structural refinement of neutron scattering data. The software makes use of a Rietveld least-squares minimisation method [55] to refine a crystallographic structure to Bragg diffraction data; thus, its use represents the first analytical stage in any total scattering study, providing key crystallographic about the average structure for use in later modelling efforts. The Rietveld refinement method has become near-ubiquitous in the characterisation of crystal structures, and GSAS in particular provides a number of crucial material and instrumental parameters for structural refinement. Though the following does not represent an exhaustive list, values available for refinement include: structural properties, such as lattice parameters and atomic positions; the sample background, accounting for signal noise introduced internally by the diffractometer; and peak shape parameters. Further properties - including those required for the consideration of sample texture - are available for refinement, but should not be required if the refining dataset is representative of a true crystallographic powder.

As a refinement software, GSAS (and indeed the Rietveld method as a whole) necessarily requires an initial structure for refinement. In the experimental chapters, each material investigated was single phase; initial parameters were therefore approximated from elemental values. From these initial values, a theoretical crystal structure is computed by the software; Bragg's Law calculations provide a description of peak positions for the sample, comprising a series of delta functions at the predicted locations of diffraction maxima. Subsequent convolution with a pseudo-Voigt peak profile provided by a standard crystal and diffractometer contributions - accounting for instrumental and sample-derived broadening - produces a diffraction pattern more reminiscent of the true dataset,

which is then ready for parameter-based refinement.

Several of the parameters refined during GSAS fitting require close attention, primarily for their impact on later large-box modelling efforts. In particular, the diffractometer constant terms $DifA, DifC$ and $Zero$) play an important role in the conversion of data from time-of-flight (TOF) into $d-$ or $Q-$space units during calculation. These instrumental parameters are mathematically associated by the quadratic relation:

$$t = \text{DifC}\ d + \text{DifA}\ d^2 + \text{Zero} \tag{2.3}$$

where t is the time of flight for the diffractometer; and d is the interplanar lattice spacing. The $DifC$ parameter is particularly worthy of note, as it is defined by the geometry of the diffractometer instrument according to the relation:

$$\text{DifC} = \frac{2m}{h}\ L \sin(\theta) \tag{2.4}$$

where m is the mass of a neutron; h is Planck's constant; L is detector path length; and θ is the neutron scattering angle. These values will be optimised during the refinement process, and are required in the SToG Gudrun Offsets (Section 2.2.4) to account for the different ways in which Mantid (Section 2.2.1) and Gudrun (Section 3.3.2) handle the conversion between TOF and Q units.

2.2.3 GudrunN

Gudrun [56] is a software package developed for the processing of total scattering data, comprising GudrunN and GudrunX. GudrunN is responsible for the processing of raw neutron diffraction data, applying post-processing to yield refined total scattering functions; GudrunX is a near-identical software used in the processing of X-ray scattering data. Processing accounts for a number of corrective calculations, including beam count and normalisation, self-scattering component calculation, and background considerations. Post-processing allows for the merging of datasets between diffractometer banks, followed by the generation of both a total scattering function, $F(Q)$, and an error-corrected pair-distribution function (PDF), $G(r)$. The following list covers a number of key processing and post-processing calculations in further detail, though the list is non-exhaustive.

Processing:

- **Data normalisation:** In line with prior Mantid processing, it is necessary to place neutron scattering data on an absolute scale across Banks of the diffractometer. To this end, a vanadium standard - again selected for its negligible neutron scattering length - is typically placed inside the neutron beam and bombarded for an equivalent time to any experimental samples. This provides a comparative dataset for normalisation.
- **Sample background:** As with any diffraction experiment, scattering may be produced unintentionally by objects intersecting with the beam. A default contribution would be produced by the environment in which a given sample is held: the atmosphere it is held in, and the sample container. Further background contributions may be provided by experimental considerations, such as the scattering produced by a cryostat or furnace.
- **Self-scattering:** As mentioned in Section 1.4, samples produce a non-negligible amount of self-scattering brought about by the interaction of neutrons with atomic nuclei without correlation to their neighbouring atoms. Given that GudrunN is designed to calculate and produce $G(r)$ functions, it is at this stage that such corrections must be introduced to the data.

Post-processing:

- **Bank merging:** Similarly to the concerns addressed by Mantid (Section 2.2.1), GudrunN necessitates post-processing according to the grouping of diffractometer detector banks. The Gudrun software also accounts for any anomalous results produced by faulty or otherwise improperly functioning detectors.
- **Minimum radius correction:** It is anticipated that the PDF, once calculated, is flat below the shortest nearest neighbour distance. This is intuitive: if the PDF acts as a weighted histogram of interatomic distances, then there should be no contribution to the PDF at distances too small for atoms to realistically be located. This post-processing parameter simply forces the flattening of the PDF below a chosen distance.
- **Lorch function:** This function acts to remove high-frequency noise in the PDF, removing the impact of so-called 'Fourier ripples'. Such ripples are a mathematical artefact produced by the Fourier transform calculation, and can appear as small 'peaks' across the PDF. Given that such noise can impact later modelling efforts, the Lorch function is designed to remove them where possible, though its application brings a simultaneous loss of resolution.

In summary, GudrunN is capable of producing a merged, corrected, and normalised $F(Q)$ of neutron diffraction data for a given sample material; the software then performs the pre-requisite Fourier transform to produce a $G(r)$ function describing the probability distribution of adjacent atoms in

the lattice. To perform the above calculations accurately, GudrunN requires a value for the atomic density of the experimental sample prior to iteration; as such, the refined lattice parameter and calculated density (atoms/$Å^{-1}$) provided by GSAS-II processing are a parametric requirement for this analytical step. The use of GudrunN therefore typically constitutes the first stage of total structural modelling, but the *second* stage of a total scattering investigation as a whole.

2.2.4 SToG

$F(Q)$ to $G(r)$ – commonly abbreviated to SToG – is a sub-routine of the wider RMCProfile [57] software package designed to exclusively perform the Fourier transform of the reciprocal $F(Q)$ total-scattering function into a real-space PDF for neutron scattering experiments. Though this calculation may be performed by GudrunN during its post-processing routine, as described above, SToG necessarily produces a series of output files compatible with use in later modelling efforts.

As the programme is run through the command terminal, the user may produce an input command file containing the selected parameters for calculation of the $G(r)$. These include the atomic density, $DifA, DifC$ and $Zero$ values determined by GSAS-II, as well as the merged intensity $F(Q)$ (.mint) file produced by GudrunN. A further benefit of this form of input is the ability to quickly edit and assess the limits of the Fourier transform calculation - the scattering vectors, $Q_{\min}$ and $Q_{\max}$. An ideal Fourier transform would be performed over *all* space, to infinity; given that a diffractometer naturally cannot collect scattering data over an infinite range, upper and lower limits for the Fourier transform are selected in the form of Q values (see: Equation 1.9). Furthermore, random fluctuations in the system prevent the data from becoming perfectly smooth at high values of Q, in turn impacting the Fourier transform through the inclusion of high-frequency noise. As such, it is beneficial to maximise the range of Q-space considered in the Fourier transform calculation, whilst maintaining a reasonable upper limit in Q. Rapid processing allows for observational selection of the 'most appropriate' Q-limits by analysing the produced PDFs. Across the following studies, a number of parametric input files were produced for each diffraction dataset across a range of $Q_{\max}$ values. The subsequently generated $G(r)$ files were then plotted against one another to determine the most desirable $Q_{\max}$ value for further investigation.

Importantly, the SToG calculation is performed using a scaling parameter, hereby referred to simply as a 'scale value'. This near-arbitrary scaling is performed to somewhat offset any miscalculation in the atomic density or packing during processing and refinement. A value of $\frac{1}{y_{scale}}$ is applied to the dataset prior to further offsetting, in order to bring data in the low-r region closer to a physically correct set of values. The scale value selected during SToG processing is found to have a significant impact on the quality of later large-box modelling; an incorrectly selected scaling parameter is found to impact the χ^2 goodness-of-fit substantially when fitting to the calculated PDF. SToG therefore represents a key stage in the processing of neutron scattering data ready for structural analysis.

2.3 Structural Modelling

2.3.1 PDFGui

Small-box modelling analysis - occasionally referred to as a 'real-space Rietveld' method - allows for the modelling of an averaged unit cell through the refinement of a $G(r)$ PDF from prior processing. For the following work, such modelling has been performed in PDFGui [58], a small-box modelling software designed to fit PDF data. Within the context of a total-scattering investigation, the use of PDFGui represents a 'first-step' in the quantitative analysis of short range order. Importantly, PDFGui allows for the least-squares refinement of key parameters, as in a traditional Rietveld fitting, for use in later large-box modelling. More specifically, refined model parameters include the unit cell parameter; Q_{Damp} and Q_{Broad} instrumental parameters; the scale factor for neutron scattering data; and a linear atomic correlation factor, δ.

Q_{Damp}, Q_{Broad} and δ are associated corrective parameters controlling PDF peak widths. Q_{Damp} describes the form of the Gaussian dampening applied to the PDF, in the form:

$$B(r) = \exp \frac{-(rQ_{\mathrm{Damp}})^2}{2} \tag{2.5}$$

This function applies a Gaussian damping to the PDF, accounting for the finite resolution of the diffractometer that broadens peaks and reduces intensities at high r. Along with the above dampening considerations, a corrective parameter for peak broadening across the Q range is required; Q_{Broad} therefore provides a mathematical description of peak broadening due to the inclusion of noise at high Q values (in turn governed by diffractometer resolution).

The final key parameter listed above is the linear atomic correlation factor, δ, which corresponds to the behaviour of paired atoms in the system. There are, in fact, two δ values available for refinement in the PDFGui software - the aptly named δ_1 and δ_2 parameters. For the purposes of the following thesis, it is only important to note that - whilst the two values are highly correlated to one another - the δ_1 value is used to describe correlated motion at high temperature, and the δ_2 parameter is conversely used to describe correlated motion at low temperature. The δ_1 parameter would therefore be ignored in a cryostat study; δ_2 would be ignored in a furnace study. The relation of these parameters to one another and to the Q_{Broad} parameter is provided by the expression:

$$\sigma_{ij} = \sigma'_{ij}\sqrt{1 - \frac{\delta_1}{r_{ij}} - \frac{\delta_2}{r_{ij}^2} + Q_{\mathrm{Broad}}^2 r_{ij}^2} \tag{2.6}$$

where σ_{ij} is the peak width; and σ'_{ij} is the peak width without correction for broadening. Over large r distances, the motion of atoms in a crystal system is typically unrelated; at short distances,

however - i.e. to within a distance of a few atomic bonds - the motion of a given atom will demonstrate a greater correlation in the movements of its nearest neighbours. Paired atoms with a high value of the δ_1 parameter, for instance, will therefore display a greater degree of correlated motion than those with a low value of δ_1. This is perhaps more intuitively understood as the degree of 'stiffness' in the bond between adjacent atoms: two atoms with a high value of δ_1 between them behave as though they are connected with a stiff 'bar'. If all atoms in the system were connected in this manner, peaks in the PDF would all be of equivalent width. Two atoms with a low value of δ_1, however, will behave as though connected by a loose 'spring', causing an increase in peak width with increased atomic separation.

Through the refinement of the above parameters, PDFGui produces a mathematical fit to the PDF produced by SToG, in turn providing an initial indication of ordering in a given system via averaged unit cell information. As described previously, the PDF represents a weighted histogram of interatomic distances, which is fully described by a series of partial functions corresponding to the interatomic spacing of atomic pairs; by extension, differences in the experimentally determined PDF and the $G(r)$ calculated by PDFGui may indicate ordering behaviours at the local level. The weighting of the partial functions and their impact on the form of the total PDF can therefore indicate the enhancement of particular atomic pairs at a distance r from the origin.

Though a useful indicator of potential chemical SRO at the local level, PDFGui analysis cannot be used to definitively state or assess SRO across bulk material. By fitting to a small-box - assuming an overall infinite translational periodicity for the unit cell, as with earlier Rietveld refinement - the method is inherently biased towards providing information over local distances. Given that analysis of SRO-type behaviours requires information over a number of coordination shells, much larger boxes are required to capture information that is otherwise 'averaged' in the wider system.

2.3.2 RMCProfile

A more physically representative description of local ordering in complex materials may be produced through large-box modelling. Though a number of techniques exist for modelling systems containing many atoms - such as Molecular Dynamics (MD) or Density Functional Theory (DFT) simulations - the primary focus of the following work will be the Reverse Monte Carlo (RMC) method, via RMCProfile [57], which employs an iterative approach to fitting against the Pair Distribution Function.

As is suggested by the name, large-box modelling involves the generation of a large box, or 'supercell' - containing information on many thousands of atoms - by fitting partial PDFs to experimentally determined data. An initial box is provided to the RMCProfile software for preliminary calculation, containing some pre-defined arrangement of atoms according to the crystallographic properties

determined by Rietveld refinement. In a similar fashion to previously described small-box modelling efforts, an initial PDF for the structure is then calculated by the analysis software. If the atoms of the input supercell are all located on their original lattice sites, the initially calculated PDF will constitute a series of delta functions at discrete distances corresponding to the coordination shell distances of the crystal lattice. It is entirely possible to begin fitting from this position, though a more physically representative model may be generated through the application of small, 'random' Gaussian displacements to constituent atoms, moving them away from their ideal lattice sites and broadening calculated PDF peaks. From this starting position, a number of scattering functions may be produced and compared to experimental data. A χ^2 goodness-of-fit factor is calculated and used to describe the quality of agreement between the starting configuration and experimentally derived PDF, according to the standard expression:

$$\chi^2 = \sum_j \frac{(y_j^{exp} - y_j^{calc})^2}{\sigma_j^2} \tag{2.7}$$

where j is a given data point; y_j^{exp} is the experimental value at point j; y_j^{calc} is the calculated value at point j; and σ_j is a weighting factor for the data. During the iterative refinement process, random translations or swaps are generated within the model, according to set probabilities provided by the user, altering the lattice structure and chemical occupations of the supercell. Translations are confined to a specified distance window from the ideal lattice positions, preventing the generation of non-physical structural solutions, and correspond to lattice distortions or thermal contributions to the PDF; swaps simply alter the chemical ordering of the model. Moves are applied at random; if the applied constraints are satisfied, the RMC software will then calculate new scattering function datasets and a corresponding value of χ^2 for the new configuration. If the change in χ^2 ($\Delta\chi^2$) between configurations is less than zero -i.e. the χ^2 value is reduced, demonstrating a closer fit to the experimental data - the newly generated supercell is taken as a starting configuration and the process iterated.

Occasionally, 'bad moves' – that is, moves for which $\Delta\chi^2$ is greater than zero – are accepted by the algorithm. The probability of acceptance for these moves is given by the expression:

$$P = \exp \frac{-\Delta\chi^2}{2} \tag{2.8}$$

Accepting a number of 'incorrect' moves according to a probability distribution prevents the algorithm from becoming 'trapped' in false minima. The full algorithm for the RMC method is presented in Figure 2.2 for clarity. Ultimately, the RMC large-box modelling method produces a three-dimensional model of the system in question with the closest possible fit to experimental

data. This model is unconstrained by symmetry relations – unlike the small-box modelling method – and can produce much larger models for the analysis of short-range order. There are, however, a number of drawbacks to the method.

In the following work, the $D(r)$ function - that is, the r-scaled $G(r)$ function - is refined against in RMCProfile. This is to best capture oscillations in the high-r region, which are significantly reduced in size when refining against the $G(r)$.

The nature of the Reverse Monte Carlo method - that is, attempting to fit a number of parameters and properties to two-dimensional data - necessarily produces a number of possible 'solutions' for any single fit to experimental data. The RMC method generates a configuration that abides by the constraints of the experimental PDF. Ideally, it therefore provides a 'maximally disordered' solution within the bounds of the data and physical constraints, though the final result can be influenced by the starting model and specific RMC parameters. This can be beneficial: any atomic ordering consistently found to be introduced to the system by RMC fitting may be more confidently assumed to be present in the experimental sample. However, it is therefore also entirely possible to bias a system towards a given structural solution with a poorly constructed input supercell, or for fitting to mathematically enter a 'false minimum' from which it cannot escape. To avoid such concerns in the following experimental chapters, initial input boxes for RMCProfile fitting typically contain a random distribution of constituent elements unless otherwise specified; any local ordering then built into the boxes by RMCProfile may therefore be taken to be the likeliest representation of potential ordering behaviours in experimental samples. It is, however, also entirely possible to

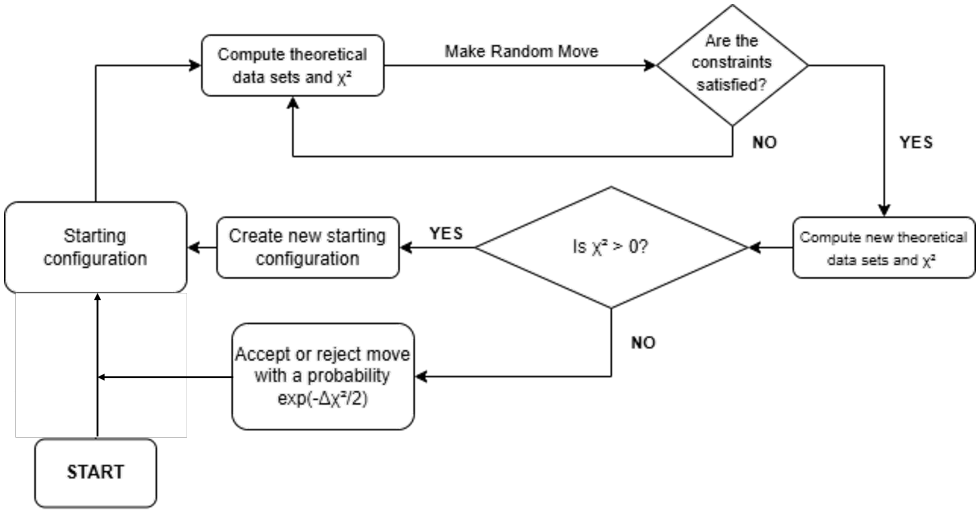

Figure 2.2: An overview of the RMCProfile algorithm.

begin the fitting process with a box containing known order over some domain size. This in effect 'guides' the algorithm towards a solution that is more in-keeping with known or assumed structural information.

There are a number of factors involved in the quality of fitting, and the extent to which we can deem a solution to be 'accurate', As described above, it is entirely possible for multiple solutions to accurately fit to a given PDF mathematically. In Section 2.2.4, it was raised that an incorrectly selected scale factor for a given dataset can significantly impact the quality of fit, ultimately impacting the validity of configurational analyses. This is equally true of a number of parameters present in the RMCProfile suite, and is particularly true of the 'resolution correction' parameter. The resolution correction parameter is a high-r corrective parameter designed to accommodate signal noise at high values of r. As previously mentioned, the finite resolution of the diffractometer dampens high-r PDF peak intensities, and failure to account for this effect would lead to erroneous atomic displacements due to the spread. It functions in much the same fashion as the Q_{damp} parameter in PDFGui, and takes a single value. If left unrefined, or inaccurate, this value can have a significant impact on the quality of fit at "large" distances from the origin; to this end, it is important to identify an ideal 'parameter suite' of values to ensure fit quality. For the purposes of the following work, this constitutes refinement of the scale and resolution correction parameters specifically. In each RMCProfile investigation, a range of scale and resolution correction parameters will be selected, paired, and analysed; if ten resolution correction parameters and ten scale values are selected, then 100 runs of the RMCProfile refinement will be assessed for their quality of fit. In each case, arrays of the values will be assessed for the lowest identifiable χ^2 value.

It is also worth raising that the RMCProfile software cannot, at present, reproduce the ordering present in multi-phase materials. Lattices of a single crystallographic structure that possess multiple chemically ordered regions may be modelled - indeed, the following work relies on the ability of the method to identify multiple chemical motifs in a single supercell. If, however, two phases do not share crystallographic structural properties - presenting with a difference in lattice parameter or space group - then the method cannot be used to identify chemical order. A number of studies are presently attempting to rectify this concern [59]. It would be remiss, however, not to identify this as a cause for concern with regards to the application of the method for the analysis of SRO in complex materials.

Chapter 3

CrCoNi

3.1 Introduction

The CrCoNi ternary alloy - occasionally referred to as a 'medium entropy alloy' - is an ideal candidate for the investigation of local atomic ordering via the total scattering technique. Like any multi-principle element alloy, it comprises a single-phase solid solution with a nominally random distribution of constituent atomic elements, typically in equimolar or near-equimolar concentrations. As a derivative of the CrMnFeCoNi family of MPEAs, CrCoNi has been investigated for its short-range order properties on a number of occasions, predominantly for its mechanical merits. CrCoNi has been noted for its high-strength, high-ductility properties at cryogenic temperatures [60], and has been recommended on a number of occasions for use in low-temperature applications such as nuclear fuel containment [61]. Indeed, some studies have suggested that the cryogenic damage-resistance and strength properties of the CrCoNi ternary alloy are superior to those of the CrMnFeCoNi MPEA, which itself has been highlighted and studied for its exceptional mechanical performance. [62].

One mechanism by which these impressive properties have been suggested to arise is an improved resistance to dislocation glide [63], which many studies have attributed to an as-yet uncharacterised CSRO structure in the system. To date, investigations into the local atomic ordering of multi-principle element alloys have been restricted to predictive modelling techniques or the inference of short-range order via traditional characterisation routes. This lack of empirical characterisation, however, has predictably led to inconsistencies in the reporting of local ordering across many systems. In the case of CrCoNi, an investigation by Yin *et al* [60] found little evidence of short-range ordering behaviours when using DFT modelling techniques. A linear Hall-Petch scaling relationship

was used to infer the *likely* absence of SRO behaviours across a range of processing conditions from literature, and the authors demonstrate no correlation between CSRO and the strength properties of the material. Work by Zhang *et al.* [64], however, reports evidence of ordering behaviours in contradiction to the Yin study, though without an associated link to mechanical behaviour. Background-corrected TEM studies of the CrCoNi ternary appear to demonstrate 'diffuse streaking' along the [111] lattice-direction. These streaks are a common phenomenon, and can indicate the presence of a multitude of lattice-effects, including SRO structures. The study implies a degree of confidence in the presence of local ordering due to the enhancement of these diffuse scattering traces upon ageing of the material; samples aged at 1000 °C (1273 K) show more prominent streaking patterns, indicating the potential formation of SRO consistent with high temperature atomic mobilities.

The results of the Zhang *et al.* study are not unique: a separate study by Zhou et al [61] used hot-forged plates of CrCoNi for a TEM and HAADF-STEM diffraction experiment, in order to characterise the structural behaviours of the alloy. FFT results along the [112] zone-axis show the presence of FCC super-lattice reflections between the origin and $\{\ \overline{3}11\}$ planes, and the simultaneous appearance of diffuse 'discs' approximately ten times larger by diameter than the primary diffraction maxima. The authors infer the presence of lattice features at approximately the scale of inter-atomic bonds from these phenomena, theoretically suggesting the existence of SRO-type ordering behaviours in the material. Further IFFT analyses demonstrate extra reflections at $\frac{1}{2}\{\overline{3}11\}$, concluding that the ordered regions (of which there are reportedly over 300 within the 35nm objective aperture diameter) must possess CSRO approximately twice the size of the $\{\overline{3}11\}$ interplanar spacing.

The results of the TEM study were supported by a further EDS line-scanning analysis of the CrCoNi system, specifically focusing on the creation of EDS maps over the regions in which CSRO was reportedly located. The intention behind this particular study was to determine the *character* of the ordering behaviours, rather than simply identify its presence. Indeed, the authors present an overall structural solution for the alloy: Cr-enriched planes appear to alternate with Cr-depleted planes, suggesting - through the analysis of spatial distribution functions over the enriched columns - that 'like' atoms appear to primarily avoid bonding in the first instance. Cr atoms are theorised to preferentially distribute towards the corners of the CrCoNi unit cell, though no further analysis to suggest this result is presented.

It is worth noting, at this juncture, that there exists an increasing body of work suggesting that the origin of diffuse scattering - a primary method for the identification of CSRO in metallic materials - may not be limited to atomic ordering in the first instance. Walsh *et al.* have recently reconsidered the presence of diffuse streaking in CrCoNi specifically, proposing that 'symmetry breaking effects' may be an equally valid explanation for the phenomena [25]. Nanoscale planar defects, such as

stacking faults, are shown to produce $\frac{1}{2}\{311\}$ diffraction maxima by breaking the symmetry of the reciprocal lattice; by extension, the authors point to even smaller defects as the cause for diffuse maxima. As mechanical deformation and irradiation have been shown to increase the presence of diffuse scattering, it is possible that the formation of faulted loops or stacking-fault tetrahedra is responsible for the appearance of such streaking in CrCoNi samples. Equally, the authors point towards so-called 'relrod spiking' - the appearance of diffraction maxima as an artefact of scattering from higher-order Laue zones - as a potential source of diffuse scattering, though it is noted that the predicted intensities of these phenomena in CrCoNi is negligible. This skepticism is echoed by Coury *et al.* [65], who have themselves disputed the efficacy of TEM analysis in the characterisation of short-range ordering behaviours. The diffuse scattering historically attributed to a range of crystalline features (such as stacking phenomena, and short-range ordering) is re-evaluated, and hypothesised instead to arise from reflections 'projected' by first-order Laue zones adjacent to the Ewald sphere associated with the diffraction experiment. Extra reflections in the diffraction pattern are, broadly, attributed to the difference in scattering factors between constituent elements, bringing about a non-zero structure factor when the 'randomness' of the structure is deviated from. Improperly prepared samples - i.e. those are not appropriately thin - or materials that contain elements with very similar scattering lengths could therefore present a greater degree of diffuse scattering that is not attributable to local atomic ordering. In a separate associated work, Bacurau *et al.* go on to suggest the use of Differential Scanning Calorimetry (DSC) analysis as an alternative method for the discernment of local ordering behaviours alongside TEM studies [66]. Exothermic reactions are hypothesised to occur with the formation of CSRO regions, while endothermic reactions are hypothesised to occur with the destruction of SRO; from here, the enthalpy of SRO may be evaluated against a baseline value to provide a measure of the extent to which a given sample possesses SRO.

Existing models of the CrCoNi system are often conflicting, and the exact form of ordering - should it exist - remains open for debate. Warren-Cowley parameters calculated for the first coordination shell of the material via DFT analysis seemingly demonstrate a strong disinclination for the formation of Cr-Cr pairs, along with a comparatively weak repulsion for both Co-Co and Ni-Ni pairs [67]. Of the remaining atomic pairings in the first coordination shell, the formation of Cr-Co and Cr-Ni bonds are seemingly favoured. Typically, this is interpreted as the segregation of Cr atoms at the local level, producing either an $L1_2$-type ordering to minimise Cr-Cr nearest neighbour pairings or an $L1_1$-type ordering of Cr on alternating atomic planes. Some have even gestured towards experimentally derived results on the magnetic behaviours of Ni and Cr atoms to justify the structure further [68]. These results, however, are not universally agreed upon: the only existing study that makes use of interatomic potentials to model the structure of the CrCoNi alloy (in a hybrid *Ab initio* - VASP - and Monte Carlo approach) appears to show strong bonding preference for Ni-Ni pairs, in direct contradiction with the above results [67]. In an effort to produce a definitive solution, a number

of studies have moved towards machine learning potentials to model the CrCoNi structure; though the work is ongoing, they appear to fall into agreement with the Cr segregation model.

Given, therefore, the degree of uncertainty associated with the analysis of short-range ordering in CrCoNi via traditional methods, the conclusions from these investigations must be taken with some caution. Although the findings of these studies are qualitatively useful in identifying the *likelihood* of CSRO, it must be accepted that a full quantification and characterisation of atomic ordering behaviours has not yet been achieved. Equally, the above results are not without merit. Each has been used to inform the analysis of mechanical experimentation on the CrCoNi system, including compression testing, nano-indentation testing, and bulk tensile testing. In all cases, the results of the tests are stated to be an emergent property of the short-range ordering in the system: the increased planarity of dislocation slip is attributed to an increased degree of SRO in the material; increased hardness and yield strength are ascribed to improved stacking fault energies resulting from SRO domains. Without a full description of the types and quantities of short-range order in the system, however, the extent to which such mechanical behaviours are attributable to short-range ordering is unclear.

For these reasons, the Total Scattering Diffraction analysis method is of increasing interest to those interested in studying the CrCoNi system. By combining traditional Bragg and diffuse scattering analysis techniques, it is hoped that a complete image of atomic ordering might be established, including the characterisation of local atomic motifs and structures.

3.2 Experimental Details

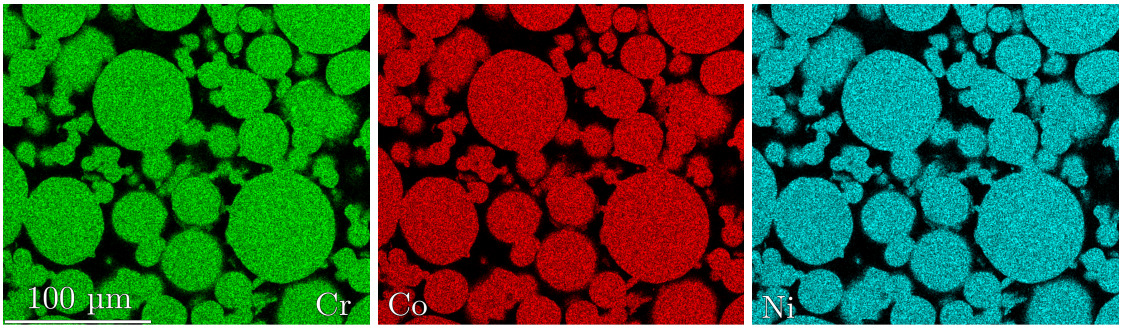

Figure 3.1: EDX Maps for the CrCoNi system as collected on the FEI Inspect F50; Cr, Co, and Ni are presented sequentially from left to right. The system appears to be single phase, randomly distributed and homogeneous as expected.

A CrCoNi powder sample of nominal atomic fraction 0.25 Cr - 0.375 Co - 0.375 Ni was manufactured via gas atomisation by Hauner Metallische Werkstoffe (Germany). A small volume of the powder was glass-sealed in an Ar back-filled quartz tube and heat treated at 1200°C for 2 hours prior to ice water quenching, providing an homogenisation process and forming a solid bar. A quantity of the powder was retained for external ICP-OES analysis at the Sheffield Assay Office. A small quantity of the CrCoNi bar was sectioned, mounted in conductive bakelite, and ground and polished for internal EDX measurements. ICP-OES analysis determined an atomic fraction composition of 0.2582 Cr - 0.3488 Co - 0.3930 Ni; the internal EDX demonstrated a reasonable agreement with these values, with 0.266 Cr - 0.375 Co - 0.266 Ni (Figure 3.1). Negligible quantities of oxygen, carbon, and nitrogen were detected during compositional analysis.

Neutron total scattering data were collected on the Polaris diffractometer at the ISIS Neutron and Muon Source (Oxfordshire, UK). The CrCoNi sample was placed into a vanadium can and subsequently loaded into a cryostat, before being fully exposed to the beam. Total scattering data for this experiment were initially gathered at near-absolute-zero (approximately 4.2K), followed by a subsequent heating ramp to ambient temperature in four increments (64K, 123K, 182K, 300K; Figure 3.2) . The heating profile for this experiment was designed to capture potential local ordering behaviours that contribute to the improved strength and damage-tolerance properties at cryogenic temperatures. Neutron diffraction data were reduced, in TOF units, using the Mantid processing software [69], and peak intensities were normalised to accommodate for neutron fluxes against a pure vanadium sample. Rietveld refinements were performed using the GSAS-II refinement software package (Section 3.3.1).

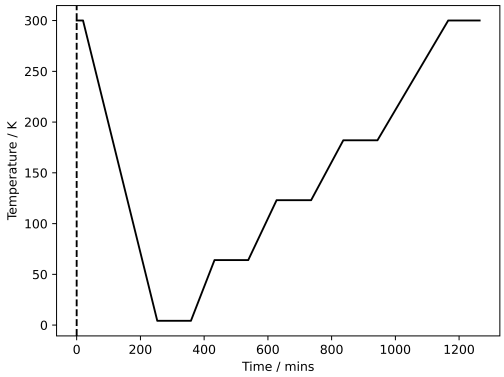

Figure 3.2: Temperature profile for the neutron total scattering experiment performed using the CrCoNi ternary alloy. The dashed line indicates a break in time, as the prior room temperature dataset remains unused.

The GudrunN software package was employed in the processing of total scattering data (producing the pre-requisite total-scattering functions), and the experimental PDFs for each temperature dataset were subsequently calculated using the SToG subroutine of RMCProfile (Section 3.3.2). More detail on the choice of parameters is provided in the sections below.

3.3 Data Processing

3.3.1 Raw Data & Rietveld Refinement

Raw, normalised Mantid processing of the Bragg diffraction data for this experiment may be found in Figure 3.3 as taken from Bank 5 of the Polaris Diffractometer, and can be well-described by a single-phase, FCC solid solution as anticipated. The fractional shifts in peak position with increased temperature are apparent in the figure.

As described above, a GSAS-II Rietveld refinement was performed for all temperature datasets. Datasets collected from Banks 3, 4 and 5 were refined to a reduced χ^2 value of less than or equal to 30.0, and an R_w value of less than 5.0, indicating a strong goodness of fit and high quality of refinement [1]. Data from Banks 1 and 2 were discarded on the basis that they did not contain sufficient crystallographic information for this study. An example of Rietveld fitting from Polaris

[1] The value of R_w demonstrates how closely the calculated data matches to observed data; χ^2 provides a comparison of this mismatch to that which is expected from the experimental uncertainty. R_w may therefore be deemed a measure of the fit quality, while the χ^2 shows the statistical significance of that fit.

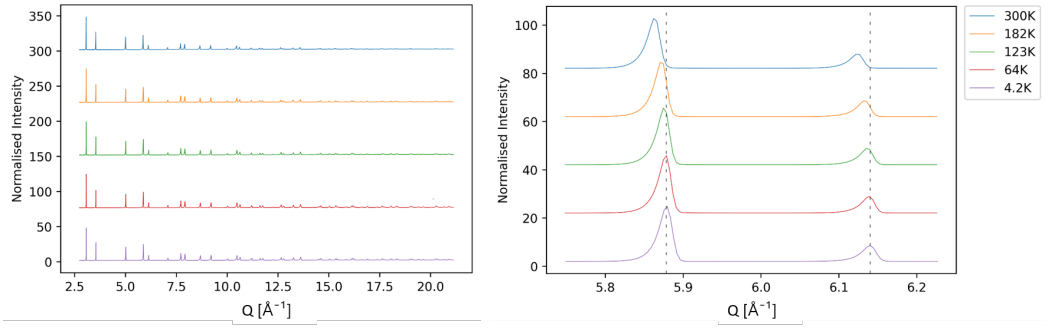

Figure 3.3: Raw normalised neutron diffraction data in Q-units for the CrCoNi system across a temperature range of 300 - 1200 K, as taken from Bank 5 of the Polaris Diffractometer. Left: Data presented for all temperature datasets over the full range in Q; Right: A slice of the data (Q=5.8-6.2 Å^{-1}) demonstrating the shift in peak position with temperature.

Bank 5 for the 4.2K dataset is made available in Figure 3.4. It is worth noting that there is a pronounced discrepancy in peak heights between the fit and data for Banks 4 and 5; these are standard data artefacts brought about by the use of Time of Flight (TOF) diffractometers (More information may be found in the Supplementary Information in [49]), such that the fitted shape does not precisely capture the form of the diffraction data.

Further results from Rietveld fitting may also be found in Figure 3.4. Certain physical properties - such as the lattice parameter and thermal U_{iso} parameter - have an intuitive influence on later structural solutions. Importantly, both the lattice parameter and U_{iso} demonstrate standard trends with changes in temperature; by extension, they can therefore be used to assess the validity of Rietveld fitting once the process is complete. Instrumental parameters, however, can have an equally significant impact on data processing. In this instance, the lattice parameter demonstrates an approximately linear increase with increased temperature as expected. The thermal U_{iso} parameter (a parametric description of thermal oscillation) exhibits an equivalent trend to that of the lattice parameter across temperature datasets, with a linear relationship at high temperature and a non-linear curvature close to absolute-zero. This non-linear region is driven by the 'minimum distance' available to atoms in the system; the lattice parameter and thermal oscillation will naturally plateau as the temperature decreases and atoms begin to experience electrostatic repulsion from their neighbours. Given that the increase in thermal oscillation of constituent atoms - described parametrically by the U_{iso} values - drives the increase in lattice parameter, the similarity in trends between graphs is an encouraging sign that the refinement has been completed successfully.

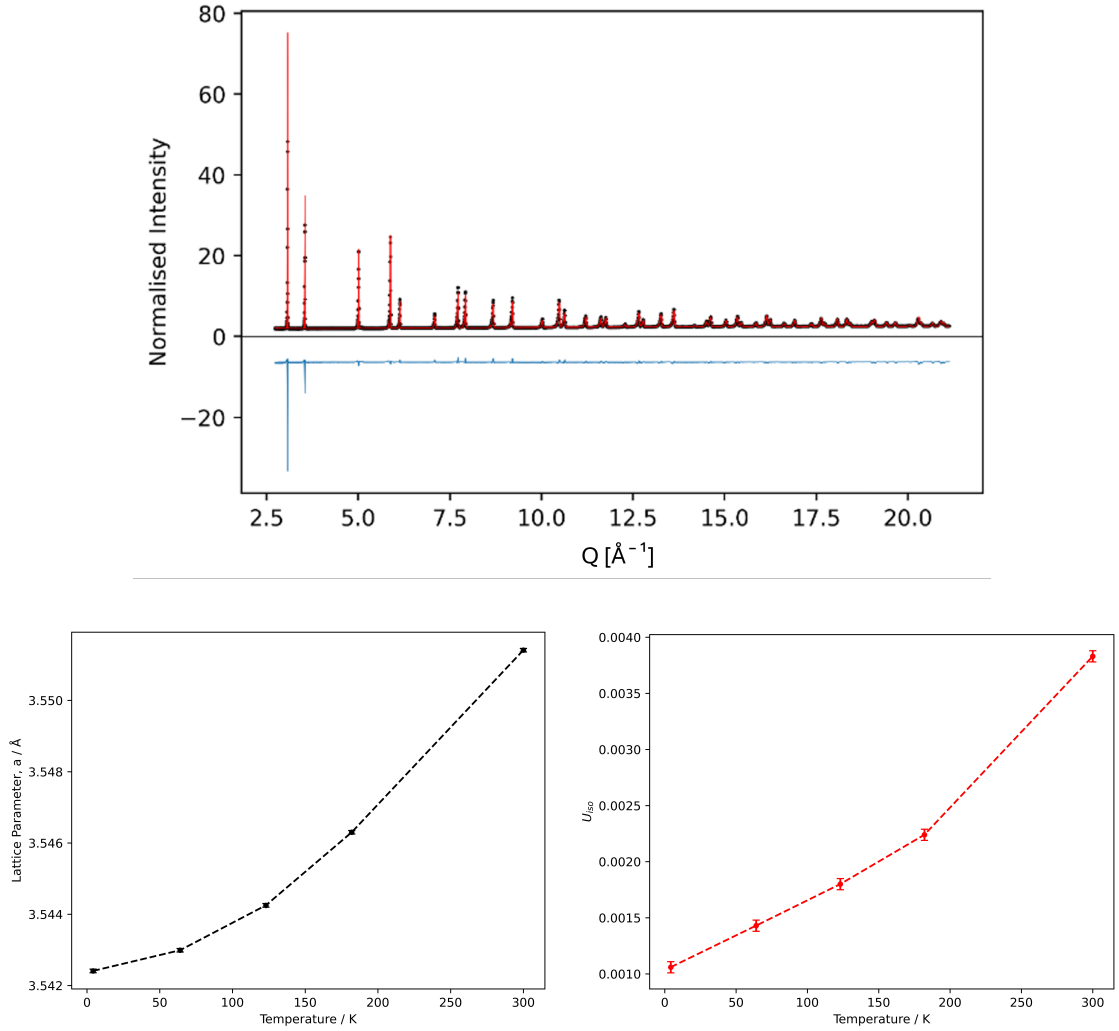

Figure 3.4: **Top:** An example of Rietveld refinement for the CrCoNi system at 4.2 K, as taken from Bank 5 of the Polaris Diffractometer. Note the discrepancy in the difference plot, an inherent feature of TOF diffractometers. Comparison plots of enhanced configurations for CrFeCoNi across the 300 - 1273 K temperature range. **Bottom:** Fitted trends between 4.2-300K for the lattice parameter, a (Left), and thermal U_{iso} parameter (Right) in the CrCoNi ternary alloy. Errors for the lattice parameter are also present, but negligible.

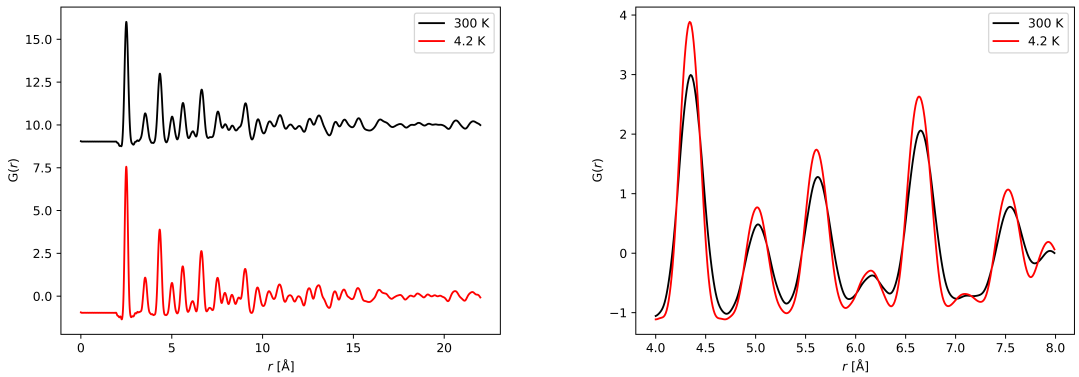

Figure 3.5: Left: $G(r)$ PDFs to 22 Å as produced by GudrunN for the CrCoNi system at 4.2 K and 300 K; Right: A section of each PDF overlaid for comparison - note the peak broadening at 300 K associated with thermal offsite displacements.

3.3.2 GudrunN PDF Calculation & SToG Processing

The following section details the processing of refined CrCoNi neutron diffraction data into the prerequisite total scattering functions for large-box modelling. This is achieved using the GudrunN and SToG softwares, as outlined in Section 2.2. A selection of the PDFs produced by this processing will be available below.

Lower and upper Q-limit bounds were imposed on the Fourier transform at 0.90Å^{-1} and 67.0Å^{-1} across all temperature datasets. For the G(r) inverse Fourier transform, a top-hat function width of 1.571Å^{-1} and a minimum radius for Fourier transform of 2.0317Å were deemed to be the most suitable parameter suite for processing, with minimal noise. The top hat function is applied as a background subtraction and smoothing operation, removing broad oscillations caused by instrumental noise and incoherent scattering while preserving sharp Bragg peaks. The user is able to specify the width of the function, effectively controlling the smoothing process for maximum information retention. Examples of the PDFs from the end-member datasets in this investigation - i.e. 4.2 K and 300 K data - are presented in Figure 3.5, demonstrating the expected broadening of peaks with increased temperature. It is worth highlighting that the PDFs at all temperatures appear to possess small artefacts about their first peak, taking the form of smaller 'peaks' or 'ticks'. The definitive origin of these artefacts remains unknown, though it is likely that they are mathematical remnants from the Fourier transform calculation itself. It was believed that such artefacts would ultimately be removed during SToG post-processing.

The use of SToG in the post-processing of G(r) data is, primarily, an aesthetic choice. SToG allows the user to quickly and intuitively select upper (Q_{Max}) and lower (Q_{Min}) bounds on the Fourier

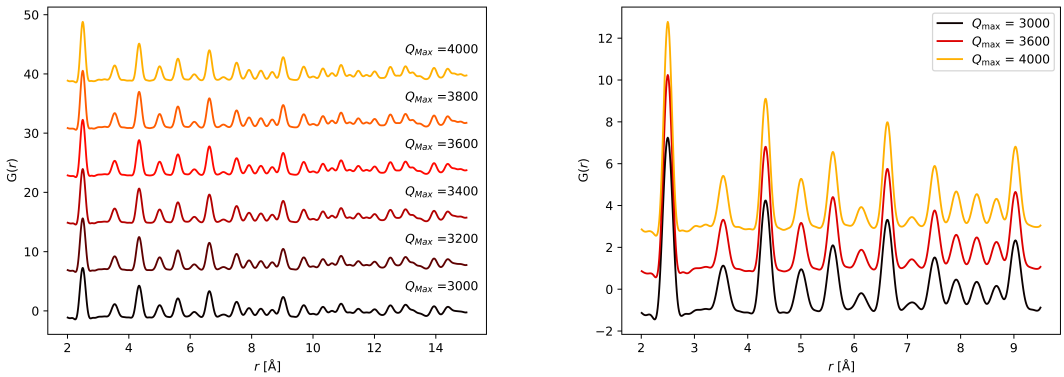

Figure 3.6: Left: SToG calculated $G(r)$ PDFs for the CrCoNi ternary alloy at 4.2 K across a range of $Q_{\max}$ values (30 - 40 Å^{-1}); Right: A comparison of PDFs when using end-member $Q_{\max}$ values, and the selected 36Å. Note the increase in Fourier ripples for the 40Åcase.

transform to produce a 'cleaner' PDF - i.e. a $G(r)$ with fewer Fourier Ripple artefacts - producing subsequent files in the format most compatible with RMCProfile fitting. The user is also able to input previously processed instrumental parameters from GSAS-II and GudrunN fitting (such as the $DifC$ parameter) to account for a known discrepancy in the way that Mantid and GudrunN perform a calculated conversion from TOF to Q units. Q_{Max} values were assessed visually for their noise-reduction across a range of values from 30 - 40 Å^{-1}. The results of this processing are presented in Figure 3.6. Ultimately, a (Q_{Max}) value of 36 Å^{-1} was deemed the most appropriate for further processing. Though figure 3.6 demonstrates very minor differences across the $Q_{\max}$ range, it is ideal to maximise the $Q_{\max}$ value used during processing; the 40Å case, in this instance, was deemed to possess more artefacts from the Fourier calculation than is desirable.

3.4 Modelling & Analysis

3.4.1 PDFGui: Small-Box Modelling

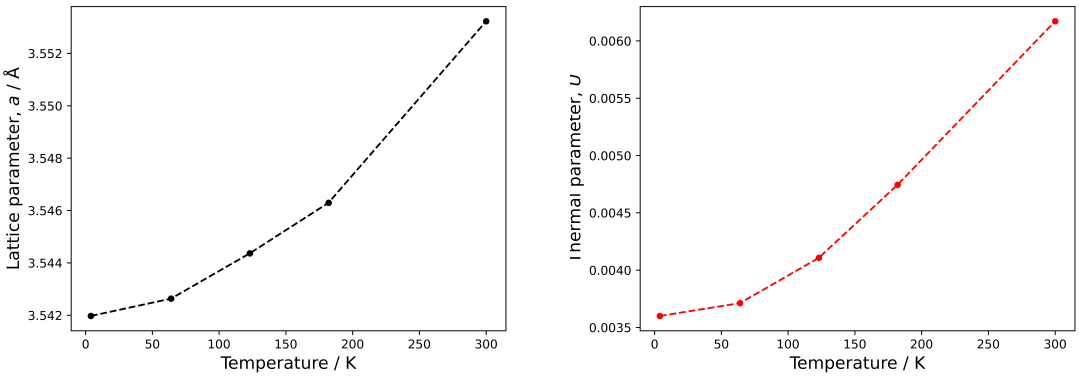

Figure 3.7: Fitted trends between 4.2-300K for the lattice parameter, a (Left), and thermal U parameter (Right) in the CrCoNi ternary alloy, as produced by PDFGui. Errors are present, but are negligible.

PDFGui fitting was performed for all CrCoNi datasets from 4.2-300 K, to assess and refine the unit cell. Refinement of the unit cell parameter, a, demonstrates the expected increase in magnitude with increased temperature, ranging from 3.542 Å at 4.2 K to 3.553 Å at 300 K; an equivalent increase in the thermal U parameter is also observed across a range of 0.004-0.006 Å^2. It is possible to further assess the efficacy of PDFGui fitting through the comparison of fitted parameters to prior GSAS-II results. Lattice parameters for both fitting regimes are equal to one another within error. Both of the aforementioned trends in the lattice and thermal parameters also demonstrate equivalent trends with increased temperature to their GSAS-II counterparts (Figure 3.7).

Small-box modelling revealed discrepancies between the data and the model, likely indicating the presence of chemical short-range order effects (Figure 3.8). Comparative differences between the two $G(r)$ profiles do not appear to obey a specific function (such as a dampening curve) suggesting chemical occupancy effects that cannot be well-described by the modelling of the unit cell. If it is therefore taken that PDFGui can indicate the *presence* of ordering but cannot quantify or clarify the specific configurations of atomic pairs, further large-box modelling is required to establish ordering effects over a larger, averaged structure. Importantly for later large-box modelling efforts, some of the parameters in PDFGui are approximately equivalent to fitted parameters in RMCProfile: it is entirely possible to use the scale value from PDFGui as an initial estimate for the scale parameter in RMC fitting, providing a reasonable 'window' within which we would anticipate finding the χ^2 minimum for that system. In this instance, the fitted scale value from PDFGui appears to be

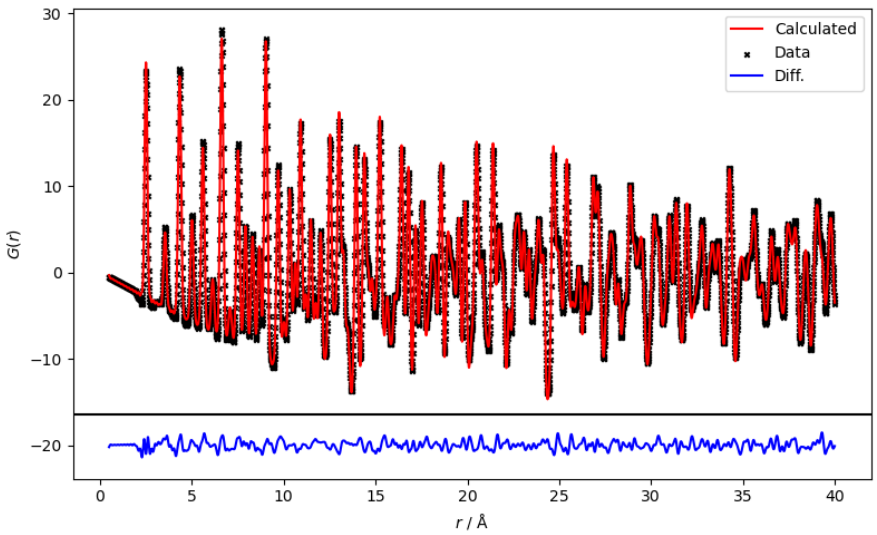

Figure 3.8: PDFGui fit to experimental data for the CrCoNi system at 4.2 K; the associated difference plot is presented below. Minor discrepancies between the experimentally derived and calculated PDFs may indicate uncaptured chemical short range order effects.

approximately equal to 1.0; we may therefore simply perform RMC fitting over a scale window in the region of 0.9-1.1. Equally, the Q_{damp} term from PDFGui fitting may be used as an approximation for the instrument resolution correction parameter in RMCProfile - as both perform high-r corrective roles to account for noise in the high Q-region of the scattering function - providing an equivalent initial value estimate. Here, the approximate Q_{damp} value for the fits is equal to 0.023; therefore, for RMC fitting, we may apply a window of values between 0.02-0.03.

3.4.2 RMCProfile: Large-box modelling

RMC fitting - random box, translations only (Grey Run)

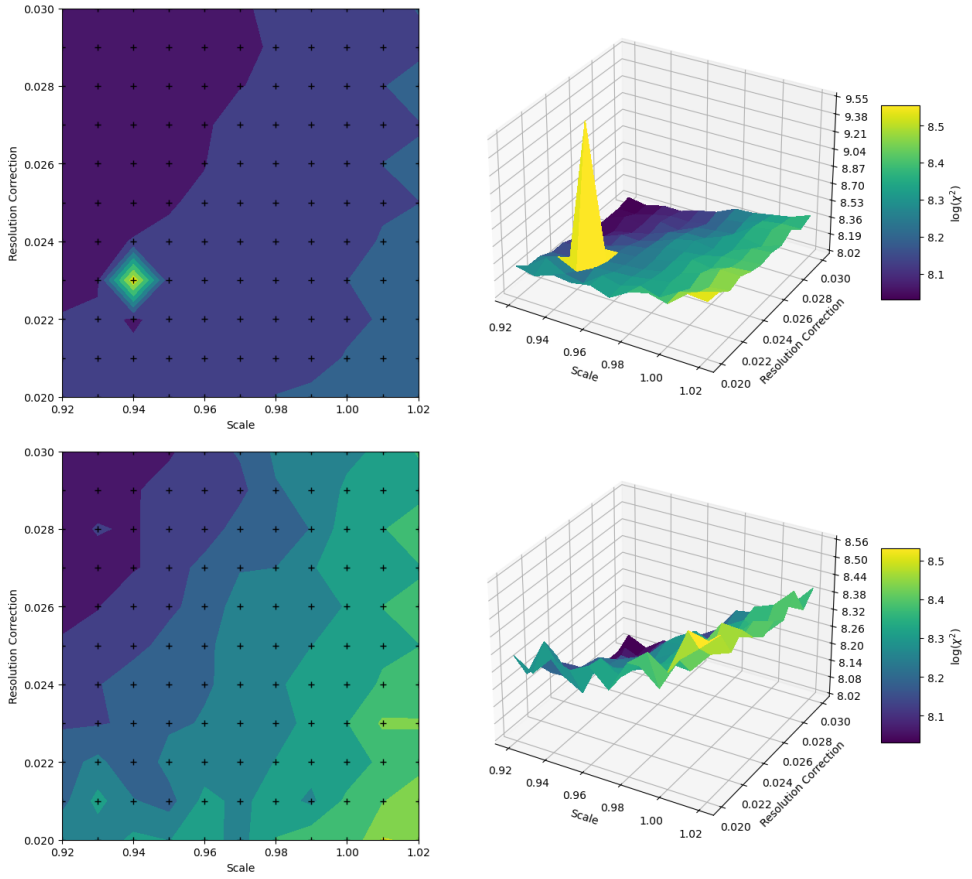

Figure 3.9: The results of χ^2 fitting for the CrCoNi system using a single atom type. ('grey' fitting). The top image contained a significant anomaly, which was removed to produce the figure below.

When performing a large-box modelling investigation in the assessment of SRO, it is typically best practice to initially fit a large-box with equivalent crystallographic properties limited to a single constituent atomic species. Fitting with a single atom type requires no 'swapping' of atomic species during χ^2-minimisation, thereby simply translating atoms from their ideal lattice sites to best match the distribution of offsite displacements described by the PDF. This provides an excellent starting point for later fitting with all chemical species, having established a 'best fit' lattice structure. Equally, a strong fit - i.e. one without much evidence for discrepancy between experimental data and the PDF calculated by RMCProfile - would likely demonstrate that the system does not possess local order; the quality of fit would be unaffected by scattering length, and therefore the system

could instead be well-described by a random distribution of constituent elements with particular offsite behaviours. For the purposes of the following analysis, fitting with a single atom type will be referred to as 'grey' fitting; a full analysis of all constituent species will be comparatively referred to as 'full colour' or simply 'colour' fitting.[2]

In the following instances, all grey runs were allowed to proceed using a minimum of 2 million translational moves for the lattice. A default atom type of Ni was used - though this in itself is an arbitrary selection - in a 20 × 20 × 20 unit cell FCC large-box containing 32,000 atoms in total. Fitting was initially performed over the full 40Å r-range available from the PDF data. The end-member 4.2 K dataset was selected for grey fitting, as it is the least likely to be impacted by thermal contributions to offsite displacement. A full range of scale and resolution correction values were analysed from prior PDFGui fitting: scale values were selected between 0.92-1.02 using a step of 0.01; instrument resolution correction values were selected between 0.02-0.03Å^{-1} in steps of 0.001Å^{-1}. Pairwise, this produced 100 simulations in total.

The final χ^2 results for grey fitting over 40Å are available in Figure 3.9. When removing the obvious anomalous result at a scale value of 0.94 - likely caused by the algorithm entering a false minimum from which it could not escape - there is a clear trend towards a low value of scale and high value of resolution correction parameter. Assessment of the calculated PDF at a scale value of 0.92 and an instrument resolution correction value of 0.03Å^{-1} demonstrates an approximate fit to the data (Figure 3.10). The difference plot appears to show moderate discrepancies between the fitted PDF and the experimental data across all of the available r-space; though not large, it is entirely possible that these differences are evidence of homogeneous ordering behaviours that are not captured by fitting with a single atom type of singular scattering length. However, the overall strength of the fit likely indicates that the offsite displacements for the structure are, in this instance, well-fitted. It is perhaps worthy of note that the scale value determined by grey fitting is substantially different to that produced by PDFGui, and indeed the best-fit resolution correction parameter (0.03 or greater) appears to significantly differ from the Q_{damp} value determined by PDFGui fitting (0.023).

RMC fitting - translations and swaps (Colour Run)

It can be assumed that the shortcomings of single-atom 'grey' fitting are brought about by the absence of site occupation by varied atomic species. For this reason, further fitting is performed in full 'colour', using all three constituent atoms in the input structure. As previously described in the methods section, RMCProfile fitting requires the optimisation of both a scaling parameter and a resolution correction parameter. By mapping the variation in the χ^2 goodness-of-fit value for each pair of scale and resolution correction values, a 'suite' of fitting parameters may be established that

[2] A full description of the fitting regimes is present in the Appendix (A.1).

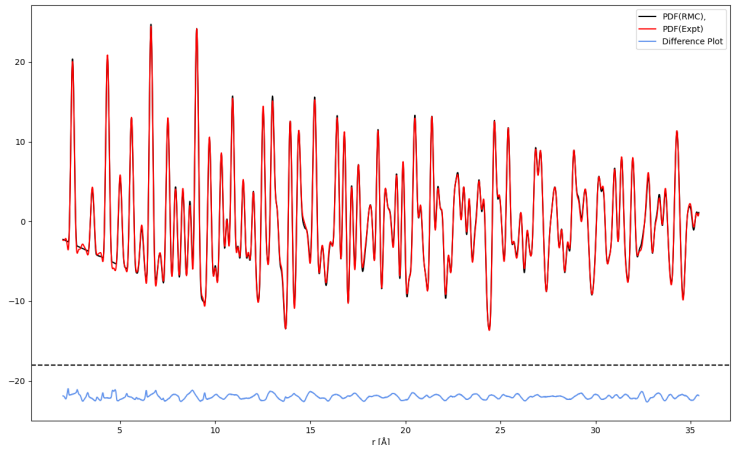

Figure 3.10: RMCProfile calculated best-fit for the CrCoNi system as modelled with a single atom type ('grey' fitting), using a scale value of 0.92 and a resolution correction value of 0.03. As demonstrated by the difference plot, there are discrepancies in the fit over the entire 40Å r-range, likely caused by chemical ordering effects not captured by grey fitting.

best represents the data for a given system. In all instances of the RMCProfile fitting described below, an initially random FCC large-box of composition 0.2582 Cr - 0.3488 Co - 0.3930 Ni was used as input. The randomness of the input structure avoids adding potential bias in the fitting towards a specific structural motif. Given the inherent maximisation of structural randomness when using the RMCProfile fitting technique, it may consequently be assumed that the final configurational results of these experiments are the *least ordered* structures that are *best represented* by the data, and a degree of confidence can be taken from the order being 'built in' via fitting. The large-boxes themselves are comprised of 20 × 20 × 20 unit cells, containing 32,000 atoms; an initial Gaussian profile of small off-site displacements is added to the structure, to aid translational fitting. In all cases, an initial 'grey' run was performed for 2 million moves (with an atom swap or translation constituting a single move) to establish a reasonable distribution of off-site displacements that matched the PDF profile. Full-colour fitting - i.e. the reintroduction of chemical species - was then allowed to proceed from this position using a minimum of 8 million moves, to ensure the convergence of the χ^2 to a global minimum. When introducing chemical variation, a swap probability of 0.2 per chemical species was employed, thereby setting a translation to swap ratio of 2:3.

An initial fitting routine was performed over a 10Å r-range using the end-member 4.2 K dataset, in order to isolate the impact of the scaling parameter from that of the resolution correction, which has its greatest effect at higher values of r. By fitting over a smaller region, an appropriate scale value can be determined without the need for an accurate value of resolution correction, and can

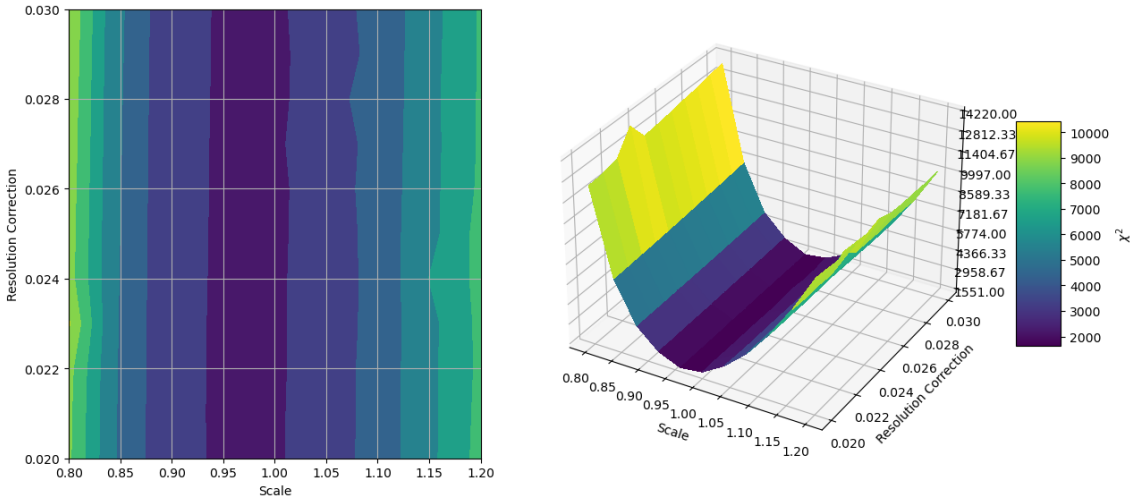

Figure 3.11: A χ^2 plot for the CrCoNi system produced by RMC fitting out to 10Å using a range of scale (0.80-1.20) and resolution correction (0.020-0.030) parameters. Due to the low r-range for fitting, the resolution correction parameter has a minimal effect on fitting, leading to the strongly parabolic trend in scale.

then be used to reduce the size of the parameter space for subsequent fitting regimes. Scale values were selected for fitting over a range of 0.80-1.2 about the 'ideal' scaling value of 1.0, and Resolution correction values were selected over a range of 0.02-0.03, both informed by prior PDFGui fitting. The final χ^2 goodness-of-fit values are presented in Figure 3.11 for each pair of scale and resolution correction parameters in the set. As is evident from the strongly parabolic plot of χ^2 values, the fitting for this particular routine converged on a clear χ^2 minimum when using a scale value of 0.96. The parabolic nature of the data in this r-region also demonstrates the insensitivity of the fit to the resolution correction parameter.

The fitting range was then expanded to 40 Å for the same 4.2 K dataset, over a similar scale range (0.92-1.02), to assess the impact of the inclusion of resolution correction on the quality of fitting. As demonstrated by Figure 3.12, the χ^2 minimum approximately coincides with the prior result - i.e. a best-fit value of the scaling parameter is found in the region of 0.94-0.96. Fitting over a wider r-range, however - thereby increasing the role of the high-r corrective resolution correction parameter - is shown to have a negative impact on the quality of fitting. The overall change in χ^2 across paired values of the scale and resolution correction is shown to be erratic

Given that the extension of the fitting range introduces a greater level of uncertainty in the fitting parameters for negligible improvements to the 'best' χ^2 value, the final r-range used in the fitting of the data was restricted to 15Å. Within this range, any preferential ordering of the local atomic

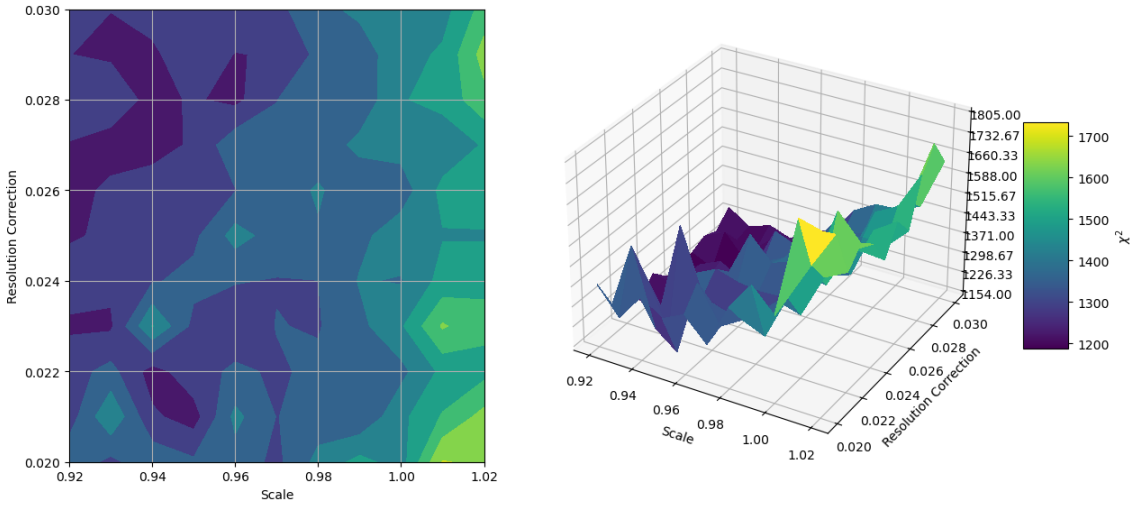

Figure 3.12: A χ^2 plot for the CrCoNi system produced by RMC fitting out to 40Å using a range of scale (0.80-1.20) and resolution correction (0.020-0.030) parameters. Due to the low r-range for fitting, the resolution correction parameter has a minimal effect on fitting, leading to the strongly parabolic trend in scale.

region should be captured out to a suitable number of coordination shells per atom, without compromising the overall quality of the fit; 15Å also represented an approximate minimum between peaks, thereby reducing the information lost when truncating data. The results of this χ^2 fitting for the 4.2 K system are presented in Figure 3.13.

An example of the large-box produced by RMC fitting for the 4.2 K system is presented in Figure 3.14 with a collapsed graphical demonstration of offsite displacements for the system; its associated PDF is available in Figure 3.15. There is little to be drawn from the PDFs in isolation in this instance: across temperature datasets, the difference plots for the best-fit RMC simulations are essentially featureless, and there is limited visual evidence in the partial functions of ordering transitions induced by heating. Analysis of the off-site displacements show an approximately Gaussian distribution of atoms about their lattice sites, further supporting the success of the overall fit for all datasets.

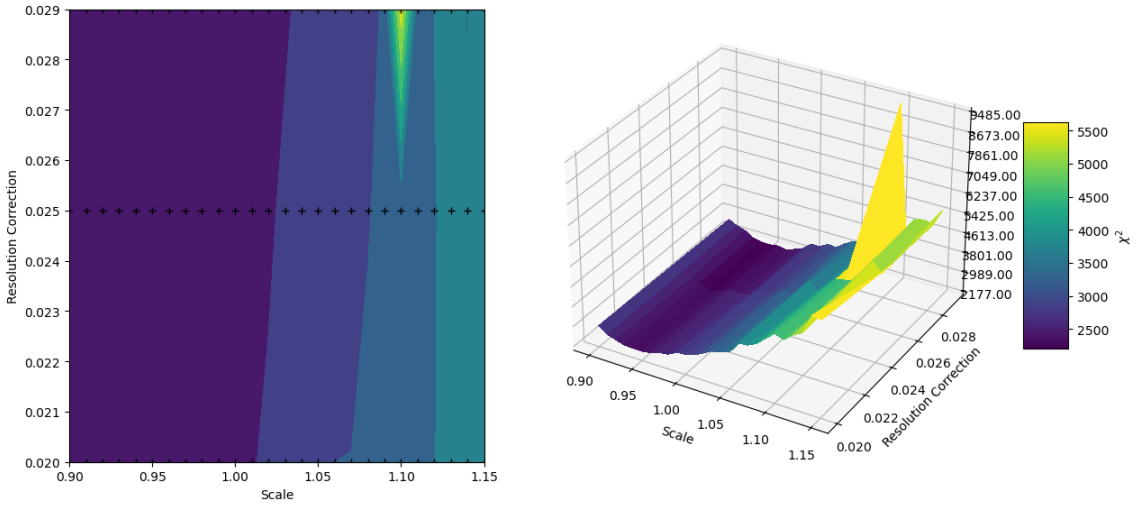

Figure 3.13: A χ^2 plot for the CrCoNi system produced by RMC fitting out to 15Å using a range of scale (0.80-1.20) and resolution correction (0.020-0.030) parameters. Due to the low r-range for fitting, the resolution correction parameter has a minimal effect on fitting, leading to the strongly parabolic trend in scale. Note: The spike in χ^2 value observed at a scale value of approximately 1.10 is an anomalous result, assumed to be caused by a false minimum result when fitting.

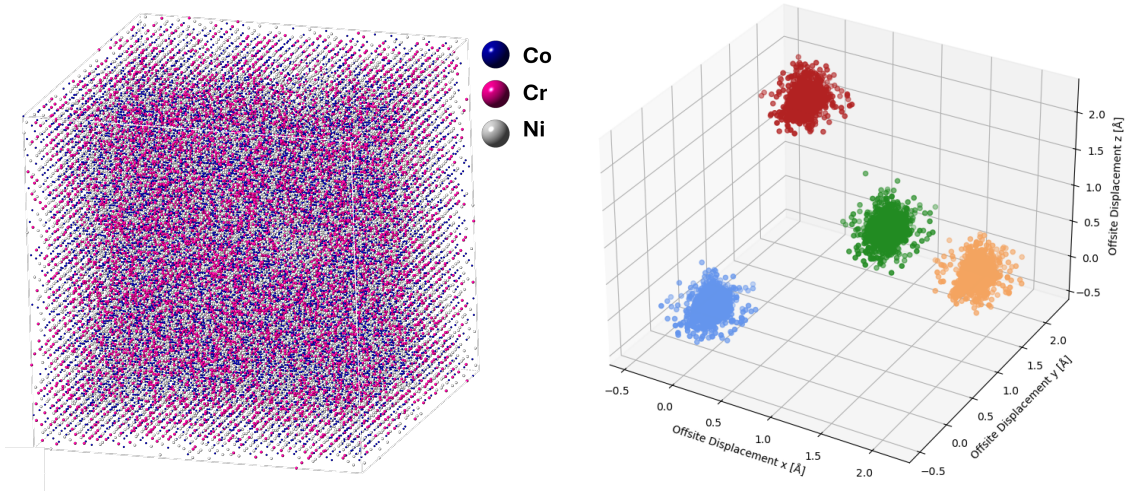

Figure 3.14: Left: The large-box model for the CrCoNi system at 4.2 K as simulated by RMCProfile (scale = 0.92, resolution correction = 0.029); Right: The offsite displacement for this model - atoms are collapsed back on to a single ideal unit cell position, and demonstrate an approximately Gaussian distribution.

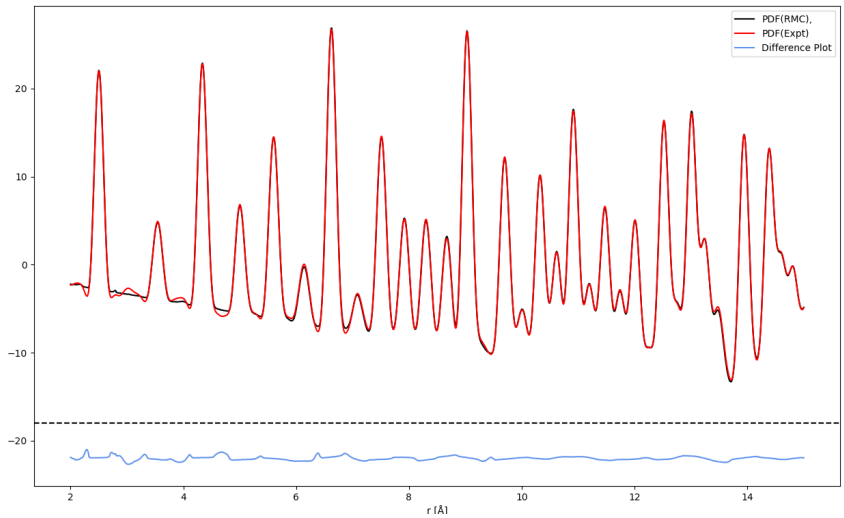

Figure 3.15: The RMCProfile calculated PDF for the CrCoNi system at 4.2 K, using a full-colour fitting regime over 15Å. Note the improvement of the difference plot to prior fitting, demonstrating a superior solution to grey fitting over 40Å.

3.4.3 Clapp Configurational Analysis

Given the prior success of fitting over 15Å, a final series of RMCProfile runs were performed for each temperature dataset. Large-boxes of 32,000 atoms (20 × 20 × 20 FCC unit cells) were once again generated with an initially random distribution of constituent atomic species. RMC fitting was then performed for each temperature dataset using a single best-fit pair of scale and resolution correction parameters taken from prior χ^2 fitting; this fitting was then repeated over 40 simulations, to determine the reproducibility of configurational results. For every box, the Clapp configuration enhancement factors, β, were calculated according to the expression:

$$\beta_a = \frac{n_a - \bar{n_a}}{\sigma_{n_a}} \tag{3.1}$$

where n_a is the number of instances of configuration a;$\bar{n_a}$ is the expected number of instances of that configuration; and σ_{n_a} is the standard deviation. A mean average of the enhancement factors per configuration and associated standard deviation values were then collected across all datasets. Averaging across multiple fitting regimes was performed to reduce the impact of potential false-minima, and provide greater confidence in the final ordering result.

As previously described in Section 1.5.2, Clapp configurations were initially formulated by Clapp for

use in the analysis of binary cubic structures. Extrapolating this system for use with higher-order systems - e.g. ternaries, as in the case of the CrCoNi system - requires the analysis to be performed on pseudo-binary sub-groupings of the overall structure. In the case of a ternary structure, this is somewhat trivial: three pseudo-binaries exist, such that we can divide CrCoNi into Cr:Ψ, Co:Ψ, and Ni:Ψ structures (where Ψ refers to the grouping of remaining constituent elements) for analysis. In this fashion, we can build up a picture of ordering through the recombination of the most enhanced configurations for each element.

The final mean-averaged Clapp enhancement factors are presented for the 4.2K system in Figure 3.16. Taking the Ni:Ψ pseudo-binary initially, we can see that all configurations (labelled along the x-axis) are enhanced to within three standard deviations of the mean to within error, as indicated by the dashed horizontal lines. This indicates that the Ni atoms in the system are, on average, randomly distributed - they demonstrate no preferential ordering behaviours. Cr:Ψ and Co:Ψ, however, show a strong, distinct patterning of enhanced configurations that extend beyond the statistical 'randomness' line. Upon first examination, it is possible to extract several key configurational motifs that are the *most* enhanced across fitting regimes: in this instance, we see strong enhancements to the C7, C16, C34, and C58 or C59 configurations for both the Cr:Ψ and Co:Ψ pseudo-binaries, though this list is not exhaustive.

Taken collectively, these configurations constitute a 'family' of associated motifs that appear to converge upon the more commonly known $L1_2$ structure. The $L1_2$ structure, in Clapp notation, is represented by the C16 configuration (Fig. 3.17), with four dislike nearest-neighbour atoms corresponding to the corners of the unit cell about the atom at the origin. In a binary $L1_2$ long-range ordered structure, only the C16 and C-1 motifs would be statistically enhanced. In a non-long-range ordered structure with a greater degree of statistical randomness in the distribution of constituent elements, however, we would expect to see a greater number of similar or associated structures enhanced along with the C16 configuration itself. The enhanced C7 configuration, for instance, possesses three dislike nearest neighbour atoms in equivalent positions to the atoms in the C16 configuration; the C34 possesses five (Fig. 3.18). At first glance, the enhancement 'pattern' demonstrated by the CrCoNi dataset therefore likely indicates a convergence towards the C16 $L1_2$ structure for both the Cr and Co atoms in the matrix.

A picture of the overall CrCoNi structure at low temperature is therefore constructed: Cr and Co atoms preferentially distribute themselves into the square arrangement demonstrated by the C16 configuration, which - when reframed - represent the corners of the long-range ordered FCC unit cell (i.e. the position with unit cell coordinates (0,0,0)); with Cr or Co atoms in this square arrangement, Ni atoms disperse themselves to the unit cell 'faces' accordingly (i.e. unit cell coordinates (0,0.5,0.5), (0.5,0,0.5), and (0.5,0.5,0)). Beyond this first examination of the enhanced configurations, however, it is worth assessing the distribution of these configurations spatially, and their relationship to any

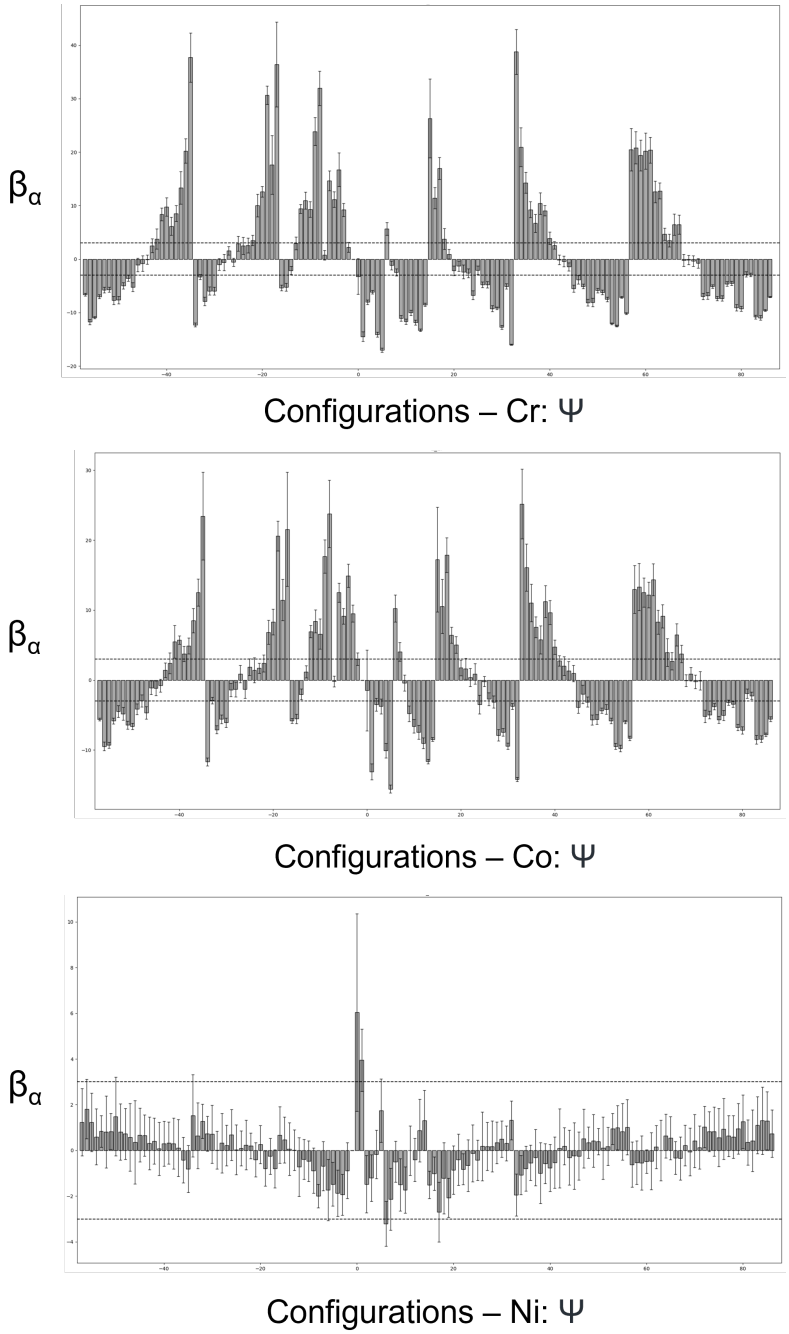

Figure 3.16: Histograms of enhancement factors, β, for the CrCoNi system at 4.2 K.

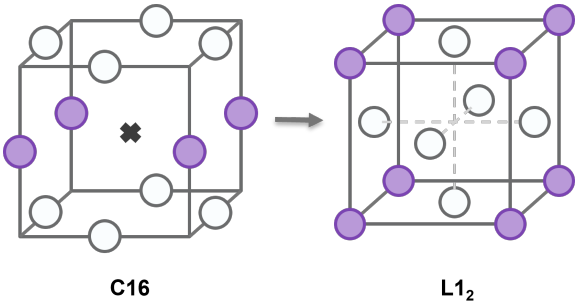

Figure 3.17: The C16 Clapp configuration, and its relation to the $L1_2$ long-range ordered structure.

other enhanced configurations found during statistical analysis. Figure 3.19 shows the location of individual atoms in the large-box that correspond to the origin atoms in the enhanced C16 family of configurations for the Cr and Co pseudo-binaries. There is no identifiable association between the enhancement of the configurations and their spatial distribution: no larger structures occur as a result of this preferential ordering. Importantly, this tells us that the formation of Cr-rich C16 configurations is generally distinct from the formation of Co-rich C16 configurations - both $L1_2$ structures exist simultaneously and separately from one another.

A more thorough analysis of the 'profile' of enhanced configurations at this temperature also provides key structural information. The association of these configurations is mapped most clearly in a configurational 'degradation tree' (Fig. 3.20), wherein the most strongly enhanced configurations are also shown to be linked to one another compositionally. Equally, the enhanced configurations demonstrated in Figure 3.16 are not restricted to the C16 'family' of motifs, but instead show a 'sawtooth' patterning along the x-axis. According to the ordering conventions established by Clapp,

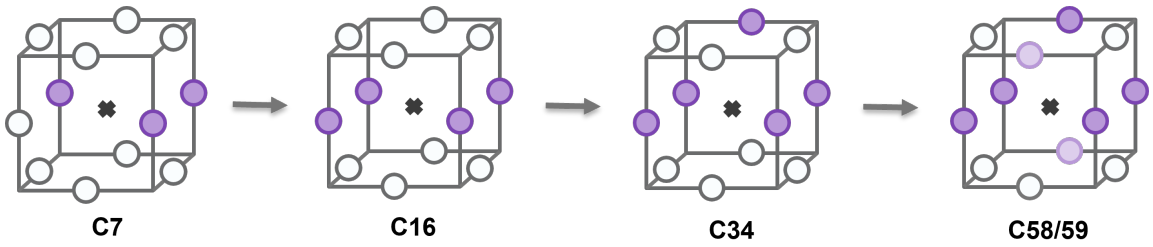

Figure 3.18: The C16 Clapp configuration, and its relation to the C7, C34 and C58-59 configurations. Here, the coloured (purple) positions represent dislike atomic occupations, while white positions represent like atomic positions. Enhancements to these configurations follow a progression of chemical occupation that can be mapped in a 'degradation tree'.

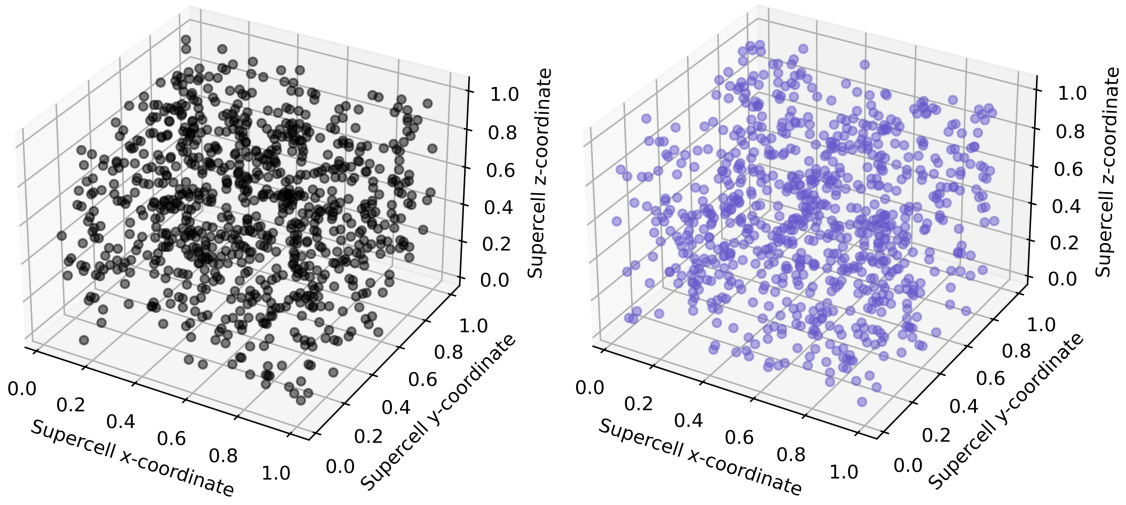

((a)) Cr atoms.

((b)) Co atoms.

Figure 3.19: Mapped Distributions of atoms associated with enhanced $L1_2$ configurations. The lack of clustering or overlap suggests that Cr and Co atoms distribute distinctly from one another.

many adjacent configurations (i.e. those found numerically next to one another in the labelling system) share their total number of dislike nearest-neighbours with one another. These configurations then differ by the absolute positions of these dislike nearest-neighbours; typically, label value will increase with the distance of the dislike nearest neighbours from the origin atom, or by coordination shell. Thus, the alternating sawtooth pattern of the CrCoNi result here may actually provide yet more insight into the structure: the strong enhancement of adjacent configurations suggests that the ordering for this system is primarily driven by nearest-neighbour interactions in the first coordination shell.

This is a pattern repeated across the temperature datasets: at all temperatures, the Ni atoms in the system display no strong configurational enhancements, indicating no preferential ordering behaviours. The Cr:Ψ and Co:Ψ pseudo-binaries show strong enhancements in the C16 'family' of related configurations, and an approximate 'sawtooth' profile indicating a primary preference for ordering in the first coordination shell.

Importantly, there does not appear to be an ordering transition identified across the temperature range used in this study. Comparisons between all datasets at temperatures greater than 4.2K show little variation; enhancements to the major family of associated configurations are, within error, approximately constant. The most significant variation across histograms is the increased prominence of the 'sawtooth' profile between 4.2 K and 64 K. Enhancement to configurations adjacent to the major C16 family of associated motifs is greater at 4.2 K than at any other temperature,

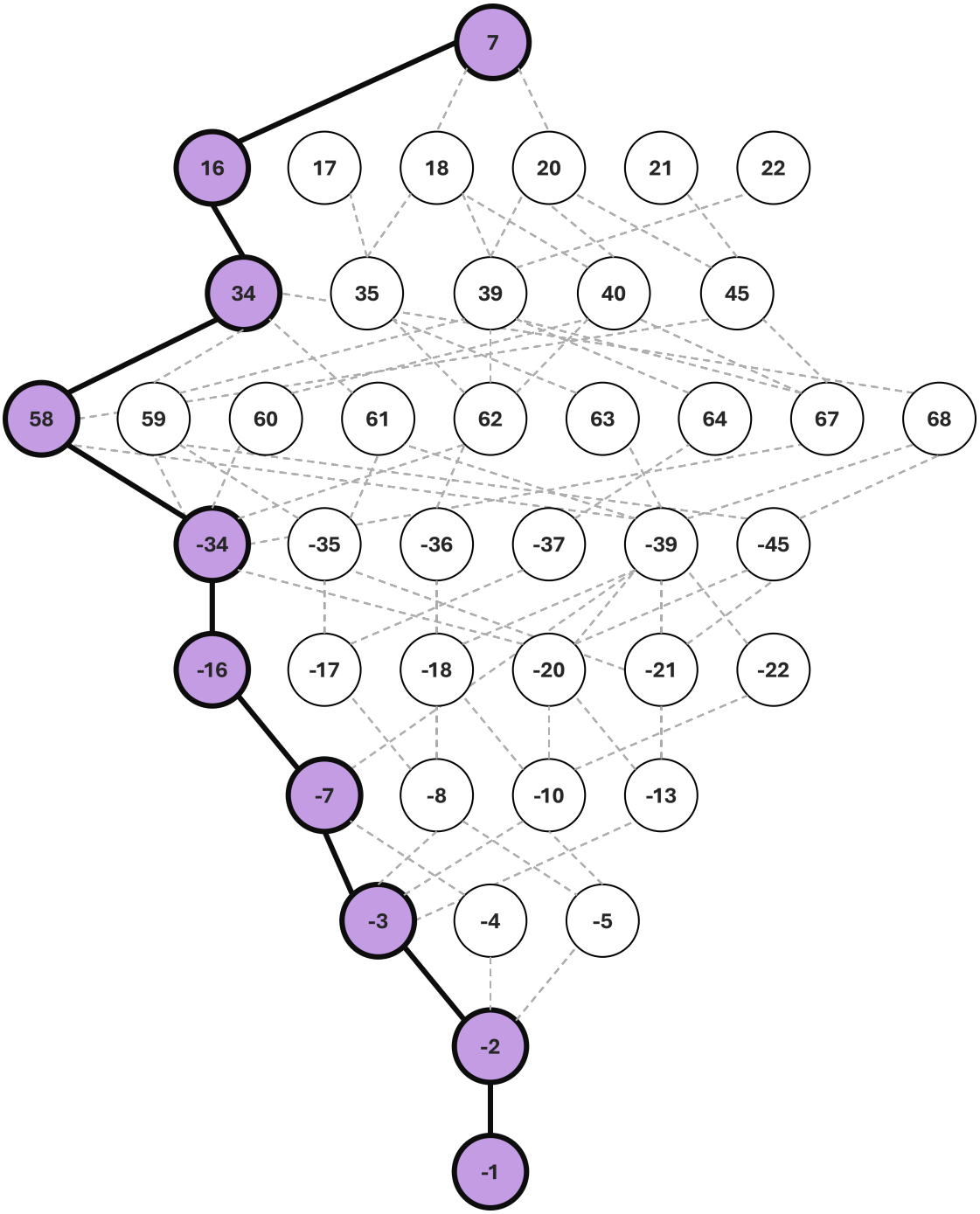

Figure 3.20: A degradation tree of enhanced configurations for the CrCoNi system, demonstrating the compositional links between major enhanced configurations and the $L1_2$ structure. Each row contains configurations with equal numbers of dislike nearest neighbour atoms.

potentially indicating some form of ordering behaviour at very low temperatures as atoms lose their preferential ordering beyond the first coordination shell. The exact origin of this behaviour is as-yet unidentified: this could, for instance, be caused by a magnetic transition at very low temperatures (which typically impacts atoms in the first coordination shell more significantly than those around it). It is also possible that at low temperatures - where the thermal contributions to atomic positions are reduced and therefore there is less overlap between higher order peaks - the RMCProfile algorithm is more readily capable of resolving the ordering in individual coordination shells. In either case, it is likely that further work would be required to ascertain the causes of this particular behaviour - though the effect is not strong, and should not detract from the major $L1_2$ structure demonstrated above.

3.4.4 Further Modelling

RMC fitting - translations and swaps (Pastel Run)

Given that this technique has not yet been applied to metallic materials of greater than two constituent components, it is important to interrogate the efficacy and robustness of the method. The additional complexity of a single added constituent atomic species is relatively easily noted: the number of possible nearest neighbour configurations for a binary FCC alloy is 2^{12} (4096); in a ternary system, that number rises to 3^{12} (531,441). As the method enters even wider compositional spaces, this number increases exponentially. The ability of the RMC method to resolve this compositional complexity, and for the Clapp-style pseudo-binary reduction to adequately or intuitively capture said ordering, remains an open question of some difficulty.

Where prior binary investigations had required only two forms of RMC fitting, a ternary material provides the opportunity for further RMC analysis. The following section, therefore, outlines the use of 'pastel' fitting: the deliberate restriction of atom types during fitting to assess the validity of pseudo-binary analysis. In each case, the atom types used in fitting correspond to one of the pseudo-binaries previously employed during Clapp configurational analysis. Take the Cr:Ψ pseudo-binary as an example. It is possible to fit a large-box using all three atom types in the input model, then combine the Ni and Co atoms into a single, arbitrary atom type 'Ψ' during Clapp configuration analysis, creating a pseudo-binary as described previously. It is therefore also possible to combine the Ni and Co atoms into atom type 'Ψ' in the input model itself - with associated averaged neutron coefficients for the combined atom type - fitting the PDF using the pseudo-binary structure. This strategy allows for analysis of the extent to which the final configurational results are impacted by the addition of chemical complexity during the fitting process.

The results of 'pastel' fitting are presented in Figure 3.21 for the 4.2 K end-member dataset, which should possess the greatest level of local atomic ordering. Co:Ψ pseudo-binary fitting shows strong

agreement with prior 'colour' fitting, with large statistical enhancements to the C16 - $L1_2$ family of atomic configurations. Once again, the sawtooth profile of enhancements likely indicates preferential Co ordering within the first coordination shell. The enhancements to these configurations are also slightly larger when fitting using the pseudo-binary; the value of the enhancement factor, β, increases from 17.23 to 59.35 for the C16 configuration. This increases the overall confidence in the success of the RMC method in reproducing the correct ordering for the Co system, as the introduction of additional 'degrees of freedom' has no overall bearing on the qualitative description of ordering.

Enhanced configurations in the Cr:Ψ pseudo-binary, however, differ somewhat from the initial three-atom fitting. Interestingly, enhancement to the C16 configuration in particular is much stronger when using the pseudo-binary as a fitting input. During full-colour fitting, the mean-averaged value of β for the C16 configuration is found to be 26.29; during the 'pastel' pseudo-binary fitting, this value increases to 101.93. This large increase in the enhancement of certain configurations is mirrored in the associated C7 (5.65 to 45.95) and C34 (38.75 to 54.06) configurations, suggesting that the $L1_2$ structure (and associated motifs) are significantly more common in the final large-box. Notably, however, configurations at the 'extreme ends' of the Clapp labelling scale are no longer enhanced at all. In particular, the C-16 configuration is substantially less enhanced (36.39 to 11.68) and the C-34 configuration seemingly vanishes entirely. This suggests that the Cr pseudo-binary more strongly favours the $L1_2$ structure - whereby Cr atoms sit on the corners of the unit cell - in the absence of additional chemical complexity.

The Ni:Ψ pseudo-binary is perhaps the most interesting result of the three pastel fitting regimes. Earlier 'colour' fitting had shown that the Ni atoms randomly distribute themselves across the CrCoNi lattice, with limited evidence of preferential ordering behaviours. When fitting as a Ni:Ψ pseudo-binary, however, this result is entirely upended. Instead, the Ni atoms appear to form the C16 $L1_2$ configuration themselves, in an equivalent sawtooth profile to the Cr: and Co:Ψ pseudo-binaries. At a glance, this is non-ideal: a result such as this could raise concerns that RMCProfile is converging to a single solution (i.e. the $L1_2$ structure) within a 'false minimum', rendering prior results unphysical. However, a closer analysis of the calculated neutron coefficients for this experiment could explain the discrepancy in fitting. Ni has a neutron scattering length of 10.3; Co, a scattering length of 2.49; Cr, 3.635. Calculation of a neutron coefficient weighted by total concentration is necessary for the fitting of neutron data, and (unless otherwise prompted) RMCProfile performs this calculation by default. When fitting with pseudo-binaries, however, these weighted neutron coefficients naturally require adjustment, or averaging, for the combined atomic species. In the case of the Cr:Ψ and Co:Ψ pseudo-binaries, this involves the averaging of a large neutron scattering length - that of the Ni atoms - with a relatively small scattering length for the remaining atomic species, leaving two atom types with relatively similar neutron coefficients for fitting. For the Ni:Ψ pseudo-binary, however, the smaller scattering lengths of Cr and Co are

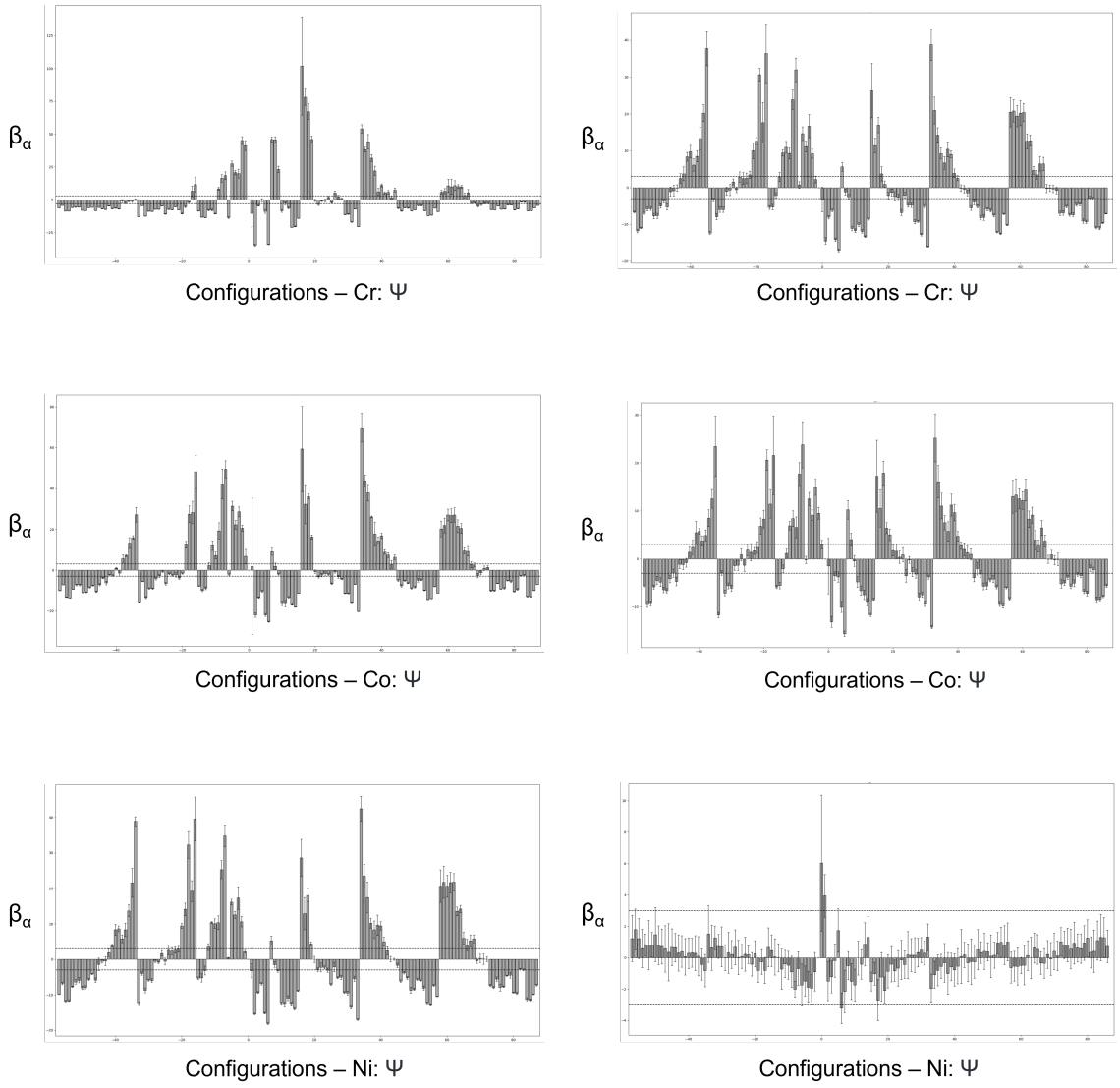

((a)) Pastel Pseudo-binaries.

((b)) Full-colour Pseudo-binaries

Figure 3.21: Histograms of enhancement factors, β, for the CrCoNi system at 4.2 K, providing a comparison between 'pastel' binary fitting (Left) and the original multi-atom 'colour' fitting (Right).

averaged, meaning that the fit is performed using two atomic 'species' with markedly different neutron coefficients. The final results, therefore, indicate that the Ni:Ψ pseudo-binary fitting is dominated by the effects of the Cr-Co atoms; the weighting associated with the small neutron coefficient has ultimately superseded that of the Ni atoms, providing an overall $L1_2$ structure in the final fit.

Ultimately, these results are encouraging. Broadly speaking, there is a strong agreement with the 'full colour' ternary fitting performed prior to pastel running, with all fits demonstrating an equivalent $L1_2$-family of enhanced configurations. Given the reduction in computational complexity inherent to 'pastel' fitting, and the success of previous studies in the analysis of binary systems, we can infer the success of the fitting regime from the overall consensus between fit types. The stronger enhancement of the C16 configuration for the Cr atoms in the system also continues to point towards agreement with existing CSRO studies on the CrCoNi system, which have previously identified the migration of Cr atoms to the corners of the unit cell. It particularly agrees with the aforementioned studies by Zhou *et al.* [61] and Zhang *et al.* [64], which identified the overall chemical segregation of Cr atoms in their respective studies.

The Impact of Neutron Coefficients on Fitting

Given the above results, it is not unreasonable to question the validity of the results provided by RMCProfile, particularly when considering the role that neutron coefficients play in the fitting process. This is not unique to the 'pastel' fitting described above; in all cases - and indeed in all modelling from neutron data - there arises a question regarding the disparity of neutron coefficients and the ability of the technique to distinguish between atom types. It is possible to imagine a scenario in which the constituent atoms of a system are indistinguishable from one another by neutron scattering length, such that it was impossible to determine the absolute local structure of the material using simply neutron scattering diffraction, or that many possible solutions to this fitting would be considered equally likely. To this end, determining the impact of neutron coefficient variation on the resultant configurational analysis is integral to the success of the method with increasing chemical complexity.

To assess the efficacy of RMC method in reproducing the ordering of a given alloy, a large-box was constructed with *known* local structure. The PDF for this structure was subsequently calculated, and used as the input dataset for an RMC fitting using an initially *random* structure of equivalent composition. In the ideal case, the random box would be expected to take on the approximate local structure of the initially ordered box, demonstrating any potential discrepancies introduced to the system by fitting. The purpose of this particular investigation is twofold: in the first instance, the ability of RMCProfile to generate structures accurately for a known solution is assessed; in the second - following failure or success - it can then be used to assess the impact of neutron coefficients

on the physical accuracy of the produced model. It is worth noting, prior to analysis, that the extent to which this method is applicable to the discovery of SRO will be system dependent: if the type and extent of ordering is not sufficiently captured for a given sample then the investigation will not succeed. The failure of this method for CrCoNi, therefore, would not represent the total failure of the method - simply that it is not an appropriate method for this material.

For the purposes of this analysis, large-boxes of the FCC CrCoNi alloy were constructed by Killian Sheriff of the Massachusetts Institute of Technology (MA, USA), using machine learning potentials to generate a known input structure. Ten boxes of 10×10×10 FCC unit cells (4000 atoms) were generated equivalently for two compositional cases, one with an equiatomic composition (0.333 Cr - 0.333 Co - 0.333 Ni) and the other with a non-equiatomic composition (0.25 Cr - 0.375 Co - 0.375 Ni). Thermal noise was simulated in the system using a distribution of off-site displacements generated using MD simulation. RMCProfile itself was used to calculate the PDF for each box, to be used as input for later fitting, ensuring overall consistency in the fitting process. Clapp configurational analyses were then performed on the boxes to ascertain the initial structure of the system, with the enhancement factors (β) mean averaged as with prior running with experimental data. The results of this configurational analysis may be found in Figures 3.22 and 3.23. As is immediately apparent - both boxes have strong, well-defined ordering enhancements, but with significant errors through. Ignoring errors for a moment: in the case of the equiatomic box, the Cr atoms appear to approximately randomly distribute themselves; the most enhanced configurations in this instance are the C1 and C2 structures, indicating a preferential local bonding with predominantly like atoms. Taking the large error in account, however - overlapping with the three standard deviation 'randomness' line - we find a wide variation between boxes. Interestingly, the Ni atoms for this system appear to approach the $L1_2$ structure, with strongest enhancements to the C16 family of configurations. The error for these enhanced configurations is, however, reasonably large, indicating a large variation in the enhancements of the structure between simulations. A more conservative interpretation of these results would therefore suggest a likelier random distribution of Ni atoms overall.

The Co atoms in the equiatomic model demonstrate a much clearer ordering behaviour, with particular enhancement to the C17 and C38 configurations. In the case of the C38 configuration (β = 116.5) the extremely large standard deviation (σ = 116.0) could suggest a randomness in its enhancement. The C17 structure ($\beta = 83.5$), however, is of greater interest. The C17 configuration is associated with the $D0_{22}$ structure, requiring co-enhancement to the C16 and C-1 configurations. This can be seen in the equiatomic CrCoNi box ($\beta_{C16} = 33.1$, $\beta_{C-1} = 22.3$), suggesting a preference in the system towards the $D0_{22}$ structure. Its presence is not entirely surprising - the $D0_{22}$ structure has been identified as a precursor to the $L1_2$ structure previously shown to be present in the CrCoNi system. Taking the form of a tetragonally symmetric, non-cubic motif (Fig. 3.24), it

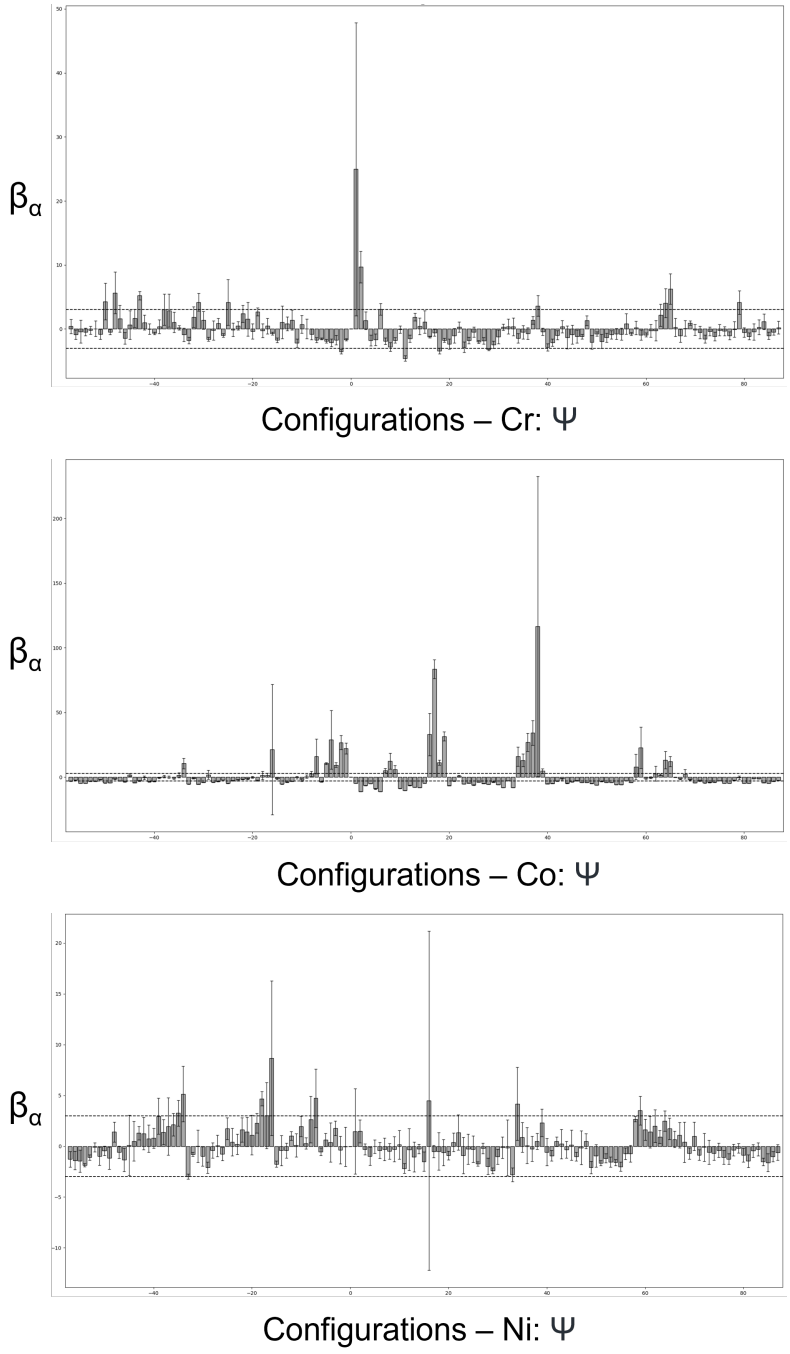

Figure 3.22: Histograms of averaged enhancement factors, β, for the equiatomic CrCoNi system at 300 K as generated by ML potentials.

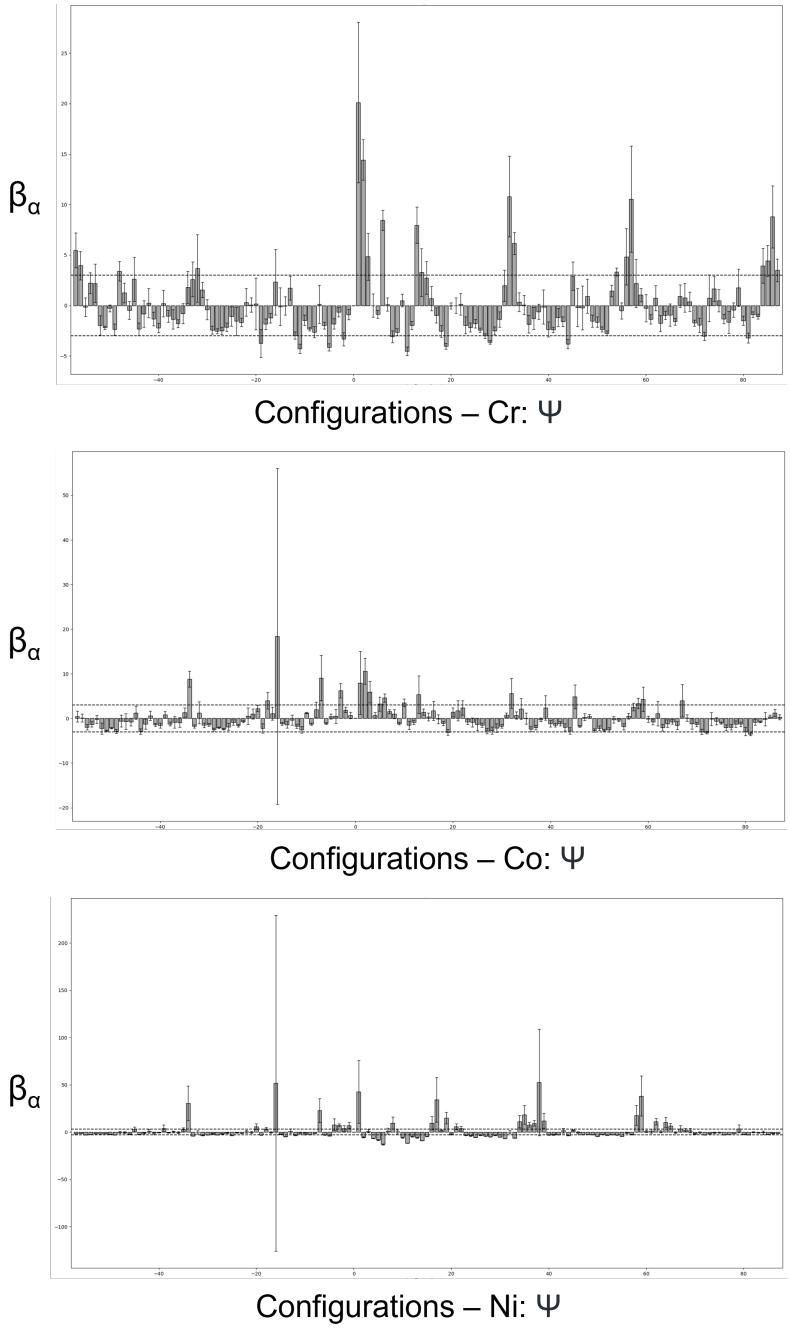

Figure 3.23: Histograms of averaged enhancement factors, β, for the non-equiatomic CrCoNi system at 300 K as generated by ML potentials.

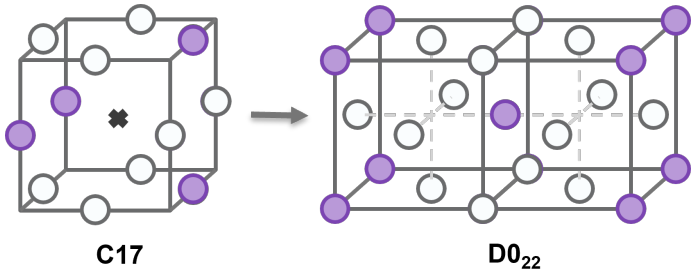

Figure 3.24: The C17 Clapp configuration and its associated $D0_{22}$ long-range ordered structure.

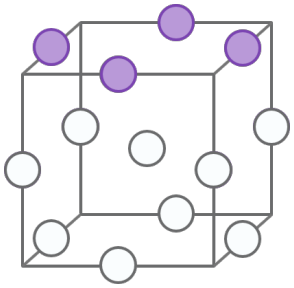

Figure 3.25: The C32 configuration.

is a form of local ordering commonly found in intermetallic compounds.

The non-equiatomic box does not share the ordering of its equiatomic partner, though it still possesses a good degree of ordering. The Co:Ψ pseudo-binary in this instance is not strongly ordered, with relatively small enhancements shown to the (predominantly unrelated) C2, C-3 and C-7 configurations. In the Ni:Ψ pseudo-binary there is arguably limited evidence for the presence of the $D0_{22}$ structure - with enhancement to the C17 configuration ($\beta_{C17} = 34.3$) and minor enhancements to the C16 and C-1 motifs - though this is not well established. The configurations with the largest enhancements (C-16, $\beta_{C-16} = 51.8$ and C38, β_{C38} 52.6) are also essentially randomly distributed within error, showing no strong preference for any particular structure. Cr atoms, however, appear to have a more well-defined ordering behaviour, with relatively large enhancements to the C1 ($\beta_{C1} = 20.1$), C6 ($\beta_{C6} = 8.45$), C13 ($\beta_{C13} = 7.96$), and C32 ($\beta_{C32} = 10.98$) configurations. This particular 'family' of associated configurations - constituting a preferential bonding for dislike atoms along alternating faces of the unit cell - could be associated with the AB B11 structure. In a long-range ordered system, this would simply be represented by the C32 configuration (Figure 3.25).

An RMCProfile fitting was then performed for each set of boxes, using a PDF generated from one of the ten boxes produced for each composition. As described previously, a G(r) PDF was calculated by the RMCProfile software itself to 15Å- an r-range selected to match earlier fitting

from experimental data - and used as an input dataset for fitting. In the first instance, neutron coefficients were not specified as input, and the RMCProfile software allowed to generate them internally. As with prior running, all simulations were allowed to converge upon a χ^2-minimum prior to analysis. The results for the equiatomic case are presented in Figure 3.26, and the non-equiatomic case in Figure 3.27. It is readily apparent in all pseudo-binaries that RMCProfile has failed to reproduce or capture the input ordering of the boxes. In the case of the equiatomic box, the fitting process has produced an entirely random structure; none of the pseudo-binary histograms show strong enhancement, outside of error, to any one configuration of atoms. This is equally true of the Ni:Ψ and Cr:Ψ pseudo-binaries in the non-equiatomic case, which also demonstrate approximately random distributions of constituent atoms. Interestingly, the Co:Ψ pseudo-binary appears to have replicated *some* of the ordering present in the initial box. Enhancements to the C2, C6, C13, and C32 configurations are in line with expected local ordering, though they are particularly small ($\beta_{C2} = 10.6$ being the largest of the four). This similarity ends, however, with configurations containing lower concentrations of dislike atoms - for the most part, the programme has failed to reproduce the ordering applied to both boxes. It is also apparent that these results differ significantly from those produced by RMCProfile fitting to experimental total scattering data, with almost no overlap between the enhancements seen in the non-equiatomic case and the experimentally derived boxes.

It is perhaps unsurprising that - in the absence of a single 'best fit' solution - the programme has produced a series of essentially random boxes. It is also possible that the PDFs produced by the provided boxes - in both the equiatomic and non-equiatomic cases - can be well described with an entirely random distribution of constituent elements, without providing the expected solution. It is possible to imagine a scenario in which the form of the PDF peaks can be well-fitted by both an ordered case and a disordered case, due to the variation in neutron scattering lengths and their impact on partial functions. The small enhancement to ordering present in the non-equiatomic box, however, potentially suggests some role for calculated neutron coefficients in the accuracy of the produced results, given their mathematical relation to atomic concentration. Assessment of the impact of neutron coefficients on the success of fitting could therefore act as a benchmark of sorts for future configurational analyses.

In order to see the effect of scattering length on the quality of fitting, a parameter space was formulated such that the input variables of the RMC fitting regime were the ratios of constituent scattering lengths. More plainly, the scattering length (b_A) of an arbitrary atom of type 'A' was held to be equal to 1; the scattering lengths of arbitrary atoms 'B' and 'C' were then varied relative to atom A, such that their values were some fraction or multiple of A (e.g. $\frac{b_B}{b_A} = 0.5$, $\frac{b_C}{b_A} = 3$). Ratios $\frac{b_B}{b_A}$ and $\frac{b_C}{b_A}$ were varied over a range of -2.5-5.0, pre-selected by taking equivalent ratios for all possible metallic scattering lengths and determining the frequency with which certain values

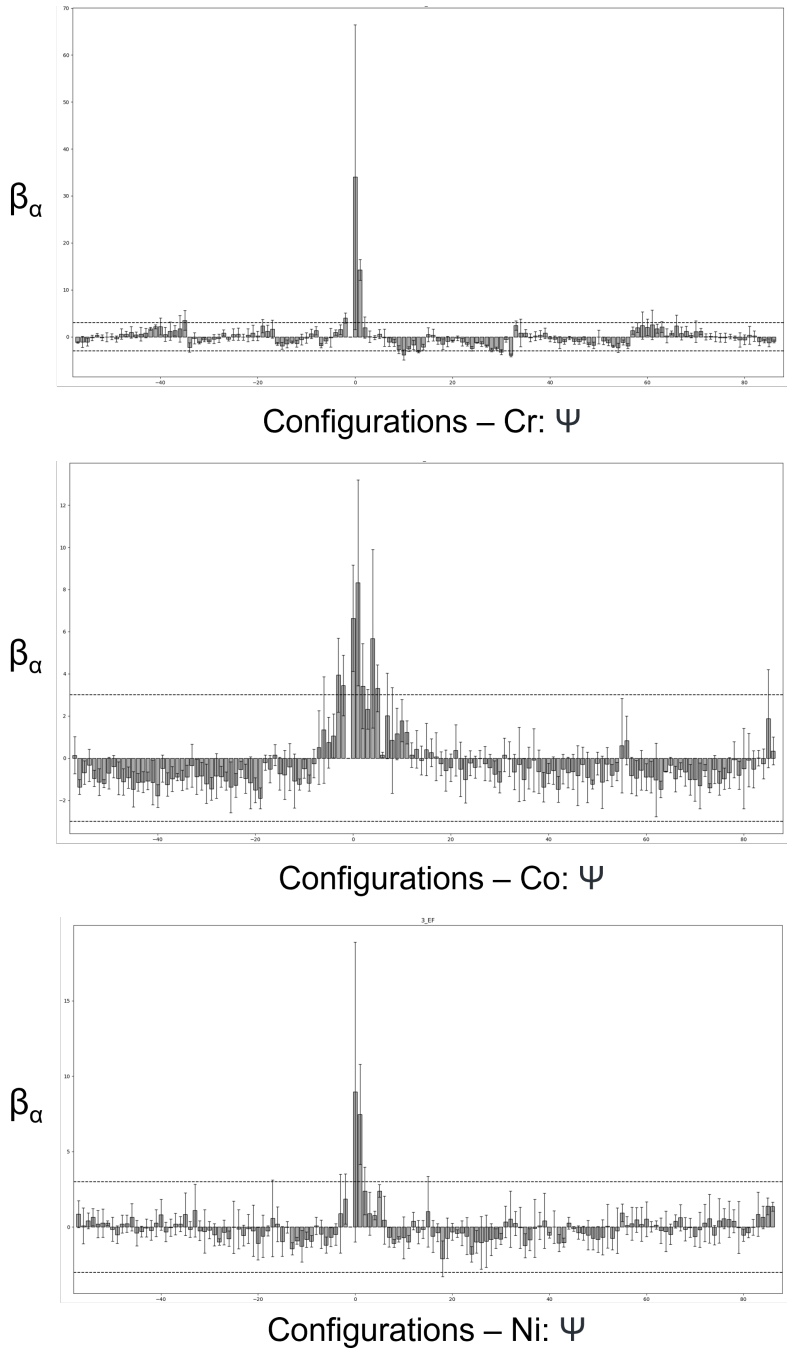

Figure 3.26: Histograms of averaged enhancement factors, β, for the equiatomic CrCoNi system at 300 K as generated by RMCProfile.

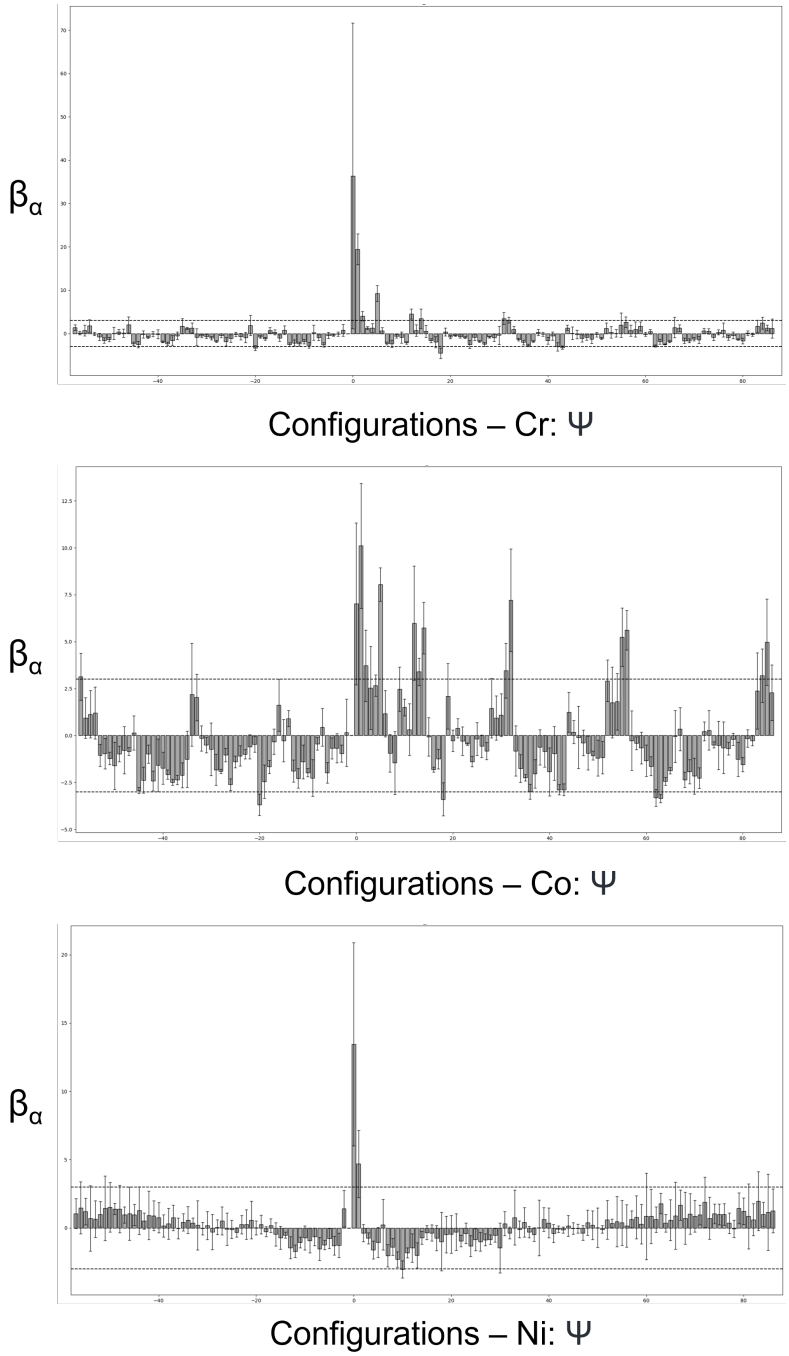

Figure 3.27: Histograms of averaged enhancement factors, β, for the non-equiatomic CrCoNi system at 300 K as generated by RMCProfile.

appeared (Figure 3.28). In all other respects, these runs were identical to prior simulations: the input dataset was generated using one of the ML potential boxes, and simulations were allowed to progress until a χ^2-minimum was achieved. The χ^2 minimum results for this parameter space are presented in Figure 3.29.

The results in this instance show very little by way of trend, or indication that particular ratios of scattering lengths cause the RMC fitting process to behave predictably. The strongest χ^2 fits are almost always produced when the ratio $\frac{b_C}{b_A}$ is approximately equal to 1, potentially suggesting that fitting is performed most accurately for this dataset when only *one* of the constituent neutron coefficients differs significantly from the others.

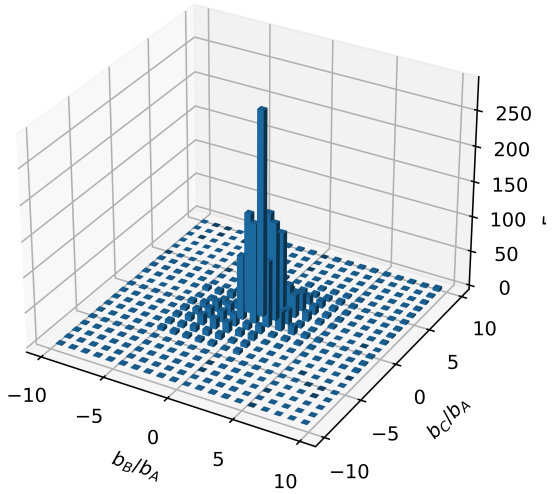

Figure 3.28: A frequency map demonstrating the number of times a given ratio of $\frac{b_B}{b_A}$ to $\frac{b_C}{b_A}$ may occur within the bounds of known neutron scattering lengths for transition metals.

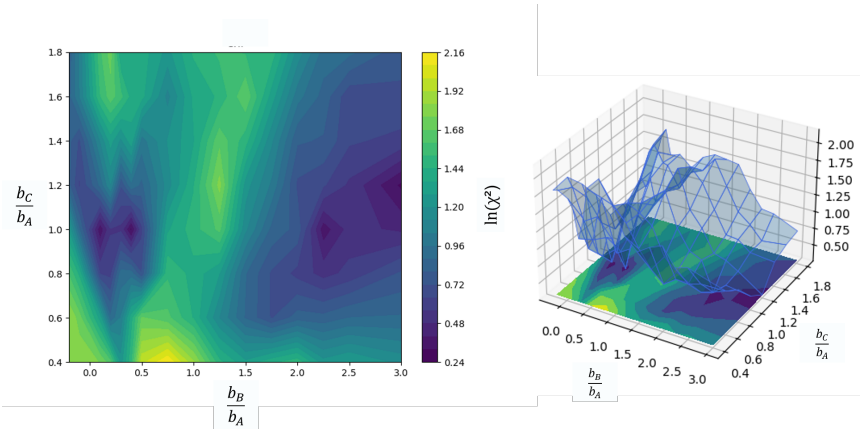

Figure 3.29: The results of χ^2 fitting for the CrCoNi system using all paired values of $\frac{b_B}{b_A}$ and $\frac{b_C}{b_A}$ pair neutron coefficient ratios. No clear pattern emerges from the fitting.

This could explain the success of fitting in the cases of the non-equiatomic boxes: the introduction of a disparity in atomic concentrations would change the neutron coefficients in an equivalent manner. However, this rule does not hold true for the fraction $\frac{b_B}{b_A}$, which - given that the elements used in fitting were essentially arbitrary - weakens this argument significantly.

Warren Cowley Parameters

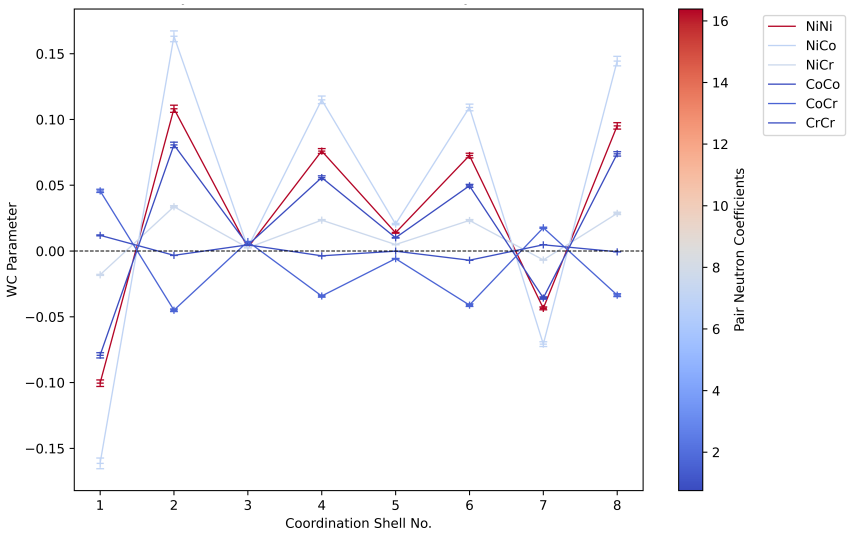

Figure 3.30: Calculated pairwise Warren-Cowley parameters for the CrCoNi system at 4.2 K, demonstrating the oscillatory effect most commonly associated with $L1_2$ structures.

One of the touchstones of short-range order analysis historically has been the use of Warren-Cowley parameters to identify the behaviour of interatomic pairings. For the CrCoNi system, these Warren Cowley parameters are well-established, as previously described in the introductory section. Though the utility of these parameters is questioned in the context of higher-order systems - collapsing a considerable amount of spatial information into a singular numerical value - it is a useful point of comparison to generate these values for the boxes produced by RMCProfile. The following plots therefore contain the calculation of Warren-Cowley α-parameters out to the first 8 coordination shells, calculated using the pair-wise form of the Warren-Cowley equation outlined in Section 1.5.1. In each instance, the colours of the data are placed along a scale demonstrating the size of the neutron coefficients associated with the atomic pairing.

In the first instance, the Warren-Cowley parameters for the 4.2 K dataset are presented in Figure 3.30. In a fully long-range ordered binary $L1_2$ structure, we would expect to see the oscillation of α values across coordination shells for the associated atomic pairings, as seen in Section 1.5.1. In the case of the 4.2 K dataset, we see a degree of oscillation in the majority of atomic pairs out to the 8th coordination shell, though not in the same manner as a perfectly $L1_2$ structure. In the majority of cases, the oscillation between coordination shells is evident; consecutive coordination shells appear to alternate between attraction or repulsion and a random distribution (i.e. $\alpha = 0$). At 300 K, however, this oscillation is not pronounced; there is a clear, 'degrading' oscillation towards

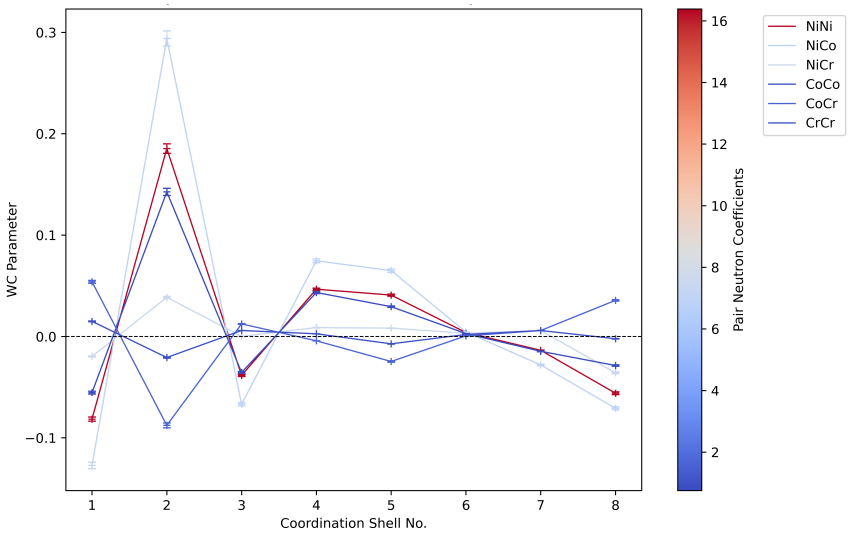

Figure 3.31: Calculated pairwise Warren-Cowley parameters for the CrCoNi system at 300 K; note the 'dampened' oscillatory effect, likely demonstrating strong, short-range ordering effects.

the fourth coordination shell, beyond which the behaviours of the α values appear mostly random. This preference for ordering behaviour to within one or two coordination shells is consistent with the presence of short-range statistical ordering in the $L1_2$ form described previously (Figure 3.31) Beyond this coordination shell, however, the behaviour of all pairings is more random, though there is a small amount of evidence for the preference for preferential bonding in the fifth coordination shell for the Ni-Ni, Ni-Co, and Co-Co pairs, perhaps suggesting interesting ordering behaviours beyond the first few coordination shells. Also worthy of note is the strong ordering enhancement over the first two or three coordination shells specifically for atomic pairs with the largest or lowest neutron coefficients. This lends credence to the suggestion that variation in scattering length impacts the efficacy of RMC fitting, though further work here would be required.

For the most part, this trend does not change with temperature. In the case of the 4.2 K dataset, however, the Warren-Cowley distribution changes somewhat. For all atomic pairings bar the Cr-Co and Cr-Cr pairs, a significant oscillation above zero is present, indicating some form of ordering behaviour. This effect is particularly strong in the transition from the first to the second coordination shell, as one might expect from prior Clapp configurational analyses that identified $L1_2$-type ordering behaviour. Beyond this point, however, the majority of atomic pairings appear to cluster or randomly distribute themselves in an alternating fashion out to the seventh coordination shell. Given that previous findings for the CrCoNi system in this investigation had identified a stronger 'sawtooth'-type $L1_2$ patterning in the enhancement of configurations, lending credence to the presence of an overall preference for dislike bonding to within the first coordination shell, and

less preferential bonding beyond that distance. In this instance, also, there is less evidence for the impact of neutron coefficients on the overall fitting, as the distribution of coefficients over the atomic pairs appears to be itself more random.

3.5 Conclusions

This chapter has demonstrated theordering behaviours of the CrCoNi ternary alloy system as produced by the RMC Total Scattering method, and illustrated the utility of Clapp-configurational analysis in the case of metallic systems containing more than two constituent elements. The use of pseudo-binary Clapp configurational analysis has proven to be a useful simplification in the case of higher-order compositions, though questions remain regarding its suitability for systems containing more than three elements.

Across all temperatures, between 4.2 K and 300 K, the CrCoNi alloy was found to possess an overall preference for $L1_2$-type ordering. Cr and Co atoms were found to preferentially distribute themselves in 'square' arrangements of nearest neighbour atoms, corresponding to the C16 Clapp configuration and thereby the $L1_2$ structure. In doing so, the Co and Cr atoms show simultaneous enhancement to an associated family of atomic configurations - including the C7, C34, and C58-59 configurations - that differ by the presence of only one or two Co or Cr atoms, suggesting a preferred ordering pathway to the long-range ordered $L1_2$ structure. The remaining Ni atoms in the matrix demonstrate an approximately random distribution behaviour, presumably primarily presenting on the 'faces' of the unit cell in the $L1_2$ structure. This aligns neatly with prior investigations into the short-range ordering behaviours of the CrCoNi system: many studies have reported a preference for the formation of $L1_2$-type structures, and indeed TEM studies by Zhou *et al.* have supported a distribution of Cr atoms specifically to the corners of the unit cell. In practice, these results also act to resolve existing conflicts in the literature: a number of modelling studies had identified a strong ordering preference for Ni atoms in the system, in direct opposition to the supposed ordering behaviours of Cr atoms identified by Zhou *et al.* Given that the above results are experimentally derived - bridging the gap between simulation and experimental characterisation - it is possible to definitively assert a greater role for Cr in the ordering of the ternary than for Ni.

Such agreement with existing literature provides confidence in the ability of the RMC method to reproduce the structure of higher-order or chemically complex metallic materials. It is interesting to note that - while there is no clearly identifiable ordering transition present in the analysis performed here - the distribution of Clapp configurations at low temperature could indicate a potential ordering phenomenon between 4.2 K and 64 K, given the increased prevalence of enhancements to configurations adjacent to the 'primary' $L1_2$ structure. This particular ordering behaviour is not enormously well evidenced - there is limited discussion in the literature about such a phenomenon -

but it is possible that cryogenic temperatures bring about some form of magnetic transition due to the presence of magnetic frustration in the Cr or Ni atoms of the system as mentioned by Woodgate *et al.* [68]. This, however, is beyond the scope of the present investigation, and remains an open line of inquiry.

Chapter 4

CrFeCoNi

4.1 Introduction

Applying total scattering diffraction analysis and subsequent Clapp-style configurational analyses to the analysis of ternary systems is demonstrated to be viable and effective. For a given ternary lattice it is possible to create three pseudo-binaries, each corresponding to a constituent atomic species in the system, and thereby uncover the local ordering behaviours of the material. If this method is to become ubiquitous in the analysis of complex higher-order systems, however, this method must be extended to quaternaries, quinaries, and beyond - a process that is significantly less easily accomplished.

The natural successor to a study on ternary alloys is the analysis of a quaternary, to assess the efficacy and scaleability of the method. CrFeCoNi is one such quaternary of interest. As in the prior CrCoNi study, CrFeCoNi is a derivative of the CrMnFeCoNi 'family' of associated MPEAs studied for their interesting mechanical properties and potentially unique local ordering behaviours. As with many of the other MPEAs widely studied in the literature, CrFeCoNi has been highlighted for its exceptional strength-ductility and fracture toughness properties, with a number of studies highlighting its unique resistance to failure by dynamic shear. [70] This marks the CrFeCoNi as another potential alloy of interest within the CrMnFeCoNi 'umbrella' for use in extreme environments and specialist applications.

Much like the CrCoNi ternary alloy, these property enhancements have been routinely linked to the atomic short-range order of the solid solution, though the empirical evidence for this effect is thin. The debate surrounding the form of SRO in the CrFeCoNi quaternary has been a feature of the field for at least a decade. A 2015 investigation by Tamm *et al.* [71] initially identified a

significantly reduced number of Cr-Cr and Fe-Fe atomic pairs - and a concurrent, smaller reduction in the number of Ni-Ni and Co-Co pairs - relative to other A-B type pairings using a Monte Carlo simulation approach. Work by He *et al.* in 2018 [72] identified the presence of local lattice distortions in the CrFeCoNi MPEA using a DFT-analysis approach. Pair Distribution Function data were generated from X-ray diffraction experiments, and supercells produced from these data using a Reverse Monte-Carlo method. The authors then compared the enhancement of specific atomic pairs in their RMC generated box versus a randomly distributed box of atoms, highlighting a random distribution of Cr-Fe, Cr-Ni, Co-Fe, and Fe-Ni atomic pairs. It is therefore inferred that the Cr and Co atoms in the system must demonstrate some level of atomic-scale ordering, though the form of this ordering is not explored.

Similarly in 2015, Niu *et al.* [73] used *ab initio* simulation (VASP) to demonstrate a magnetic frustration effect in random CrFeCoNi solid solutions. This frustration was found to be reduced when Cr atoms segregated to the corners of the FCC unit cell, forming an $L1_2$-type ordering structure; the group suggest that this is primarily driven by antiferromagnetic coupling with the remaining Fe, Co, and Ni atoms in the lattice. This result was further supported by Fukushima *et al.* in 2017 [74], who noted a preference for Cr-segregation into an $L1_2$-type structure in a 500 atom supercell produced via DFT, and who further noted a potential link between this behaviour and the magnetic properties of the material.

Extensive work by Schönfeld *et al* [75]. made use of a variety of electronic structure calculations, first-principles modelling techniques, X-ray scattering and APT analysis to determine the atomic structure of CrFeCoNi. They also found that equimolar CrFeCoNi appears to strongly favour the formation of the $L1_2$ motif, specifically demonstrating the segregation of Cr atoms to form an $(Fe,Co,Ni)_3Cr$ structure. Here, the authors state that the primary mechanism for this preferential ordering behaviour is the electrostatic interaction between Cr-Ni and Cr-Co pairs, driven by atomic size mismatch.

As identified previously, many - if not all - of these studies rely on indirect characterisation techniques, or the reduction of complex ordering information into one-dimensional parameters or labels, to describe the SRO of the CrFeCoNi system. These efforts introduce a degree of uncertainty into the validity of the final results; in many cases, the investigations above fail to produce a full description of the *character* of ordering in the structure - i.e. the form of lattice motifs - even when successfully *quantifying* the extent of SRO overall, or vice versa. Indeed, even the most successful studies have noted the propensity for segregation by Cr atoms in the system, but ultimately lack interpretation for the behaviour of the remaining atomic species. It is for these reasons that CrFeCoNi is selected as a natural successor to the prior CrCoNi investigation, outlined in 3. The total scattering technique will ideally quantify the extent to which the structure orders itself, whilst also clarifying the interactions of all atomic species in the structure.

4.2 Experimental Details

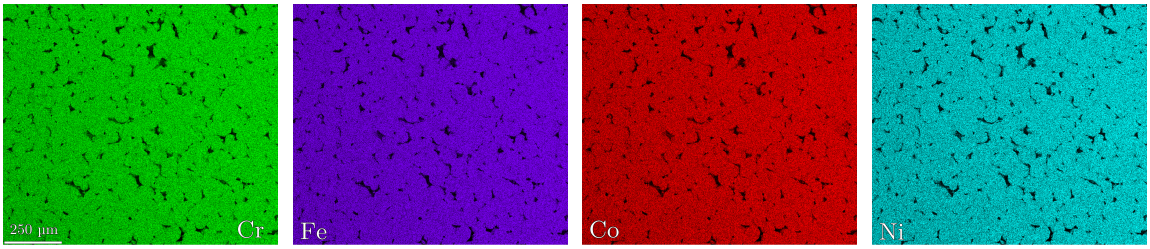

Figure 4.1: In-house EDX compositional results for the CrFeCoNi system, demonstrating the homogeneity of the system over 1mm^2.

The CrFeCoNi powder sample of nominally equiatomic composition 0.25 Cr- 0.25 Fe- 0.25 Co- 0.25 Ni at.% was prepared via gas atomisation. A small volume of each powder sample was subsequently placed in an Ar back-filled quartz tube, sealed, and sintered at 1200 °C for two hours to form a solid bar. The sample was then rapidly water quenched, to ensure a random distribution of constituent elements. In this instance, the sintering process also acted as a homogenisation step. Some of the initial powder sample was retained for external ICP-OES compositional analysis at the Sheffield Assay Office. A portion of the sintered bar was sectioned and mounted into conductive bakelite, ground, and polished for later in-house EDX. ICP-OES analysis provided a measured composition of 0.2429 Cr - 0.2453 Fe - 0.2535 Co - 0.2584 Ni at. fraction (±0.0005[1]); in-house EDX analysis showed a composition of 0.2484 Cr- 0.2474 Fe- 0.2495 Co - 0.2547 Ni at. fraction (±0.0005) mapping over 1mm^2, demonstrating strong agreement and an approximately equiatomic structure as desired. In both instances, oxygen, nitrogen and carbon content was found to be negligible. Images demonstrating the homogeneity of the powder CrFeCoNi samples may be found in Figure 4.1.

Neutron diffraction data for this experiment were collected at the ISIS Neutron and Muon Source, Oxfordshire (UK) on the Polaris Diffractometer. Samples were placed into vanadium can containers of 8mm diameter and loaded into a furnace, under vacuum, on the Polaris beamline. The *in-situ* temperature profile for this experiment is shown in Figure 4.2. The experiment was designed such that the atomic disorder of the alloy would be maximised at high temperatures - with the solid solution governed predominantly by entropic principles - followed ideally by the gradual reintroduction of local ordering with reduced temperature. In order to capture any potential order-disorder transition in the alloy, powder diffraction data was initially collected at room temperature (around 300 K) for approximately two hours, followed by a one hour heating ramp. The sample temperature

[1]The Sheffield Assay Office offer compositional analysis to >0.00005 at.%; errors in this instance have been given according to the precision of provided results.

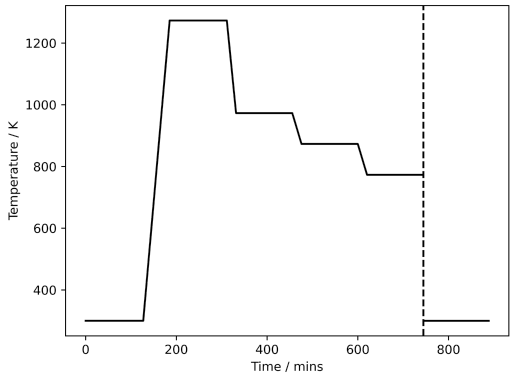

Figure 4.2: Temperature profile for the CrFeCoNi neutron total scattering experiment as performed at the Polaris Diffractometer of the ISIS Neutron & Muon Source (Oxfordshire, UK). The dashed vertical line corresponds to a break in the experiment, as the sample was re-assessed at room temperature at a later time.

was raised to 1000 °C (1273 K) before being lowered incrementally to 700 °C (973 K), 600 °C (873 K), and 500 °C (773 K). Each temperature was held for two hours to facilitate data collection, and the decreases in temperature occurred over 20 minute intervals. A further room temperature dataset was collected for two hours upon total cooling of the sample.

Raw diffraction data were processed using the Mantid software. As with prior experiments, Rietveld refinements of diffraction data were performed in the GSAS-II software, and PDF processing was undertaken using the GudrunN and SToG programmes (SToG Gudrun offsets). Comparative small-box modelling for this experiment was carried out via PDFGui, and large-box Reverse Monte-Carlo fitting was performed in RMCProfile.

4.2.1 GSAS-II Refinement

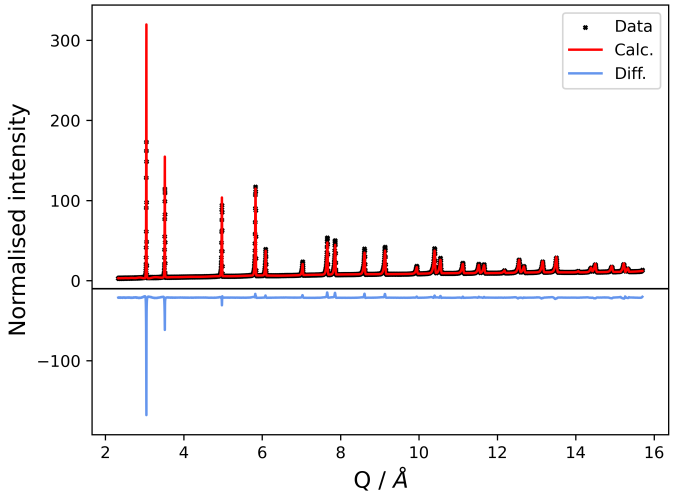

Figure 4.3: Rietveld refined neutron total scattering F((Q)) data for the CrFeCoNi system at 300 K, as taken from Bank 5 of the Polaris Diffractometer (ISIS Neutron & Muon Source, UK).

As described above, a GSAS-II Rietveld refinement was performed for all temperature datasets. Datasets were refined to a reduced χ^2 value of less than or equal to 30.0, and an R_w value of less than 5.0, indicating a strong goodness of fit and high quality of refinement. Examples of Rietveld fits from Polaris Bank 5 are available in Figure 4.3. As seen in previous Rietveld refinements, there is a pronounced discrepancy in peak heights between the fit and data for Banks 4 and 5; these are standard data artefacts brought about by the use of Time of Flight (TOF) diffractometers.

Further confirmation of the success of Rietveld fitting is found in Figure 4.4. The lattice parameter demonstrates an approximately linear increase with increased temperature as expected (3.571 Å at 300 K; 3.634 Å at 1273 K), as does the thermal U_{iso} parameter. Given that the increase in thermal oscillation of constituent atoms - described parametrically by the U_{iso} values - drives the increase in lattice parameter, the similarity in trends between graphs is an encouraging sign that the refinement has been completed successfully. It is worth noting that the U_{iso} parameter for each constituent element in the system was allowed to refine independently in this instance, leading to a 'spread' in values at high temperature. This result was not seen when allowing the U_{iso} values to refine independently in the CrCoNi. In the case of the CrFeCoNi sample, this 'spread' is likely caused by the larger divergence in atomic masses between constituent elements.

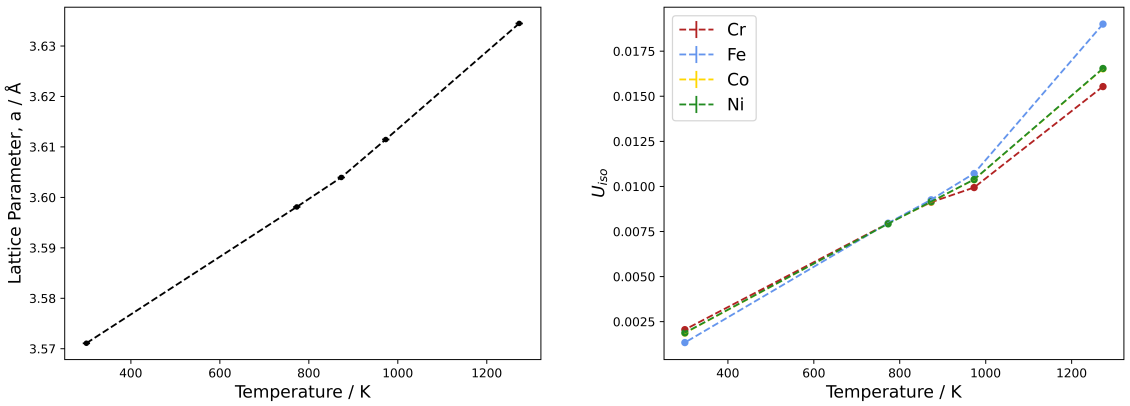

Figure 4.4: Fitted trends between 300-1273 K for the lattice parameter, a (Left), and thermal U_{iso} parameter (Right) in the CrFeCoNi quaternary alloy. Errors for both parameters are also present, but negligible. Both figures demonstrate the expected linear relationship with increased temperature.

4.2.2 GudrunN & SToG Processing

The following section details the processing of refined neutron diffraction data into the prerequisite $G(r)$ PDFs for large-box modelling. A selection of the PDFs produced by this processing may be found below. During GudrunN processing, lower and upper Q-limit bounds were selected at 0.9 Å^{-1} and 67.0 Å^{-1} for all temperature datasets. For the processed $G(r)$ inverse Fourier transform, a top-hat function width of 1.571 Å^{-1} and a minimum radius for Fourier transform of 2.0 - 2.1 Å were deemed most suitable for the produced PDFs, with minimal noise.

Comparative examples of the produced PDFs for the 300 K and 1273 K datasets are available in Figure 4.5. As discussed previously, the use of SToG post-processing is used to minimise the 'noise' introduced to the data via Fourier transformation, allowing easier, automated variation of the Q_{max}. Q_{max} values were assessed over a range of 30-40 Å^{-1}, and a final value of 36 Å^{-1} was selected as being most suitable. A comparative plot of PDFs for the 300 K dataset across Q_{max} values can be found in Figure 4.6.

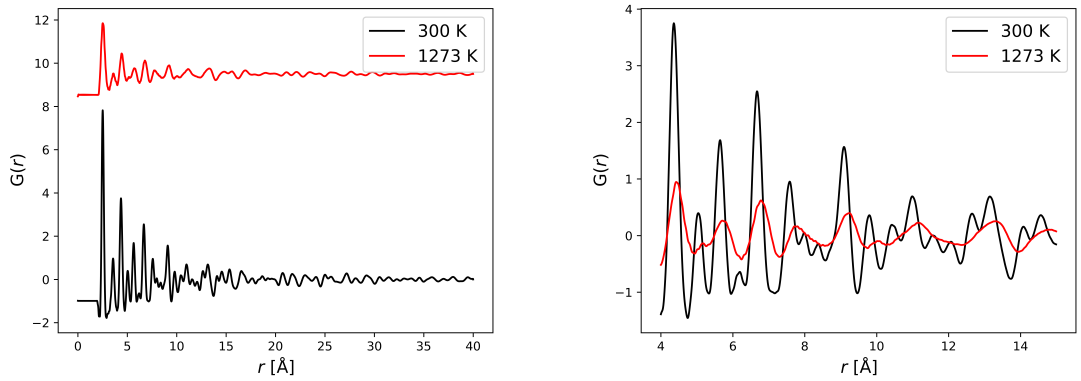

Figure 4.5: Left: $G(r)$ PDFs to 40 Åas produced by GudrunN for the CrCoNi system at 300 K and 1200 K; Right: A section of each PDF overlaid for comparison - note the peak broadening at high temperature due to thermal offsite displacement effects.

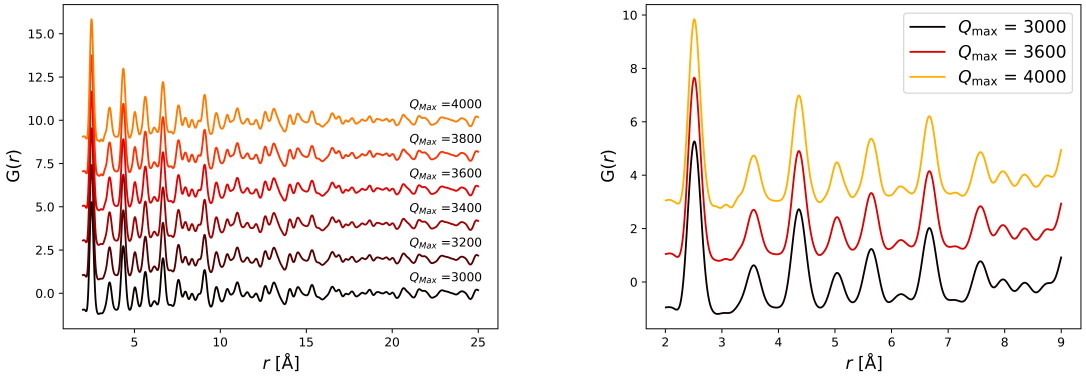

Figure 4.6: Left: SToG calculated G(r) PDFs for the CrFeCoNi ternary alloy at 300 K across a range of $Q_{\max}$ values (30 - 40 Å); Right: A comparison of PDFs when using end-member $Q_{\max}$ values, and the selected 36 Å.

4.3 Modelling & Analysis

4.3.1 PDFGui: Small-Box Modelling

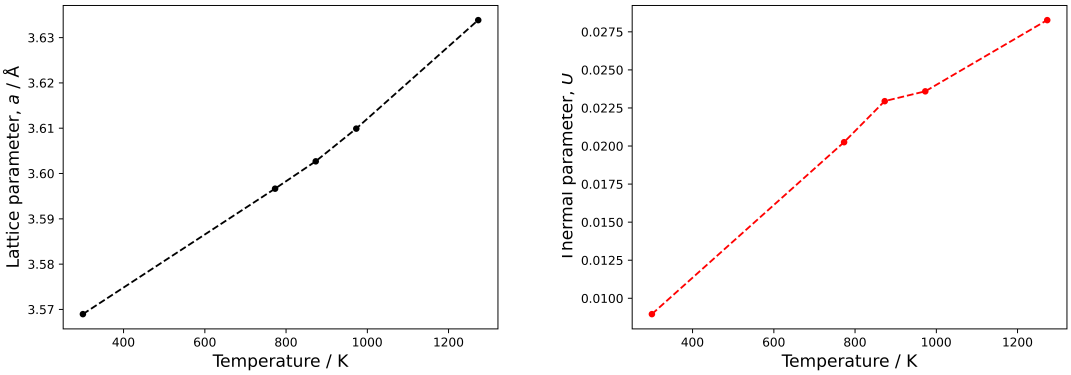

Figure 4.7: Fitted trends between 300 - 1200K for the lattice parameter, a (Left), and thermal U parameter (Right) in the CrFeCoNi quaternary alloy, as produced by PDFGui. Errors are present, but are negligible.

As with the prior CrCoNi investigation, PDFGui fitting was performed for all CrFeCoNi datasets between 300-1273 K, for unit cell refinement. Refinement of the unit cell parameter, a, demonstrates the expected increase in magnitude with increased temperature, ranging from 3.569 Å at 300 K to 3.634 Å at 1273 K; an equivalent increase in the thermal U parameter is also observed across a range of 0.001-0.0028Å^2. $Comparing GSAS-II Rietveld refinement with PDFGui modelling, lattice parameters are found to app$ $II counterparts (Figure 4.7)$.

As with the prior CrCoNi investigation, discrepancies between the SToG calculated $G(r)$ and the reduced χ^2-fit produced by PDFGui likely indicates the presence of SRO in the system (Figure 4.8); calculated PDF profiles do not appear to obey a an identifiable dampening curve - or other such function - suggesting a role for chemical occupancy effects. Once again, therefore, large-box modelling will be required to resolve the likeliest atomic structure of the material.

Unlike the CrCoNi system, the fitted scale value from PDFGui varies somewhat between fits. For temperatures 300-873 K, the scale value appears to be approximately equal to 1.0; in this instance, we would therefore simply perform RMC fitting over a scale window in the region of 0.9-1.1. However, above this temperature, the best fit scale appears to drop moderately: at 973K, it remains in the 0.9-1.0 range; beyond 1273K, it varies more dramatically. The fit for both when using a scale value of 1.0 is adequate, but the impact of this choice on the overall modelling at larger scales will require examination. To inform selection of the instrument resolution correction

parameter, the Q_{damp} value may be taken once again; here, the Q_{damp} value for the fits varies across a range of 0.024-0.027. For RMC fitting, we may therefore apply a window of values between 0.02-0.03.

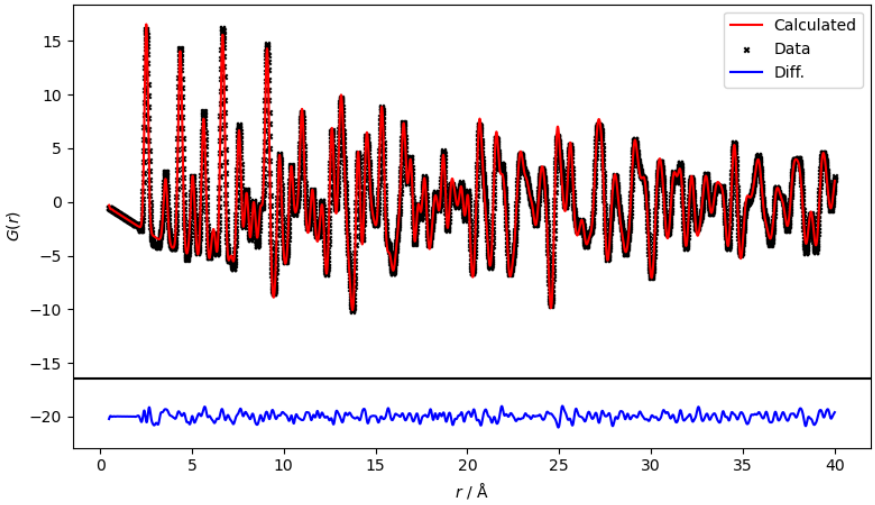

Figure 4.8: PDFGui fit to experimental data for the CrFeCoNi system at 300 K; the associated difference plot is presented below. Minor discrepancies between the experimentally derived and calculated PDFs may indicate uncaptured chemical short range order effects.

4.3.2 RMC fitting - random box, translations only (Grey Run)

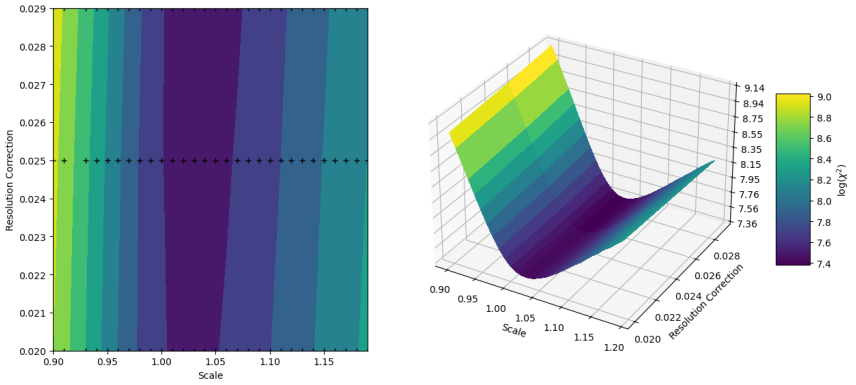

Figure 4.9: Results of 'grey' RMC fitting over 15Åfor the CrFeCoNi system at 300 K, when varying the scale (0.90-1.20) and instrument resolution correction parameters (0.02, 0.025, 0.029).

As a reminder, grey fitting requires no swapping of atomic species during χ^2-minimisation, thereby providing an excellent starting lattice structure for later colour fitting. In the following instances, all grey runs were performed using a minimum of 2 million translational moves; an arbitrary default atom type of Ni was used to construct a 20 × 20 × 20 unit cell large-box containing 32,000 atoms in an FCC lattice. In this instance, grey and colour fitting were performed consecutively across the initial stages of modelling. The scale and resolution correction parameter ranges for grey fitting were therefore selected with later full-colour fitting in mind. As with the prior CrCoNi investigation, ideal values for the scaling and resolution correction fitting parameters must be optimised across all temperature datasets when performing coloured fitting. Initial calculations were therefore performed using the 300 K dataset over a 0-15 Å range in r in order to isolate the impact of the scale factor from that of the resolution correction parameter during subsequent full-colour analysis. As previously described, the resolution correction is a primarily high-r corrective parameter, and therefore an appropriate scale factor for a given dataset can be selected more confidently when fitting over a shorter r-region. A 15 Å fitting range was selected to capture potential ordering behaviours out to a number of coordination shells, as well as to match the fitting ranges used in the CrCoNi investigation. To this end, scale values over a range 0.9-1.2 were assessed for their suitability in increments of 0.01, and - though their effect was anticipated to be negligible - appropriate resolution correction values of 0.020, 0.025, and 0.029 were applied for each scale value.

The final χ^2 results for grey fitting over 15 Å are available in Figure 4.9. There is a clear parabolic trend towards a best fit scale value between 1.0 and 1.05, in line with prior PDFGui modelling. Assessment of the calculated PDF at a scale value of 1.03 and an arbitrary instrument resolution correction value of 0.025 reveals a relatively strong fit to the data Figure 4.10. The difference plot

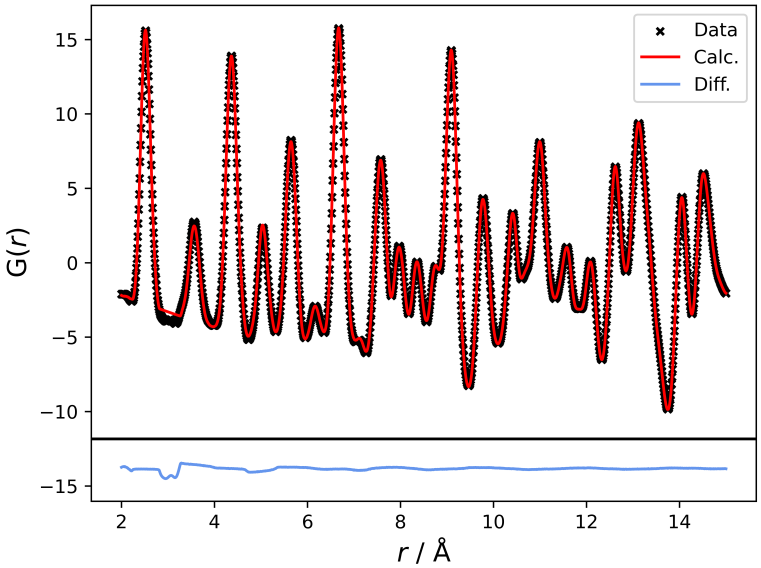

Figure 4.10: RMCProfile calculated$G(r)$ for the CrFeCoNi system at 300 K as modelled with a single atom type ('grey' fitting).

show little discrepancy between the fitted PDF and the experimental data across all of the available r-space. The strength of the fit is a likely indication that the displacements for the structure are, in this instance, well-fitted, and that the structure could potentially be described by a random distribution of constituent elements. Further fitting is required to determine the validity of this assertion, however. The Q_{damp} value determined by PDFGui fitting (0.025 at 300K) also matches the resolution correction value here exactly, providing greater confidence in the quality of the fit.

4.3.3 RMC fitting - translations and swaps (Colour Run)

To assess the impact of site occupation on the quality of fit - or, more specifically, the impact of potential chemical short-range ordering - further fitting is performed allowing both spatial translations and the swapping of chemical species. In all cases, the input large-boxes used in this experiment were constructed with random site occupation; that is, constituent atomic species were initially distributed statistically randomly across lattice sites in all boxes (according to the concentrations determined by ICP-OES analysis), to avoid biasing of the final configurational results. As with prior single-atom fitting, a large box of 32,000 atoms ($20 \times 20 \times 20$ FCC unit cells) was constructed for fitting. As described above, initial fitting was performed to 15 Å, using a scale range of 0.9-1.2, and resolution correction values of 0.020, 0.025 and 0.029.

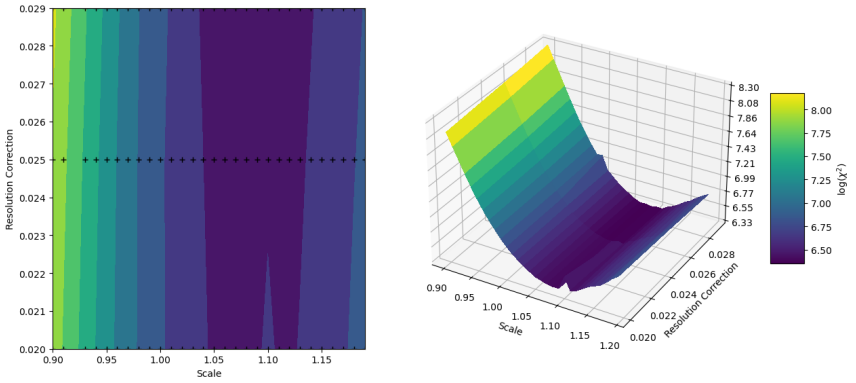

Figure 4.11: Results of 'grey' RMC fitting over 15Å for the CrFeCoNi system at 300 K, when varying the scale (0.90-1.20) and instrument resolution correction parameters (0.02, 0.025, 0.029)

Figure 4.11 demonstrates the final χ^2 values extracted from these fitting regimes. As is evident from the approximately parabolic trend in χ^2 values along the scale axis and the negligible change in χ^2 along the resolution correction axis, fitting over the shorter r region successfully limited the impact of the resolution correction parameter on the overall quality of fitting. In this instance, the best χ^2 fit was achieved across a short range of scale values in the region 1.05-1.12. It is also worth highlighting, prior to further analyses, that the χ^2 plot along the scale axis has adopted an 'asymmetric' parabolic profile. More plainly, the best χ^2 value still occurs at a given scale value - here, a value of 1.09 - but the increase in χ^2 away from this value of scale is not symmetric about the minimum. The exact cause of this effect is, at present, unexplained, but the asymmetry itself could provide a a 'tolerance' for the selection of scale values when fitting. If the variation in the value of χ^2 is lesser at values of scale *above* the minimum - and, naturally, greater at values of scale below the minimum - then it is likely that these larger values of scale will also demonstrate greater similarities in their final configurational behaviours.

Using the previous χ^2 results as a base-line, an appropriate range of scale values (1.02-1.13) were subsequently applied to a wider 40 Å r-range fitting regime for the initial 300 K dataset. An appropriate range of resolution correction values was selected for fitting from prior studies using the Polaris diffractometer between 0.02 - 0.03. The final χ^2 results for this experiment are presented in Figure 4.12. It is immediately apparent that this particular fitting regime has not been successful in identifying a uniquely 'strong' candidate for the best suite of fitting parameters: the existence of 'double-minima' - two approximately equal minimum χ^2 values with substantially different input parameters - presents a challenge. One minimum exists at a scale value of 1.03-1.04 and an instrument resolution correction value of 0.027-0.028; the second, at a scale value of 1.10-1.11, and a resolution correction value of 0.021-0.022. Visually, the fits for both simulations appear equivalent,

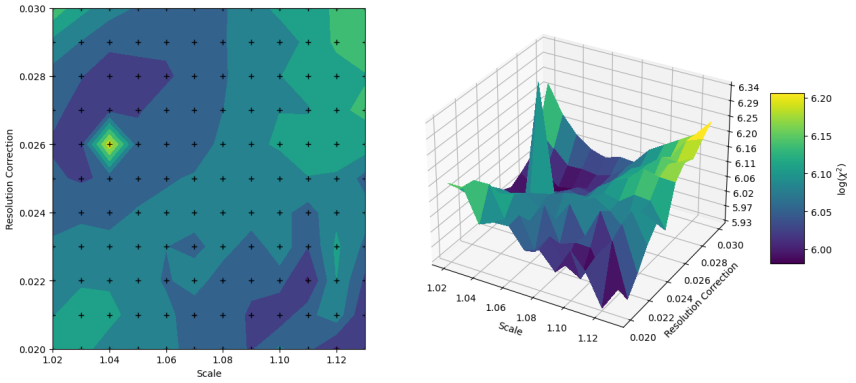

Figure 4.12: Results of 'grey' RMC fitting over 40Å for the CrFeCoNi system at 300 K, when varying the scale (1.01-1.13) and instrument resolution correction parameters (0.02, 0.025, 0.029), containing the double-minima solutions.

with minor fluctuations in the difference plot attributable to standard variations between models. As a reminder, prior PDFGui analysis had identified a scale value of approximately 1.0 at 300 K, with an associated resolution correction value of approximately 0.025. That the scale value for the first minimum would approximately coincide with both values to within error is a positive sign, though the exact cause for the double-minimum phenomenon is as-yet unexplained.

Given that prior fitting over a shorter 15 Å r-range produced a well-defined χ^2 minimum, and that local ordering should be well-defined to within a number of coordination shells inside a 15 Å limit, it was decided that all further temperature data for this sample would undergo fitting to this lower limit. The 40 Å fitting is, however, retained for comparative purposes. An example of the large-box produced by fitting the 300 K dataset over 15Å is presented in Figure 4.13, and its associated PDF function may be found in Figure 4.14. Similarly to the CrCoNi fitting of the previous chapter, one can draw few conclusions from the function itself. The difference plots for best-fit RMC simulations are once again featureless, and the distributions of off-site displacements in the model are approximately Gaussian as anticipated.

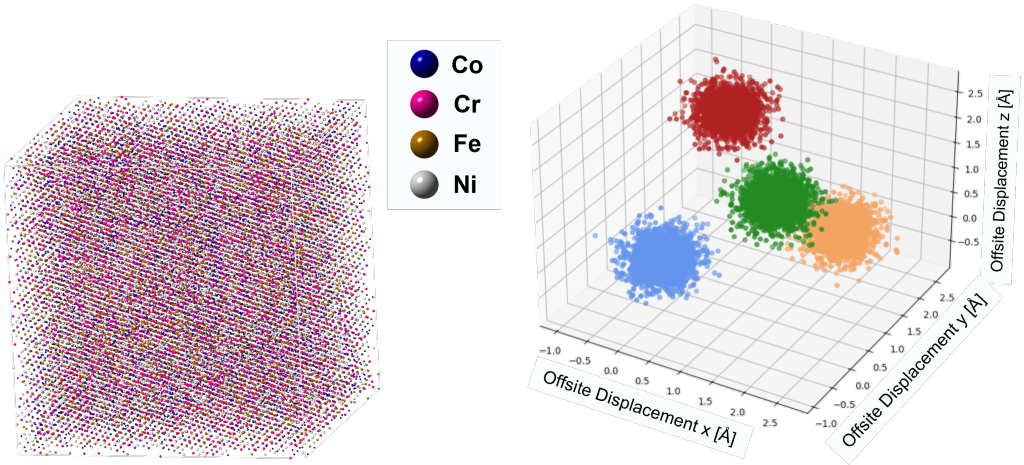

Figure 4.13: Left: The large-box as produced by RMCProfile fitting for the CrFeCoNi system at 300 K over 15 Å, using a scale value of 1.03 and a resolution correction value of 0.025; Right: The offsite displacements for this large-box, demonstrating an approximately gaussian - and therefore random - distribution.

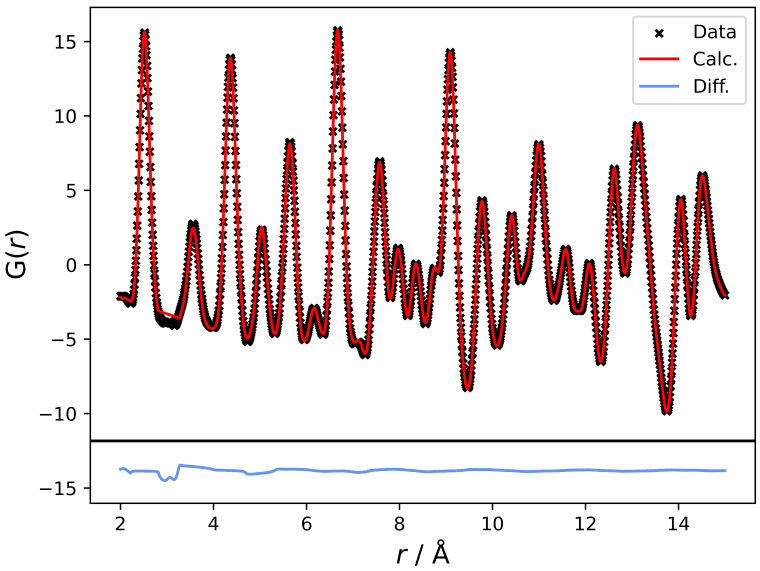

Figure 4.14: The RMCProfile fitted PDF for the CrFeCoNi system at 300 K over 15 Å. The difference plot is, in this instance, essentially featureless.

4.3.4 Clapp Configurational Analysis

Following the process outlined in the analysis of the CrCoNi ternary alloy, a final instance of PDF fitting was performed for each of the temperature datasets over the 15Å limit. Large-boxes of 32,000 atoms ($20 \times 20 \times 20$ FCC unit cells) were generated with a random distribution of atomic species. The best-fit parameter suites determined by χ^2 fitting for each temperature were used as input parameters for the RMCProfile fitting regime. In all cases, each fitting regime was performed a total of 40 times, and the configurational enhancement values (β) were calculated for each fit. The enhancement values were then mean-averaged over all 40 boxes to produce the 'likeliest' atomic structure for each temperature case, and the standard deviation across these values is applied as error.

As mentioned above, prior CrCoNi analyses required the formation of only three pseudo-binaries per dataset; that is, the Cr:Ψ, Co:Ψ, and Ni:Ψ pseudo-binaries. Whilst this analysis is not trivial, it is relatively simple to reconstruct the configurational behaviour of atoms in the system when each pseudo-binary can be used to represent the distribution of a single atomic species. Applying this form of analysis to higher-order systems, however, introduces a greater number of possible pseudo-binary analyses to the system - thereby naturally increasing the complexity of analysis - due to the possible groupings of atomic pairs or triplets. In the case of the CrFeCoNi quaternary alloy, seven pseudo-binary pairs may be produced from the four constituent atomic species: Cr:Ψ, Fe:Ψ, Co:Ψ, and Ni:Ψ, each essentially modelling the distribution of single atomic species; and (Cr-Fe):(Co-Ni), (Cr-Co):(Fe-Ni), and (Cr-Ni):(Fe-Co).

The final mean-averaged enhancement factors for the 300 K dataset (scale value 1.09, resolution correction value 0.025) are presented in Figure 4.15. Within statistical bounds - i.e. the three standard deviation limit applied to each pseudo-binary delineating statistical enhancement - several of the pseudo-binaries appear to demonstrate little to no ordering behaviour whatsoever. Each of the Co:Ψ, Ni:Ψ, (Cr-Ni):(Fe-Co) and (Cr-Fe):(Co-Ni) pseudo-binaries show approximately random configurational distributions, indicating no overall ordering preferences.

Analysis of the Cr:Ψ, Fe:Ψ, and (Cr-Co):(Fe-Ni) pseudo-binaries, however, suggests very clear evidence for preferential ordering behaviours in the model. All three pseudo-binaries demonstrate strong enhancements to the C7, C16, C34, C58 or C59 configurations, though this is not a complete picture of *all* enhancements shown in Figure 4.15. As with prior CrCoNi fitting, this distinct patterning of enhanced configurations is connected to the presence of the $L1_2$ structure. As described previously, the $L1_2$ structure places atoms of type 'A' at the corners of the unit cell, and the remaining atoms of type 'B' on its faces; when translating this to nearest-neighbour configurations, this structure manifests as a four-atom square of 'dislike' atoms in the horizontal plane about the atom at the origin, and is labelled as the C16 configuration. If this configuration is found to be sta-

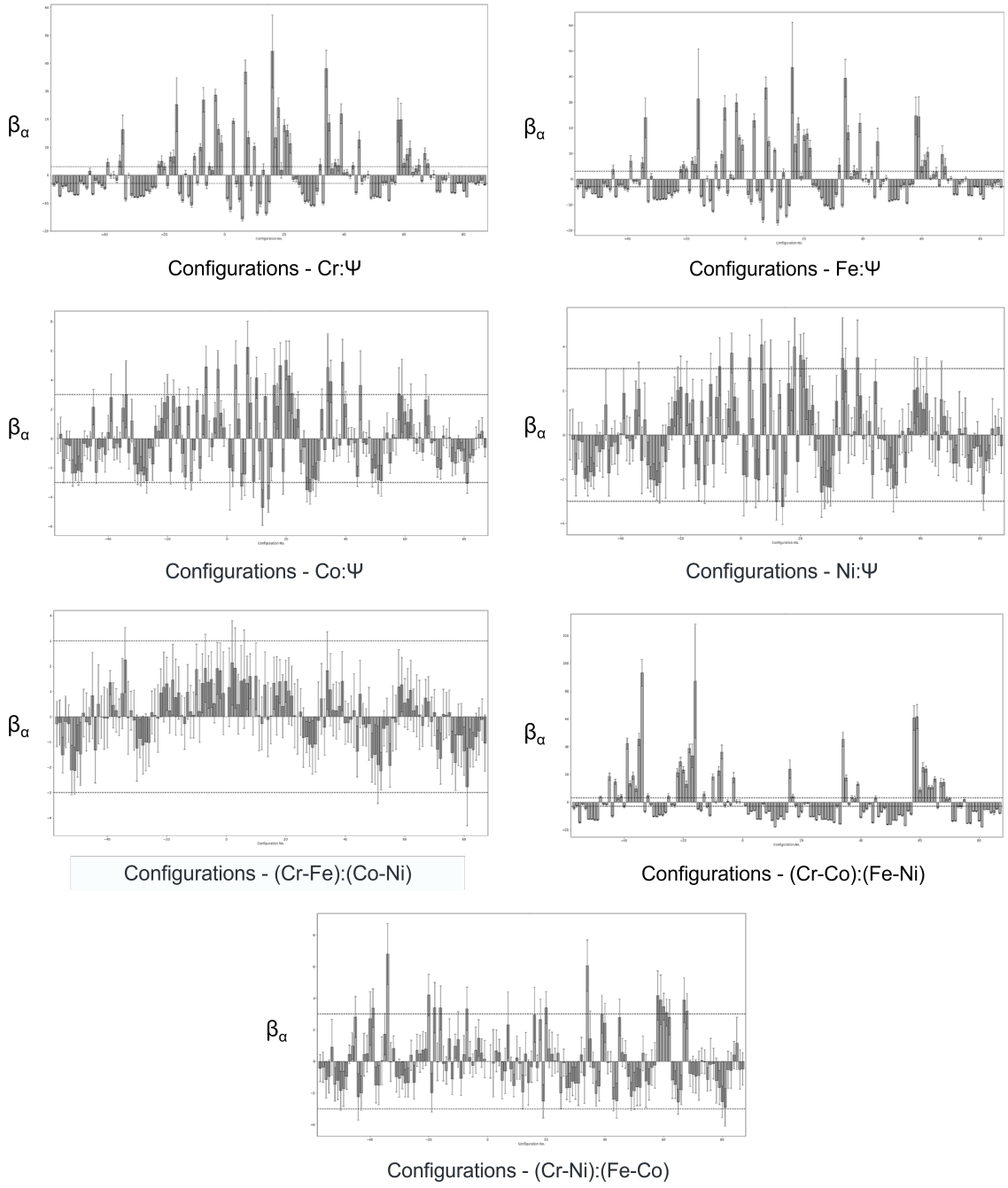

Figure 4.15: Histograms of the pseudo-binary enhancement factors for atomic configurations in the CrFeCoNi system at 300 K; the large-box for this run was generated using a scale factor of 1.09 and a resolution correction parameter of 0.025. Errors are produced as a standard deviation across 40 simulated boxes.

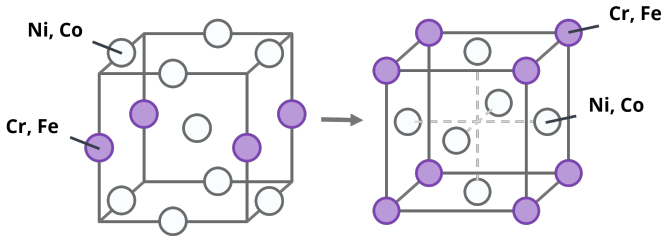

Figure 4.16: The structure of the CrFeCoNi system, as determined via pseudo-binary analysis.

tistically enhanced in a non-long-range ordered structure, then it stands to reason that associated structures - i.e. those that differ from the C16 configuration by the presence or absence of one or two 'dislike' atoms - would be co-enhanced alongside the C16 configuration. This associated family of atomic motifs is demonstrated most clearly in the (Cr-Co):(Fe-Ni) pseudo-binary, which shows very strong enhancement to this ordering pathway without particular enhancement to otherwise 'unrelated' configurations.

Unlike the CrCoNi enhancements to the $L1_2$ structure, however, there is no evidence of a 'sawtooth' type patterning to the enhancement of configurations. In the case of CrCoNi, this wave-like pattern in the averaged β values was taken to be potentially indicative of preferential ordering to within a single coordination shell (i.e. preferential ordering in first nearest-neighbour atoms), with ordering at greater distances less statistically meaningful. The *lack* of this patterning in the configurational enhancements of the CrFeCoNi system therefore indicates a legitimate preference for the formation of the complete $L1_2$ structure across these particular pseudo-binary groupings, and a likely second shell effect that distinguishes the system completely from the associated $D0_{22}$ structure (otherwise indicated by a co-enhancement to the C17 configuration).

From these enhancements, we can describe the likeliest structure for the CrFeCoNi alloy at room temperature: Cr and Fe atoms appear to preferentially segregate to the corners of the unit cell, with Ni and Co atoms then randomly distributing themselves across the remaining 'face' sites to produce the $L1_2$ structure (Figure 4.16. The lack of enhancement to the pseudo-binary in which Cr and Fe atoms are grouped (i.e. (Cr-Fe):(Co-Ni)) would suggest that the instances of this segregation to the corners of the unit cell are spatially distinct from one another. Cr and Fe atoms do not *share* the corners of the unit cell, but instead form their own $L1_2$ structures separately to one another. We can visualise this distinction by plotting the positions of origin atoms in the C16 family of enhanced configurations, as seen in Figure 4.17. Cr and Fe atoms in these configurations show no overlap with one another, nor particular segregation, suggesting an approximately random distribution of atoms with $L1_2$-type ordering.

This behaviour can be seen across all temperature datasets, with no evidence for particular ordering

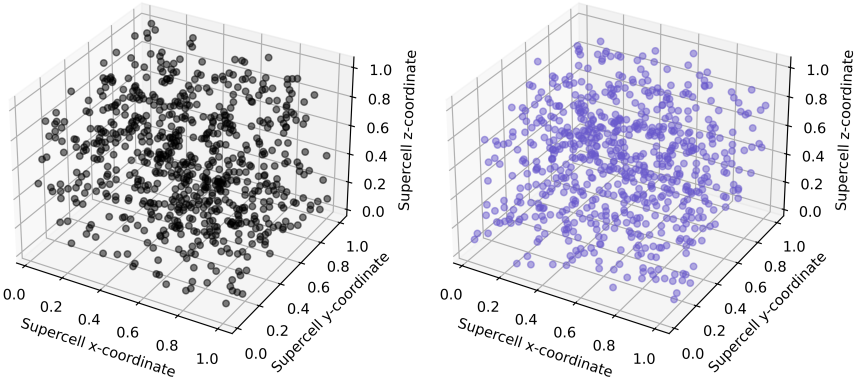

((a)) Cr atoms ((b)) Fe atoms

Figure 4.17: Mapped Distributions of atoms associated with enhanced $L1_2$ configurations. The lack of clustering or overlap suggests that Cr and Fe atoms distribute distinctly from one another.

transitions at any temperature. In every case, it would appear that Cr and Fe atoms at least partially preferentially migrate to the vertices of the unit cell, and the remaining Ni and Co atoms order themselves randomly across the remaining lattice sites. There are, however, substantial differences in the absolute enhancement of configurations (i.e. the values of β for specific configurations) across temperatures. When raising the temperature of a given sample, one would anticipate a greater degree of disorder in the sample as atoms in the system become governed by entropic principles, as opposed to enthalpic principles. By extension, we would expect to see an overall decrease in the heights of peaks in the configurational histograms associated with an increase in temperature. Nonetheless, this behaviour is not observed in the CrFeCoNi sample as temperatures increase. Indeed, when raising the temperature from 300 K to 1273 K, the enhancements to particular configurations appear to increase (Figure 4.18(a)), directly contradicting the expected trend. As the temperature is then decreased (1273 K to 973 K), β enhancement values drop substantially, before rising gradually once again as the temperature of the sample decreases further (Figure 4.18(b)).

There is no clear explanation, at present, for this behaviour. The trend from 973 K down to 773 K (and upon re-analysis at room temperature post-heating) matches the expected thermodynamic behaviour (Figure 4.18(c)). It is believed that the 'increase' in ordering with initially increased temperature may be explainable through the slow diffusion kinetics of multi-principal element materials: over the 300 K to 1273 K temperature range - each running for two hours - the sample had not had sufficient time to disorder. The 300 K sample, when fabricated, was quenched, and some order may have been introduced on heating - but may not have been in a completely ordered state. As thermal energy is provided to the system, this order may have then been increased initially

by the heating process, before beginning to disorder over time with the applied heat. By the time the sample had reached 973 K, still above the disordering temperature for the material, sufficient time had passed for the sample to clearly disorder, leading to the reduction in β values in this dataset. Then as the temperature was lowered, the ordering behaviour of the material progressed as anticipated, leading to the final (expected) increase in configurational enhancements.

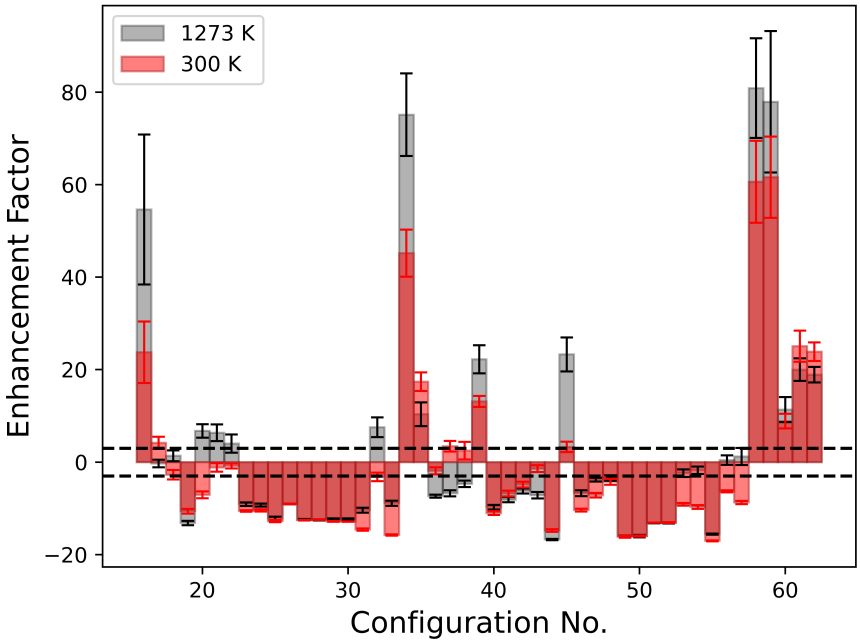

((a)) 300 K - 1273 K

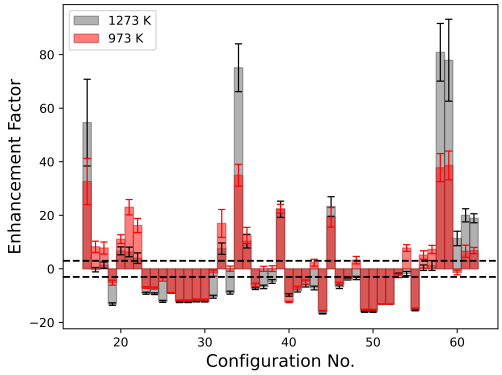

((b)) 973 K - 1273 K

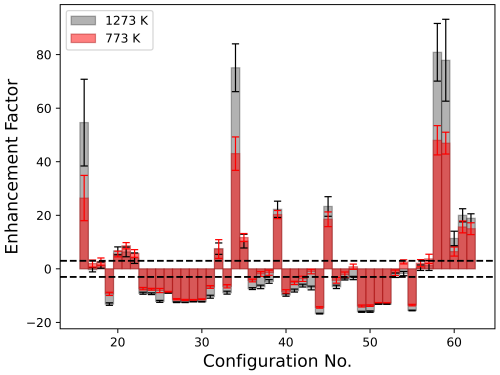

((c)) 773 K - 1273 K

Figure 4.18: Comparison plots of enhanced configurations for CrFeCoNi across the 300 - 1273 K temperature range. As is evident, the 1273 K case counter-intuitively demonstrates the greatest degree of ordering, though at 973 K the material shows disordering and re-ordering in line with expected thermodynamic behaviours.

4.3.5 RMC fitting - translations and swaps (Pastel Run)

As a final confirmatory analysis, it is possible to perform the 'pastel' fitting outlined in the CrCoNi investigation. Falling somewhere between single-atom 'grey' fitting and 'colour' fitting with all constituent elements, 'pastel' fitting uses each pseudo-binary reduction as an input structure for the fitting regime. The relative simplicity of the ternary CrCoNi alloy leads to a comparatively small number of potential pseudo-binaries for analysis. The quaternary CrFeCoNi alloy, however, provides a greater number of potential 'pastel' structures: not only can the structure be reduced into the seven pseudo-binaries outlined above, but it may also be divided into a number of pseudo-*ternaries*. These pseudo-ternary fits combine two of the constituent atomic species into a single atom type. For example, the combination of Cr and Fe atoms leads to a Co-Ni-(Cr-Fe) - hereby labelled Co-Ni-Ψ - input structure, and an equivalent combination process can be applied to all unique atomic pairs. We can then determine the efficacy of the RMC fitting method for chemically-complex structures by comparing the behaviour of 'combined' atoms across the pseudo-binary and pseudo-ternary fits. The (Cr-Fe):(Co-Ni) pseudo-binary, for instance, can be directly compared to the Co-Ni-Ψ pseudo-ternary for the ordering behaviours of the (Cr-Fe) grouping, to increase confidence in the final structural result.

Presented below are a selection of key results from the pseudo-binary (Figure 4.19) and pseudo-ternary pastel fitting, as described above, for the 300 K temperature dataset. This particular dataset was selected for analysis due to its relatively strong configurational enhancements when performing full 'colour' fitting. Taking the Cr:Ψ, Fe:Ψ, Co:Ψ, and Ni:Ψ pseudo-binaries initially, an interesting result emerges: all four of these analyses demonstrate clear $L1_2$ ordering pathways. This is perhaps an expected result in the case of the Cr:Ψ and Fe:Ψ pseudo-binaries, which have previously shown enhancements to the C16 'family' of associated configurations; it is a less anticipated result in the case of the Co:Ψ and Ni:Ψ pseudo-binaries, which have previously demonstrated a statistically random distribution across temperature datasets.

This is a trend repeated across the remaining binary analyses: the (Cr-Co):(Fe-Ni) pseudo-binary demonstrates the same strong enhancement to the $L1_2$ ordering pathway as prior analyses; the (Cr-Fe):(Co-Ni) and (Cr-Ni):(Fe-Co) pseudo-binaries, however, demonstrate newfound enhancements - albeit less convincingly - to the same C16 ordering pathway. This does not, however, necessarily indicate a failure of the method to identify the ordering when fitting with all available atomic species. It is likely that the experimentally derived PDF possesses a particular 'patterning' of peaks related to the $L1_2$ structure previously identified in the system. When reducing the degrees of freedom available to the system - i.e. the number of available atomic species, and by extension the number of partial functions used to fit to the PDF - the algorithm attempts to optimise the chemical order of the model to best match this behaviour. The final configurational results for these previously randomly distributed pseudo-binary reductions therefore reflect the *existence* of ordering

in the system, without correctly identifying the form and quantity of said order. The ternary investigations demonstrate near-identical results, and therefore require little further description; an example of the (Cr-Co):(Fe-Ni) pseudo-binary as produced by ternary pastel fitting is presented in Figure 4.19.

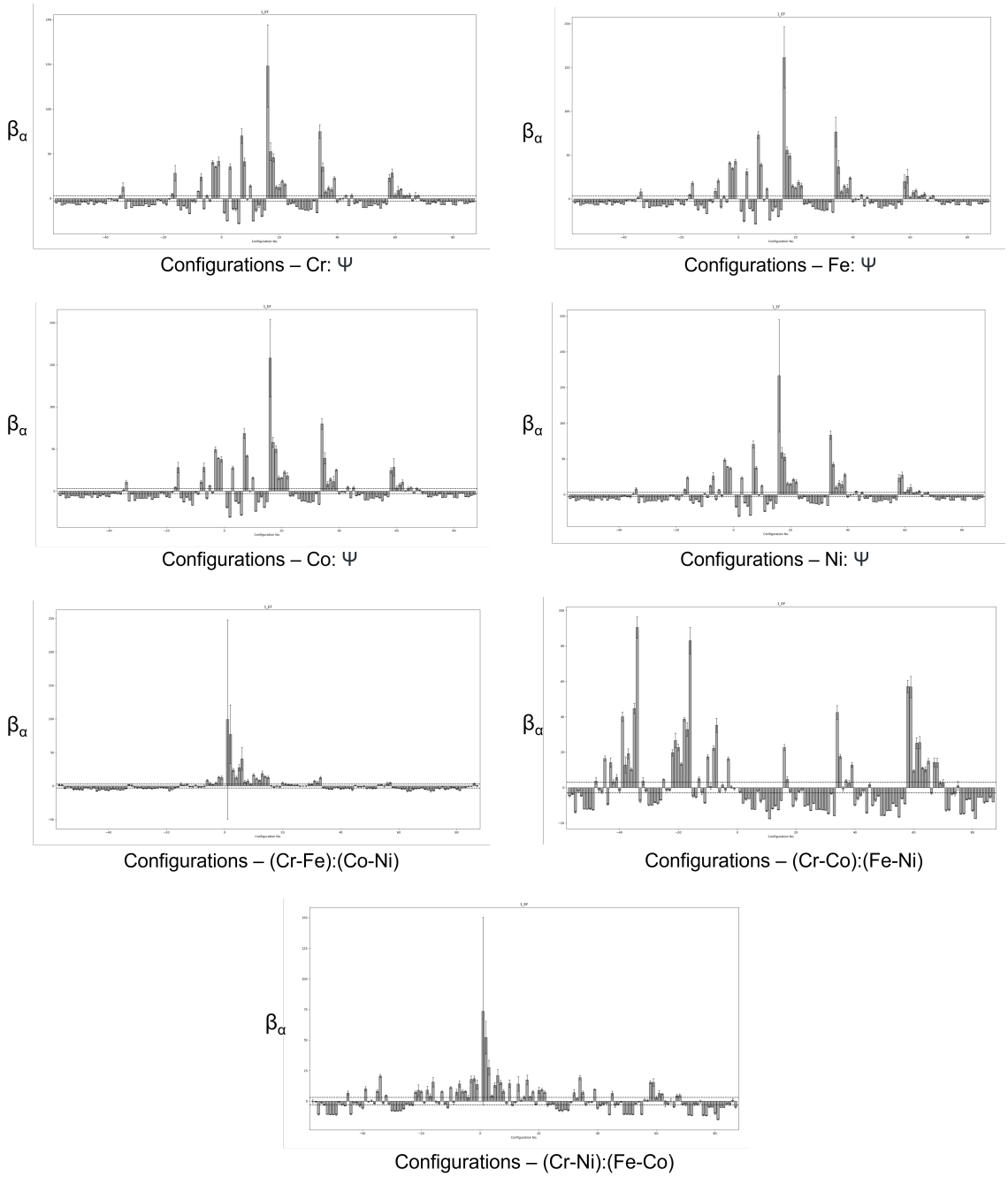

Figure 4.19: Histograms of the pseudo-binary enhancement factors for atomic configurations in the CrFeCoNi system at 300 K when using 'pastel fitting'; the large-box for this run was generated using a scale factor of 1.09 and a resolution correction parameter of 0.025. Errors are produced as a standard deviation across 10 simulated boxes.

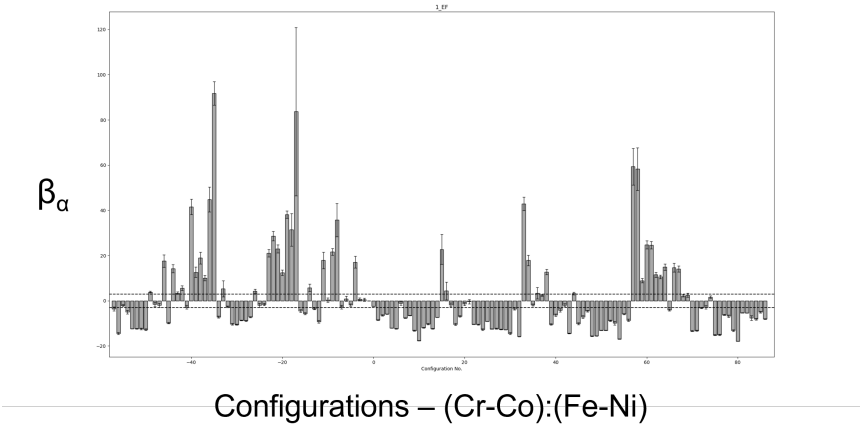

Figure 4.20: Configurational enhancements for the (Cr-Co):(Fe-Ni) pseudo-binary, as produced by pseudo-ternary fitting of the CrFeCoNi system at 300 K (scale = 1.09, resolution correction = 0.025). The fit to the data was produced using three atom types: Cr, Co, and 'X' (Fe and Ni combined).

4.3.6 RMC fitting - full r-range

A final point of comparison is to perform a configurational analysis of the 'best fit' box produced by the initial Å fitting regime attempted above. Though the presence of double-minima in the final χ^2 analysis presents an interesting problem when identifying the most suitable suite of fitting parameters - thereby decreasing confidence in the final result - a comparison may be made to the truncated 15Å fits. The following comparisons are made using results from single boxes, though it is anticipated that the averaged results would demonstrate similar ordering behaviours.

A comparison of configurational enhancements for the 40Å fit with the lowest χ^2 against the best-fit over 15Å is presented in Figure 4.21. For the purposes of the following analysis, both minima are analysed for configurational enhancement. It is immediately apparent, in the fit corresponding to a scale value of 1.11 and a resolution correction value of 0.022, that there are very clear enhancements to configurations associated with the $L1_2$ ordering pathway in the Cr:Ψ, Fe:Ψ, and (Cr-Co):(Fe-Ni) pseudo-binaries, closely matching those seen in the 15Å fitting.

Interestingly, very similar arguments can be made for the 40Å fit corresponding to a scale value of 1.04 and a resolution correction value of 0.028 (Figure 4.22). The $L1_2$ ordering pathway is also demonstrated somewhat clearly by the (Cr-Co):(Fe-Ni) pseudo-binary, providing even greater confidence in the final results across all fittings. In the case of the Cr:Ψ and Fe:Ψ pseudo-binaries, however, this argument is less strong: though there is some evidence of enhancement to the C16

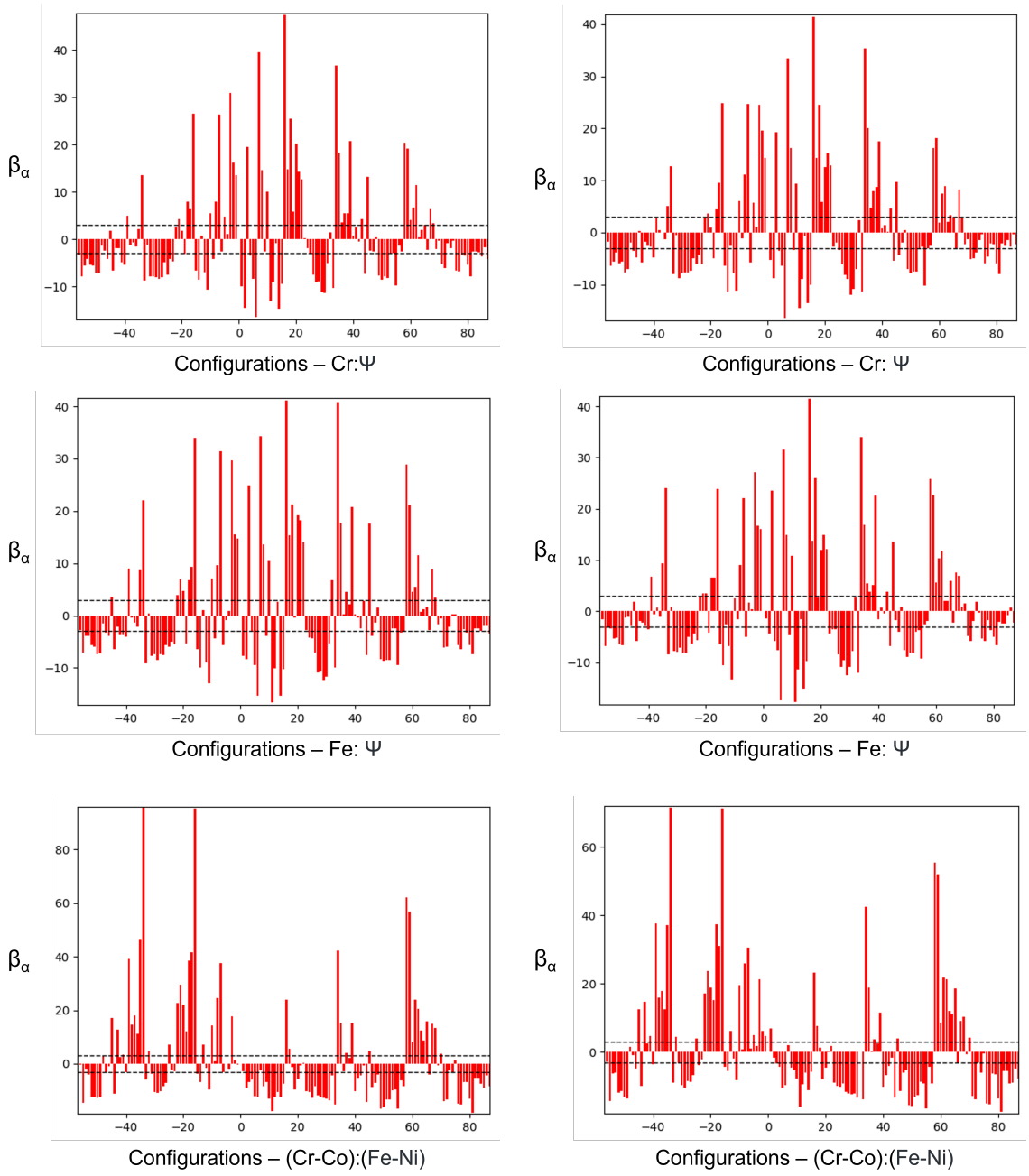

Figure 4.21: Comparison between configurational enhancements for the ordered pseudo-binaries in the CrFeCoNi system at 300 K when fitting over 15 Å (Left) and 40 Å (Right) (scale = 1.11, resolution correction = 0.022). The similarity between the datasets provides confidence in the final results outlined above.

family of atomic configurations, the concurrent enhancement to a greater number of configurations across both pseudo-binaries makes this result significantly less clear. There is a degree of configurational uncertainty associated with fitting over a larger r-range, with small but statistically significant enhancements to configurations adjacent to or even distinct from the $L1_2$ pathway. These enhancements are not large ($\beta_{C1} \approx 12$), but represent an equivalent 'noise' in the dataset introduced by fitting over a larger r-scale that is not seen when fitting over 15Å. Taken collectively, this is likely indicative of remaining optimisation errors, such that further optimisation of the fitting is required for the larger r-range.

These results lend some credence to the selection of fitting parameters when assessing the 300 K dataset over 15 Å. When fitting over 15Å, a scale value of 1.09 and resolution correction value of 0.025 were selected for modelling. Given the somewhat arbitrary selection of resolution correction parameters over shorter fitting distances, comparison of these values between runs is less significant. However, that the 'best fit' scale value over 15 Å is equal to 1.09, and the scale value over 40 Å that produces the clearest ordering behaviour is 1.11, it is possible to suggest that the configurational analyses previously produced are likely to be physically representative. It is a significant result to find that the 40Å fitting regime demonstrates the same configurational enhancement as the 15Å model, even if the wider r-range introduces a larger spread of enhanced configurations present in the model. Capturing coordinations out to a larger distance and finding that RMCProfile has converged upon a single solution (or set of solutions) implies that there is a degree of tolerance associated with the optimisation of fitting parameters, and provides additional confidence to the validity of the final local configurational solutions identified when fitting over a short distance.

The results presented above - that is, the apparent segregation of Cr and Fe into the 'square'-like nearest neighbour pattern constituting the $L1_2$ structure - are well supported by existing literature. As briefly mentioned in Section 4.1, Tamm *et al.* noted the de-enhancement of Cr-Cr or Fe-Fe pairs, which can be linked directly to the formation of distinct Cr or Fe C16 configurations; Schönfeld *et al* note an equivalent potential Cr segregation. Importantly, Niu *et al.* note a reduction in magnetic frustration when Cr atoms coordinate anti-ferromagnetically, providing an overall 'coupling' to the remaining constituent elements. This necessarily requires the segregation of Cr atoms to the corners of the FCC unit cell. Given the formation of the $L1_2$ structure in the results above, this result may be supported somewhat, though the exact causes of such SRO behaviour would require further investigation before this hypothesis may be confirmed.

Structural agreement in this instance does not mean, however, that all results from literature are supported by the experimental data provided above. Schönfeld *et al.* [75] specifically identify an order-disorder transition in the CrFeCoNi alloy across a temperature range of 500-600 K, with the $L1_2$ structure specifically stabilised at around 500 K. When analysed using the total scattering technique, however, the form or quality of ordering present in the system does not vary with

temperature; the $L1_2$ structure is present at all temperatures, though the enhancement of the C16 configuration and its associated structures do vary with temperature. More specifically, the $L1_2$ structure appears to be present at all temperatures across a range of 300-1273 K, with limited evidence for any disorder transition. Though this could be due, in part, to the thermal history of the parts analysed, further investigation would be required to determine the origin of this discrepancy in results.

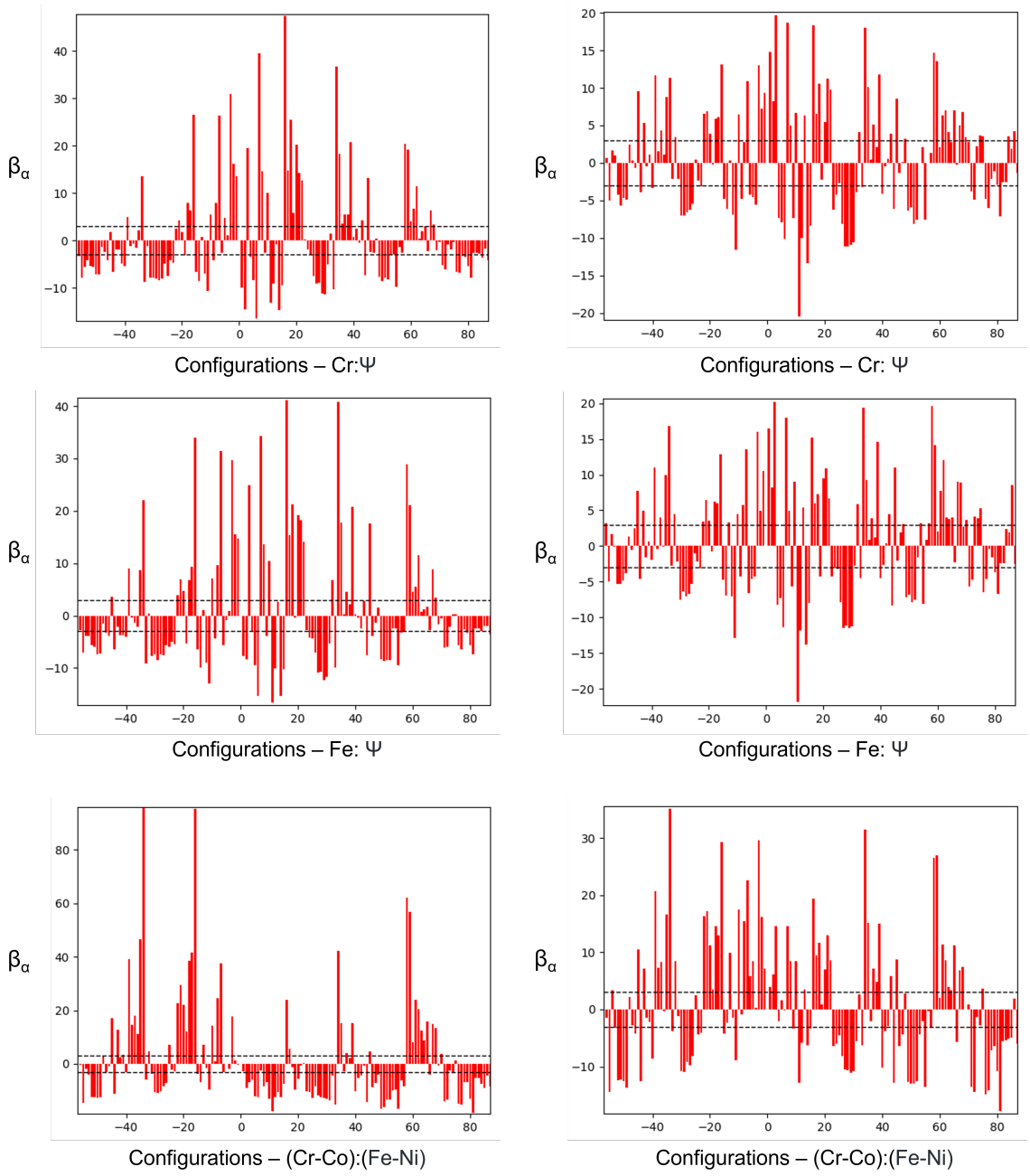

Figure 4.22: Comparison between configurational enhancements for the ordered pseudo-binaries in the CrFeCoNi system at 300 K when fitting over 15 Å (Left) and 40 Å (Right) (scale = 1.04, resolution correction = 0.028Å^{-1}). Though providing the second χ^2 minimum of the 40 Å fitting, the enhancements in the structure are less well defined.

Warren Cowley Parameters

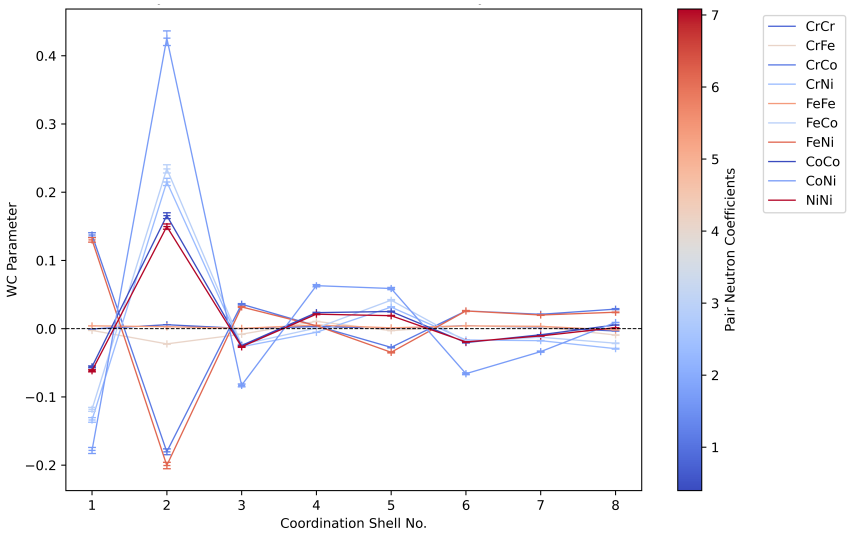

Figure 4.23: Warren-Cowley parameters as calculated for a CrFeCoNi large-box at 300 K, produced using a scale value of 1.09 and a resolution correction value of 0.025. The oscillatory behaviour within the first few coordination shells indicates strong local ordering effects.

As in the case of the CrCoNi study, and as a final point of comparison, it is worth assessing the Warren-Cowley parameters of the CrFeCoNi system to identify potential trends or agreements with literature. In the first instance, the Warren-Cowley parameters for the 300 K dataset are presented. As described in Section 3.4.4, in a perfectly long-range ordered binary $L1_2$ structure, one would observe the oscillation of α values about zero across coordination shells for associated atomic pairings. In the CrFeCoNi dataset, this perfect oscillation is not observed: instead, the α parameters for each atomic pairing appears to oscillate about zero according to a 'damped' pattern out to the 8th coordination shell. As with the CrCoNi ternary, it therefore appears that the $L1_2$ structure identified through fitting holds true to within a few coordination shells, and at larger distances the system tends towards a random distribution of constituent elements, as the α values approach zero.

Analysis of the variation in Warren-Cowley parameters according to neutron coefficients (Figure 4.23) also appears to show that the atomic pairs with the largest and smallest pair neutron coefficients demonstrate equivalent trends to one another across coordination shells, and produce lower α values overall. Those with values for their pair neutron coefficients closer to the median seemingly demonstrate greater degrees of ordering or clustering (i.e. higher or lower α values). This trend was also observed in the analysis of the CrCoNi alloy: Cr-Cr and Ni-Ni pairs in both cases demonstrate the smallest α values above or below zero.

It is possible that the manner in which the RMC algorithm weights its partial PDFs by neutron coefficients is having an impact on the form of ordering; it is equally possible that this demonstrates a commonality in the ordering between alloys of similar composition, or that contain similar constituent elements. Given that prior analysis of the impact of neutron coefficients on the quality of fitting was inconclusive - appearing potentially system specific, or entirely without trend - there is a higher likelihood that the above Warren-Cowley parameters further demonstrate the similarities in structure between the ternary CrCoNi and quaternary CrFeCoNi, with Cr atoms preferentially distributing themselves into 'square' configurations to satisfy the magnetic frustrations previously raised. Further work would be required in this regard, however, with alloys of similar but distinct compositions - such as VCrCoNi, CoNiCuPd and so on - to assess the validity of this conclusion.

4.4 Conclusions

In summary, the ordering of the CrFeCoNi quaternary alloy is demonstrated and well-described through Reverse Monte-Carlo fitting of the neutron PDF. Extension of the Clapp configurational analysis method to higher-order systems - i.e. those of greater than three constituent atomic species - appears robust, with agreement across a number of fitting regimes to suggest the success of the result.

At all temperatures, between room temperature (approx. 300 K) and 1273 K, CrFeCoNi appears to demonstrate the segregation of Cr and Fe atoms to the corners of the unit cell in an $L1_2$-type structure. The segregation of Cr and Fe atoms into the C16 configuration appears to be spatially un-connected, whereby Cr-rich unit cells form alongside but distinct from Fe-rich unit cells, as evidenced by the relative lack of enhancement to the Cr-Fe:Co-Ni pseudo-binary. The remaining constituent elements demonstrate little by way of preferential ordering, with both Ni and Co atoms distributing themselves randomly across available lattice sites. This result is supported by both Clapp configurational analyses and the calculation of the more traditional pairwise Warren-Cowley parameters. It may be assumed that the preferential ordering of Cr and Fe atoms necessitates an associated migration of Ni and Co atoms to the faces of the unit cell, though the distribution of these atoms across face-sites appears random.

These results align strongly with existing studies on the form of SRO in CrFeCoNi. It is near-uniformly agreed in the literature that the formation of an $L1_2$ structure with Cr atoms at the corners of the unit cell is the likeliest form of ordering in the system. The suggestion that this is driven by the anti-ferromagnetic properties of Cr may be supported by this particular result, though this is beyond the scope of the present work and would require further investigation. Further, the suggestion by Schönfeld *et al.* that an order-disorder transition is predicted to exist above 500-600 K in equiatomic CrFeCoNi is entirely unsupported by the findings of this investigation.

The efficacy of the RMC method for the analysis of complex structures appears to be confirmed by this study, though questions remain. The application of Clapp configurational analysis to higher-order systems has proven a success - even with the added compositional complexity - with regards to the pseudo-binary analysis method. Indeed, even the existence of double minima in the χ^2 analysis of the initial 40Å fitting range - which suggests the potential for multiple equivalently successful solutions to the fitting - appears to show a consistent configurational result that can provide confidence in the determined structure. The application of this method to systems of greater compositional complexity - i.e. systems of five or more constituent elements - may yet, however, prove more complex. Indeed, the challenges of 'recombining' 10 or more pseudo-binaries in a quinary alloy into a single coherent picture of ordering could prove prohibitively difficult for systems with complex or non-intuitive structures.

Furthermore, the general trends observed across both the CrCoNi and CrFeCoNi alloy likely point towards similarities in the ordering behaviours of alloys with similar elemental compositions, but this will require further analytical work to definitively demonstrate.

Chapter 5

A Novel Analytical Framework for the Analysis of Atomic Short-Range Ordering

5.1 Introduction

The preceding chapters of this work have provided evidence for the utility of the 'Clapp method' in the quantification and interpretation of short-range order in MPEAs. Though Warren-Cowley parameters have been adopted by the wider community as a default descriptor for local ordering behaviours, they reduce complex three-dimensional crystallographic information into single-dimensional values, thereby limiting the information that can be extracted from a given system. Clapp configuration labelling has provided an intuitive framework to begin addressing this shortcoming in cubic systems.

As a reminder, Clapp [38] established a method for the description of atomic configurations in binary FCC and BCC crystal structures by numerically labelling the positions of nearest-neighbour atoms relative to a central site (i.e. atoms present within the first coordination shell of a given atomic position). In a binary system, atoms on each nearest-neighbour site are of either a 'like' or 'dislike' species to the central site atom. Mathematically, therefore, there are 2^N possible atomic configurations for a given binary alloy system, where N is the total number of nearest-neighbour atoms. This number is reduced by the consideration of symmetrically-equivalent structures: FCC structures ultimately possess 144 unique configurations by symmetry; BCC structures possess 22.

Importantly, Clapp provided a series of ordering rules for these symmetrically equivalent configurations, providing the numerical labelling implemented in prior chapters. These numbering rules for the FCC case are as follows:

1. Configurations are initially ordered by composition, i.e. the total number of dislike nearest-neighbour atoms relative to the central atom. Configurations containing the fewest dislike nearest-neighbour atoms are given the lowest numerical value.
2. Configurations are then sub-ordered by the number of dislike nearest-neighbours in each coordination shell:
   (a) The configuration with the **highest** number of dislike atoms in the **first** nearest-neighbour coordination shell (i.e. not including the central atom) is labelled first.
   (b) If two configurations have an equal number of dislike nearest-neighbours in the first coordination shell, then the configuration with the **lowest** number of dislike atoms in the **second** nearest-neighbour coordination shell is labelled first.
   (c) This system then alternates out to the maximum coordination shell captured in the configuration.
3. In the event that the above rules still do not distinguish between unique configurations, they are then sub-ordered *again* in descending order of multiplicity, i.e. the configuration with the greatest number of symmetrically equivalent configurations is labelled first.

These ordering rules are not intuitively described in the original work, and therefore a selection of configurations from the FCC system may be found in Table 5.1, to highlight the validity of this description.'Negative' configurations are also defined, such that configurations with more than half of their nearest-neighbour positions occupied by dislike atoms are taken to be negative. As these configurations are essentially 'inverted' versions of existing 'positive' configurations (Figure 5.1), they are labelled accordingly. The prevalence of Clapp configurations in a given model can then be quantified through the calculation of statistical enhancement factors. By extension, related enhanced configurations - i.e. those that differ in structure by one or two atoms from one another - can be associated through the 'ordering pathways' described previously, and used to provide a full description of ordering across otherwise seemingly randomly distributed structures.

While Clapp's method is efficient and well-described for FCC and BCC structures, a fully realised and generalised system of configurational analysis is not provided in the original work. HCP structures, for instance - common crystal structures in alloying metallurgy - are left without the same labelling treatment, though the methodology for applying these configurational and ordering rules to more complex structures remains valid. The following work therefore presents a novel analytical framework - and associated software - for the application of the Clapp method to all

FCC Clapp Configurations (15-31)						
Clapp Configuration	No. dislike nearest neighbours					Multiplicity, W_k
	Total	1^{st} coordination shell	2^{nd} coordination shell	3^{rd} coordination shell	4^{th} coordination shell	
15	3	6	6	12	3	8
16	4	16	0	16	0	3
17	4	16	4	8	4	6
18	4	14	4	12	2	48
19	4	14	6	8	4	48
20	4	12	4	14	2	48
21	4	12	4	12	4	24
22	4	12	4	12	4	12
23	4	12	6	12	2	24
24	4	12	6	12	2	24
25	4	12	6	10	4	48
26	4	12	8	12	0	12
27	4	12	8	10	2	24
28	4	12	8	10	2	24
29	4	10	8	12	2	24
30	4	10	8	12	2	24
31	4	10	6	12	4	48

Table 5.1: A table demonstrating the labelling system employed by Clapp, highlighting the alternating ascending and descending pattern applied to the occupation of coordination shells for an FCC system.

crystalline materials. In the first instance, this work will establish an updated set of ordering rules for the generalised framework, providing guidance on the labelling of atomic configurations. Subsequently, the assumptions inherent to the model - specifically, a full mathematical description of the simplified point group symmetry considerations - are presented, using a case example of an $L1_0$ structure for clarity.

A method for the calculation of configurational enhancements in large-box models is then presented in the following section. Case examples from a broad range of crystal systems - including a number of non-metallic systems - are provided in Section 5.5, as a full illustration of the generalisation and capabilities of the analytical framework. A link to the produced software is provided in Appendix A.2.

5.2 Analytical Framework

A programme has been developed to facilitate the application of the above generalised framework to all crystal systems. Using the standardised Crystallographic Information File (.cif) format as an input, users are able to generate Clapp-style configurational dictionaries for the sublattices of a given structure, with a further option to select site-equivalencies across lattices for broader analysis.

Using the symmetry operations, atomic sites and associated atomic species listed in the .cif file, a crystal super-lattice is generated, and sub-divided into its constituent sublattices according to the specified requirements of the user. The nearest neighbour atoms for these sub-lattices are then identified individually, and presented in lattice vector form in a 'basis set' file.

5.2.1 Structuring .cif Files

One of the key inputs required for the use of this analytical framework is the .cif file, a 'Crystallographic Information File' used to fully describe a given structure. The .cif file format was originally formulated in an effort to standardise the documentation of crystallographic information, alongside key experimental values or parameters. Typically, these files will include atomic unit cell coordinates (with associated site fractions and thermal parameters), symmetry operators, and space groups. In practice, however, the generation of .cif files for complex crystal structures is

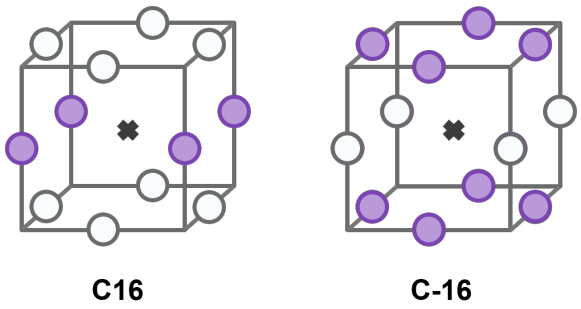

Figure 5.1: A demonstration of the opposite binary occupations for configurations and their negative counterparts.

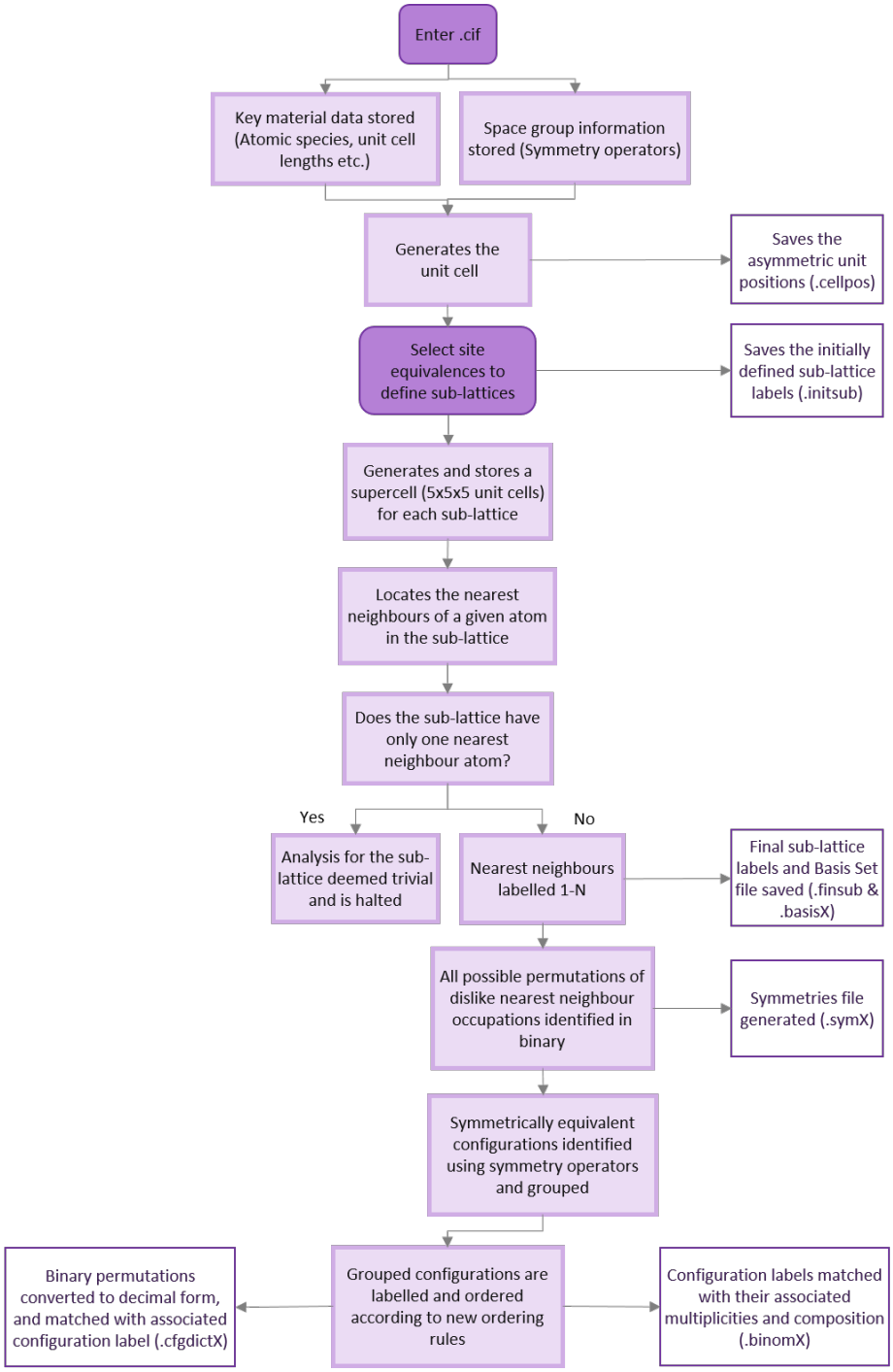

Figure 5.2: A flow chart demonstrating the stages of generating configurational dictionary files for the new analytical framework.

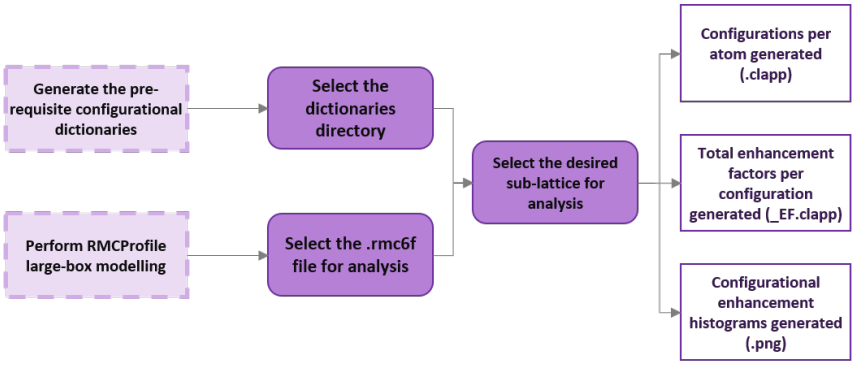

Figure 5.3: A flow chart demonstrating the analysis of large-box models produced by RMCProfile using the dictionary files generated by the new analytical method.

often imperfect, or non-standard: a user may, for instance, incorrectly define asymmetric unit cell coordinates; different databases or collections of .cif files will possess slight variations in the syntax or presentation of data.

In many ways, the software produced for the above analytical framework will operate regardless as to the syntax of the provided files, with information lifted from the .cif file with relative ease. However, a number of pre-requisite conditions exist for the formatting of the .cif file to successfully generate configurational dictionaries used in later analysis. In the first instance, the files used to generate the configurational dictionaries for each structure must necessarily contain lattice positions for all constituent atoms used during RMCProfile fitting. In other words: the atom types contained in the .cif file must match those in the .rmc6f file of interest, due to sublattice labelling conventions in the code base. In practice, this means that a set of files generated for one FCC structure cannot be used on another FCC structure by default. Though the key .binom and .cfgdict files generated will be identical for equivalent space groups (and therefore theoretically transferable), the remaining files will be composition and sub-lattice specific, and will therefore raise an exception when used on a different system.

The .cif file must also necessarily contain a full list of the symmetry operators used to describe the crystal structure, in a standard 'x, y, z' format. As may be anticipated, a full list of unit cell lengths (in Å) and unit cell angles is also required, for the calculation of nearest-neighbour distances and the generation of the 'basis set' of nearest-neighbour vector positions. The order in which these values and operators are entered into the .cif file is not relevant to the generation of configurational dictionaries.

5.3 Assumptions in the Method

In generalising the Clapp method, there are a number of mathematical assumptions or considerations that require attention,

5.3.1 Symmetry Operations

Each crystal structure possesses a unique associated set of symmetry operations that can be used to describe its space group. It might be assumed, therefore, that in the grouping of Clapp-style configurations, *all* symmetry operations must be applied to a given set of nearest neighbour atoms in order to fully identify all equivalent atomic configurations. It may be demonstrated mathematically, however, that for each basis set (the lattice vector coordinates of the nearest neighbours for a given sub-lattice) it is only necessary to apply operations that leave the position of an atom at the sub-lattice origin *invariant* under symmetry.

We can make this simplification due to the existence of point group symmetries that describe the local environment of a given point, or atom. A point group is a geometric construct that defines a set of symmetry operations with a common fixed point in space. When applying a symmetry operation to a given configuration of atoms , it is necessarily required that the total transformation of the local environment maps the original nearest neighbour atoms on to positions with the same basis set coordinates. Symmetry operations that require a translation of the origin - that is, the atom around which we locate the nearest neighbours - cannot satisfy this condition; these operations are a valid part of the total *space group* of the crystal structure, but do not adequately describe the *point group* of this particular site. We can therefore discard operations that do not maintain the position of this origin.

More plainly, if a given sub-lattice is defined by an atom of species 'A' at position [0, 0.5, 0.5], then the only symmetry operations required to define all possible configurations of nearest-neighbour atoms are those that leave this atom in position [0, 0.5, 0.5]. This is because - by definition - symmetry operations that pass through a given origin will maintain the position of this origin; those that do not will necessarily translate the position of the origin in space.

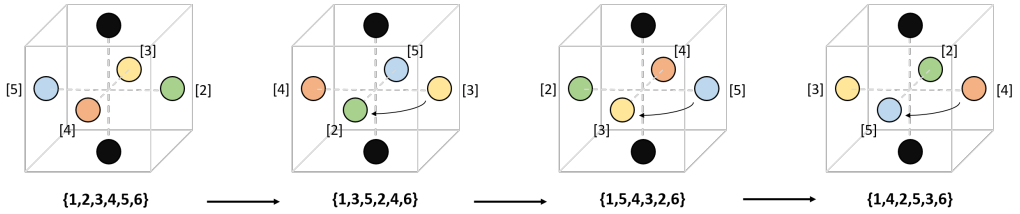

Figure 5.4: A graphical representation of an applied four-fold series of 90° rotations about the y-axis, demonstrating the manner in which the labelled atomic positions alternate. This is integral to later interpretation of dislike nearest neighbour occupations.

Though in certain cases a translational shift is present in the complete symmetry operation, operations that leave the sublattice origin position invariant are reliant only on the rotational or reflective components of said operation. The translational component may therefore be effectively ignored when determining the possible configurations of atoms in the first coordination shell.

This is not a complete picture, however, as origin atoms located on special equivalent positions within the crystal lattice require further treatment. In the following framework, special equivalent positions are identified and made essentially equivalent to the origin of the entire structure outlined by the original .cif file. A 'check' may be performed by determining whether an applied symmetry operation transforms the origin of a given sub-lattice back into itself *or* into a point translated by one unit vector in each direction. This may be visualised as a mirror plane coinciding with a point half a unit vector in each direction along the unit cell vector direction.

Once the relevant symmetry operators for each sublattice have been identified, they are applied in turn to the basis set, establishing every possible configuration of nearest-neighbour atoms. The primitive structure, for instance, possesses a four-fold rotational symmetry about the y-axis. The four rotations about the y-axis would swap the numbered atomic positions such that each of the $\{1,3,5,2,4,6\}$, $\{1,4,2,5,3,6\}$, $\{1,5,4,3,2,6\}$ arrangements would describe a single 90° rotation of the $\{1,2,3,4,5,6\}$ configuration (Figure 5.4). These arrangements are then stored for each sublattice in a 'Symmetries' text file (.sym), for later reference.

5.4 Ordering Rules

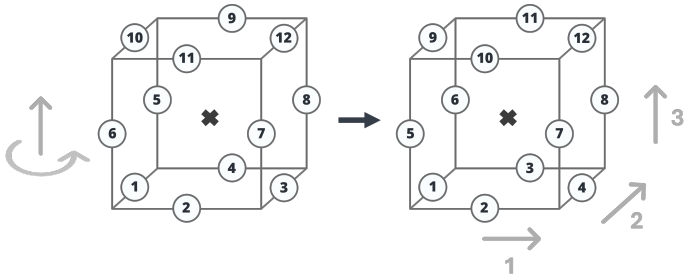

Figure 5.5: A comparison of Clapp's atomic labelling convention (Left) and that of the new framework (Right).

Clapp's method, as outlined above, is a useful starting point for the description of crystalline materials, but that does not mean that it is entirely without its difficulties. In particular, Clapp's treatment of FCC and BCC structures differs minutely, but in such a way as to make generalisation of the method less straightforward. In the original work, the 144 configurations of the FCC nearest-neighbour positions are outlined first, with associated labelling conventions developed based on the number of unique inter-atomic distances in the FCC unit cell. More specifically, this refers to rule 2 outlined in the introductory section: the alternation of ascending or descending ordering based on the number of dislike nearest neighbour atoms per coordination shell. Clapp's original method, naturally, labels configurations according to the first nearest neighbours of a given atom and the binary occupations of those positions. These labelling conventions, however, also inherently contained information on higher neighbouring distances and coordination shells. As a way to distinguish between those with increased numbers of dislike nearest neighbours - which naturally have greater multiplicities - Clapp ordered symmetrically equivalent configurations by occupations in higher order coordination shells. All evenly numbered coordination shells (i.e. the second, fourth, and so on) are ordered in *ascending* numbers of dislike nearest-neighbour atoms; all odd coordination shells (i.e. the first, third, etc.) are ordered in *descending* occupation of dislike atoms.

In applying these conventions to a BCC structure, however, Clapp does not simply use an equivalent general rule. One might expect that the first coordination shell would be equivalently ordered according to descending dislike occupation, the second ascending, and so forth. Instead, the Clapp labels are applied according to *absolute distance* in terms of the FCC unit cell parameter 'a'.

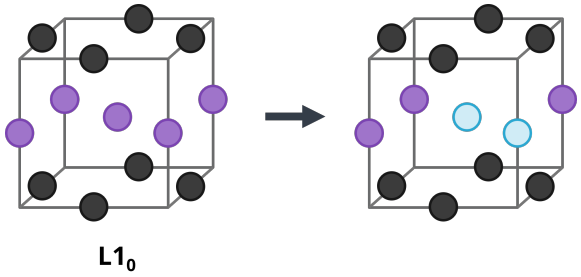

Figure 5.6: The binary $L1_0$ structure, possessing A and B sub-lattices (Left), and an example of substitution on to a single sublattice by a third constituent atom type (Right).

This logic therefore leads Clapp to label what would otherwise be the first coordination-shell of the BCC system as the '*second*' coordination shell, followed subsequently by the 'third' and 'fifth' shells. The application of ascending and descending logic is maintained: the 'second' coordination shell is labelled in ascending order of dislike nearest-neighbour occupation; the 'third' and 'fifth', as odd-numbered shells, are labelled in descending order. [1]

This labelling convention makes the generalisation of the method less straightforward. For non-cubic systems, in which nearest-neighbour atoms do not occupy positions at equivalent distances to the FCC and BCC structures, this particular labelling method may even prove impossible to enforce The following framework addresses this concern by removing this consideration entirely; odd-numbered coordination shells are labelled in descending order of dislike occupation, and even-numbered coordination shells in ascending order. As might be expected, for the previously defined FCC and BCC structures, this has some impact on the final numbering of configurations - particularly those with a larger number of dislike nearest-neighbour atoms in the configuration overall.

Equally, Clapp opts to number the nearest-neighbour atomic positions in a particular fashion, which will have an equivalent impact on the labelling system employed by the generalised framework. In his original outline, Clapp chooses to number the nearest neighbours from 1-N from the lowest position to the highest, rotating anti-clockwise to accommodate atoms on the same face or plane. This represents the 'basis set' of atomic positions - that is, the coordinates of the nearest neighbours in terms of the individual lattice vectors that constitute the basis of the crystal structure. This method has been simplified mathematically for the present framework: atoms are numbered according to increasing z-coordinate value, followed by the y- and x-coordinate values in sequence. A diagram highlighting the differences between the two methods is presented in Fig. 5.5 Given the reliance of

[1] It is equally worth noting that, in Clapp's original work, this logic is somewhat confusingly applied. There appears to be an inconsistency in the application of 'absolute distances' that leads to an incorrect assignment of ascending or descending conventions for occupied coordination shells. Though this does not render Clapp's labelling system itself incorrect, it is another justification for the redevelopment of these ordering rules in the following work.

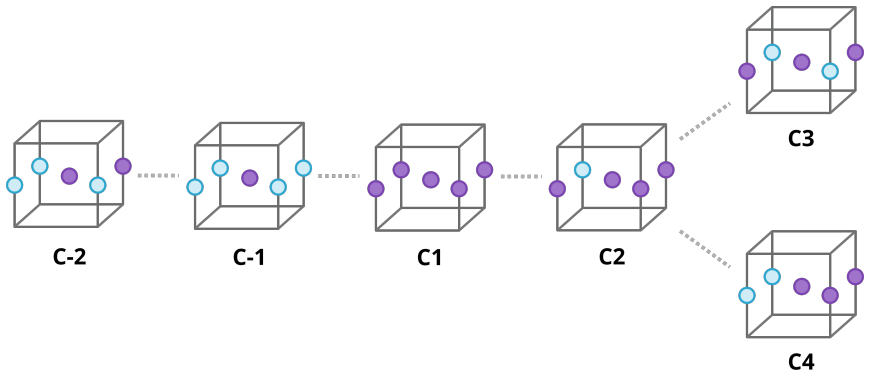

Figure 5.7: The enumerated configurations for a single sub-lattice of the $L1_0$ system.

the Clapp method on the specific location of occupied positions, this will therefore introduce further differences between Clapp's original configurational labelling and the new analytical framework. While this will inevitably create a disparity between existing studies that make use of the Clapp method and future studies using the generalised method, this is easily resolved through reference to the basis set of atomic positions. All configurations can be reconstructed from said basis set, allowing for comparison across studies that do not use an equivalent labelling system.

To demonstrate this principle visually, the configurations for ordering on a sub-lattice of the $L1_0$ structure (Figure 5.6) are presented in Figure 5.7. As the sublattice is simply a plane of atoms, each lattice point will possess four nearest neighbours. A central atom of type 'A' surrounded by entirely like atoms is given the C1 configuration; when surrounded by entirely dislike atoms, it is the C-1 configuration. As the occupation of nearest neighbour atoms increases, the labelling increases. When the number of dislike nearest neighbours increases to three, the configuration is a compositionally 'mirrored' form of the C2 configuration, and it is therefore labelled C-2. The C3 and C4 configurations are then distinguished by their multiplicities: as the C4 configuration has a greater multiplicity, it is labelled last.

5.4.1 Statistical Analysis of Atomic Configurations

The quantification and analysis of the enhancement of specific atomic configurations in a large-box model inherently requires statistical treatment. In the case of a binary alloy, this is a comparatively trivial problem. In their 2017 work, Owen *et al* demonstrated that the enhancement of a given configuration relative to a random distribution of atomic arrangements is given by:

$$\beta_a = \frac{n_a - \bar{n}_a}{\sigma_{n_a}} \tag{5.1}$$

where β_a is the calculated statistical 'enhancement factor' of a given configuration; n_a is the number of times the configuration appears in a particular structure; $\bar{n}_a$ is the *expected* number of instances of the configuration; and σ_{n_a} is the standard deviation, as predicted from a randomly distributed example case. A configuration is taken to be statistically enhanced when $|\beta_a| > 3$, representing an enhancement of more than three standard deviations from the mean, or expected value. Plotting the enhancements of specific configurations in histogram form also allows for the rapid identification of degradation pathways: groups of enhanced configurational motifs that are closely related to one another (differing by the presence or absence of individual atoms), related to a particular preferential ordering behaviour.

Increasing chemical complexity introduces an equivalent increase in the complexity of statistical analysis, and a significant parallel increase in any computational requirements therein. Taking an FCC crystal as an example, a binary system would possess 4096 (2^N=2^{12}) possible configurations of like and dislike atomic pairs. A ternary system would possess over 500,000 possible configurations, and a quaternary system increases this complexity by an order of magnitude. Statistically, therefore, the usefulness of identifying the enhancement of unique configurations in a system of greater chemical complexity is minimal; the majority of computationally determined structures are unlikely to be of sufficient size to adequately capture the possible range of local configurations in statistically significant quantities.

For this reason, chemically complex systems are 'reduced' into pseudo-binary models to assess configurational enhancement. Each atomic species is taken in turn, and *all* dislike atoms taken to be of a single, dislike species. Given the prior separation of the superlattice into its constituent sub-lattices, this allows for direct analysis of the chemical occupancy of specific lattice sites, and the local ordering motifs of individual atomic species.

5.5 Test Cases

In order to demonstrate the full breadth of analyses made possible by the above framework, a number of test cases have been produced across a range of crystal structures of interest.

5.5.1 Ordering Transitions in Heusler Alloys

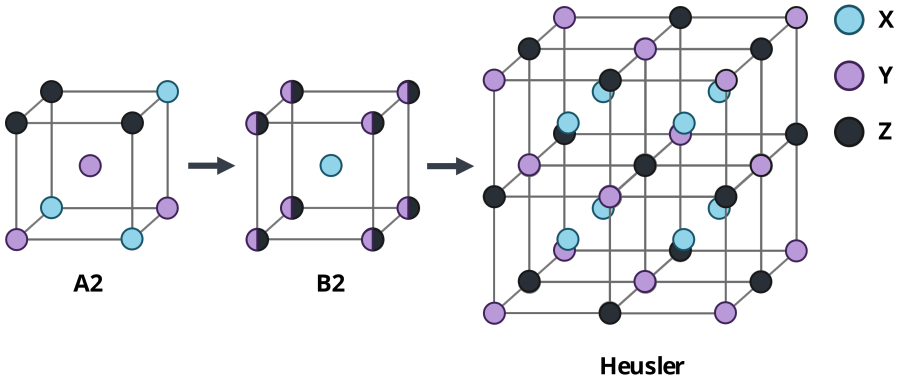

Figure 5.8: A diagram illustrating the pathway for the A2-B2-Heusler ordering transition in a ternary alloy system, as in the case of Fe_2VAl.

Heusler alloys are a well-known and widely studied group of intermetallic materials, often hailed for their ferromagnetic properties, amongst other unique mechanical behaviours [76]. Both full-Heusler (X_2YZ) and half-Heusler (XYZ) alloys have been studied since the turn of the 20th century, though a significant resurgence of interest in the 1980s led to their reappraisal as candidates for applications in the field of spintronics [77]. The full-Heusler phase takes the form of an ordered $L2_1$ face-centred cubic structure with two sub-lattices: one containing a single atomic species, and the other with an alternating 'patterning' of the remaining atom types. It can otherwise be described as a 2×2×2 'array' of body-centred unit cells, with a single atom-type at the body-centre, and an alternating occupation of atoms at the unit cell corners. A diagram of the $L2_1$ structure may be found in Figure 5.8.

An interesting case example of a full-Heusler material demonstrating a significant ordering transition was outlined by Maier *et al.* in their *ab initio* DFT work on the Fe_2VAl ternary alloy [78]. At room temperature, Fe_2VAl presents in the stable $L2_1$ Heusler structure; when its temperature is raised to $\tilde{1}350$ K, however, the structure decomposes into a body-centred B2 phase, before finally forming a disordered BCC A2 phase at approximately 1460 K. The full phase ordering transition is also presented in Figure 5.8.

The A2 Structure

Using the Clapp framework outlined above, we are able to demonstrate the ordering transitions of the Fe_2VAl ternary. In the first instance, we are able to visualise the randomness of the A2 structure through the generation of configurational dictionaries using only the BCC structure, for which all configurations will possess eight nearest-neighbour atoms. In all cases, theoretical .rmc6f large-box files were generated using .cif files obtained on the Inorganic Crystal Structure Database (ICSD). Use of configurational dictionaries generated without site equivalencies on a model of the A2 system - that is, a BCC model with entirely random distribution of Fe, V, and Al atoms - demonstrates no statistical enhancement above three standard deviations for any configuration of atoms (Figure 5.9(a)).

The B2 Structure

In the second instance, a long-range ordered B2 BCC lattice is generated, with Fe atoms placed at the body-centre of the unit cell, and the V and Al atoms distributed randomly across the remaining lattice sites. Use of the random A2 dictionaries on this model produces distinct statistical enhancement across all pseudo-binaries (and thereby for each constituent atom). The Fe:Ψ pseudo-binary - grouping both V and Al atoms into a single atom type - is shown to possess only the C-1 configuration, surrounded by entirely dislike nearest neighbour atoms. Both the V:Ψ and Al:Ψ pseudo-binaries, however, show enhancement to both the C1 and C-1 configurations, indicating a preference for entirely like or entirely dislike nearest-neighbour bonding. This is due to the sub-grouping of atom types: if Fe and V atoms are taken to be a single atom type, then only entirely like or entirely dislike nearest neighbour bonds are made possible (Figure 5.9(b)). Using the ordered B2 dictionaries to assess the B2 structure, however, we find that there is a random occupation of *all* configurations, as might be expected (Figure 5.10(a)).

There are also minor, observable enhancements to higher configurations. Taking the Al:Ψ pseudo-binary as an example, the C-1 enhancement is brought about the Al atoms surrounded entirely by Fe atoms; the C1 enhancement is brought about by the V atoms surrounded by Fe atoms, which in this instance have been grouped and are therefore 'like'. The remaining configurations are then brought about by the nearest neighbours of the Fe atoms themselves: if half of the atoms are Al atoms, and half V atoms, then we would expect to see statistical enhancements to configurations in which four of the nearest neighbour positions are like atoms, and four are dislike - which includes a number of the higher configurations here, such as the C9 and C10.

The Heusler $L2_1$ structure

Finally, a long-range ordered $L2_1$ Heusler lattice is generated, such that the 'X_2' sub-lattice is occupied entirely by Fe atoms, and the remaining sub-lattices are composed of V and Al atoms occupying alternating lattice positions. Using the A2 configurational dictionaries for this model, we

find a large statistical enhancement to the C9 configuration in both the V and Al pseudo-binaries, and small, associated enhancements to the C1 and C-1 configurations. The C9 configuration (Figure 5.9(c)) clearly demonstrates the alternating occupation of V and Al atoms on their sub-lattice. The Fe:Ψ pseudo-binary, however, shows only enhancement to the C-1 configuration - entirely dislike nearest neighbour bonding - as would be expected. The configurations listed here, corresponding to analysis with the A2 dictionaries, can be found in Figure 5.10.

We may also perform an analysis of the $L2_1$ ordered Heusler using dictionaries generated from the B2 structure. The framework outlined above allows for the separation of constituent sub-lattices, allowing configurational analyses on each individually. With the B2 structure as a basis, the Fe sub-lattice of the Fe_2VAl requires no further treatment: a single atom-type will possess no configurational enhancements on its sub-lattice. However, the V and Al sub-lattice - in the absence of Fe atoms - effectively forms a primitive structure with alternating V and Al occupation. This primitive lattice possesses six nearest-neighbours, as opposed to the eight of the BCC lattice, and configurational analysis on this sub-lattice yields enhancement to the C-1 configuration, reflecting the alternating occupation (Figure 5.11).

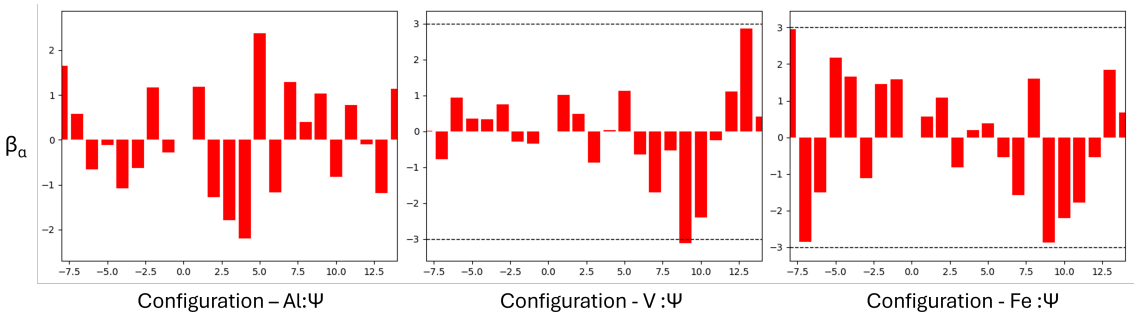

((a)) The A2 phase. Within statistical bounds all configurations appear to be randomly distributed.

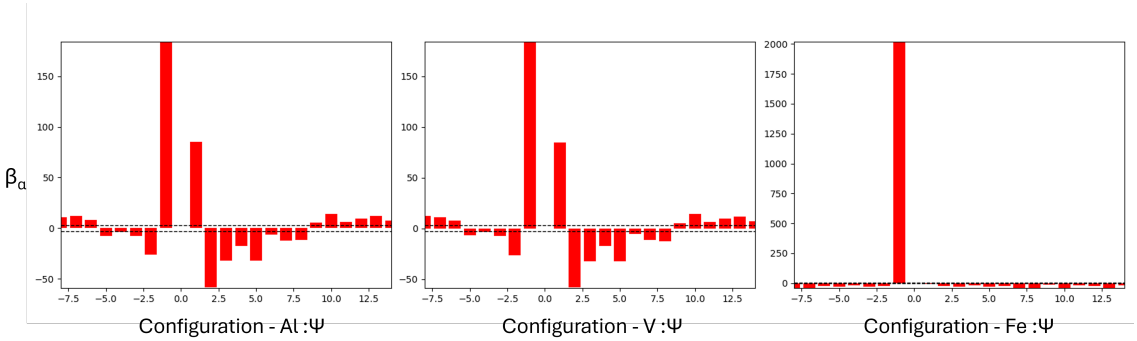

((b)) The B2 phase. Note the large enhancement of the C-1 phase in the Fe:Ψ pseudo-binary, indicating the segregation of Fe atoms to the body-centre.

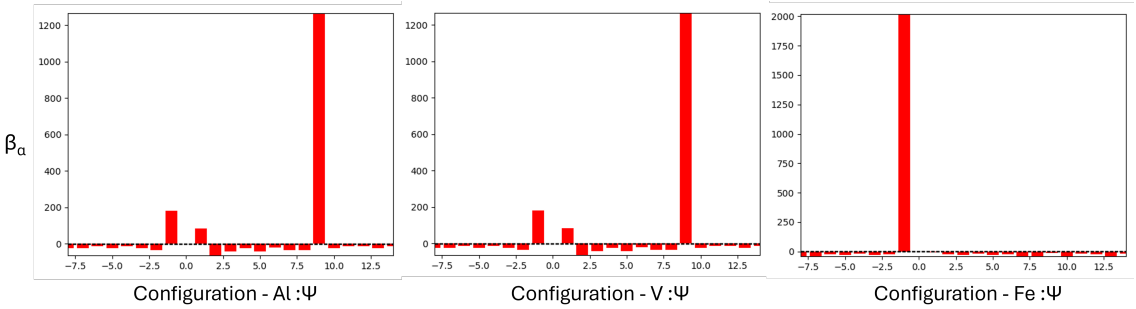

((c)) The Heusler phase. Note the large enhancement to the C9 configuration, demonstrating the alternation of Al and V atoms in the newfound ordered structure.

Figure 5.9: Enhanced configurations per pseudo-binary for the Fe_2VAl system, as it undergoes transition from the A2 phase to the fully ordered Heusler phase, using the configurational dictionaries generated by the A2 structure.

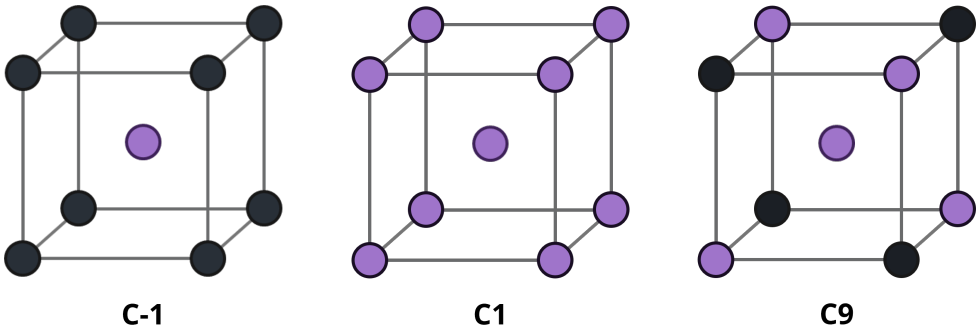

Figure 5.10: The major enhanced configurations of the Heusler system as produced by the A2 dictionaries (i.e. demonstrating a BCC-type structure.

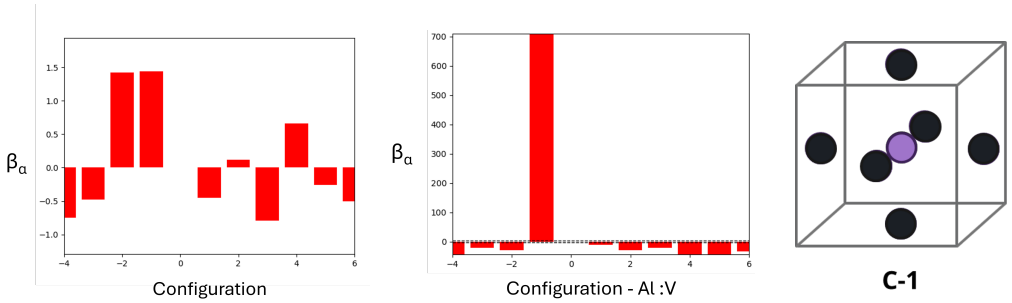

((a)) B2 Phase

((b)) The Heusler Phase

((c)) Primitive C-1 Configuration

Figure 5.11: Enhanced configurations for both the B2 and Heusler phases of the Fe_2VAl system, using the configurational dictionaries generated by the B2 structure. The B2 possesses two sub-lattices - one for the Fe atoms, and one for the Al and V atoms. Configurational analysis for single-atom sub-lattices is trivial; the Al:V sub-lattice pseudo-binary therefore contains all of the relevant information for this system.

5.5.2 Cubic and Orthorhombic Perovskite Ordering

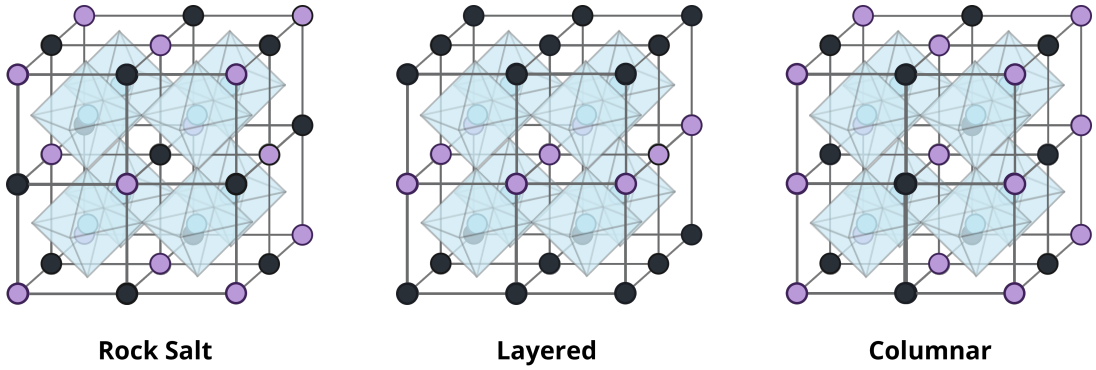

Figure 5.12: The three most common ordered-perovskite structures; ordering is presented on the A-site, though both A- and B- site ordering is possible.

Perovskites are a key group of complex oxide crystal structures, and are regularly exploited for their enhanced ferro- and piezo-electric properties in electronic applications [79]. In their ideal form, they adopt the ABX_3 structure, whereby X anions octahedrally coordinate B-site cations. These mechanical and physical properties are often substantially altered by the crystal structure of the materials; distortions brought about by octahedral tilting, for instance, can have a significant effect on the overall behaviour of the system by impacting conduction bandwidths and magnetic interactions. Such tilting is typically brought about by the chemical occupation of A-site and B-site cations - though atomic substitution is possible across both anion and cation sites - forming key, common structural motifs across perovskite materials.

Three of the most common simple perovskite structures are the rock-salt, layered, and columnar perovskites, which order on the A and B cation sites. The three structures are visualised in Figure 5.12 for A-site ordering. To demonstrate the efficacy of the above framework, a cubic perovskite structure of $15\times15\times15$ unit cells was constructed, containing 42,750 atoms in total. For the purposes of this model, a calcium titanate ($CaTiO_3$) structure was generated, with Ca and Ti atoms randomly distributed across the A and B lattice sites in equal proportion.

In generating the ordered perovskite structures, the Ca and Ti atoms were distributed across the metallic lattice sites, such that Ca atoms occupy the A-sites and Ti atoms occupy the B-sites. The remaining O atoms are excluded from configurational analysis. Ordering may be introduced to any sub-lattice, and analysed in isolation. In the case of the rock-salt structure, an extra atomic species of arbitrary type 'X' was introduced to the B-site Ti lattice. Ti and X atoms were distributed evenly, such that there are approximately 1675 atoms of each across the B-site positions. The six nearest-neighbours on the B-site sub-lattice form a primitive structure. As is evident in Figure

5.13(a), the rock salt structure leads to strong enhancement in the C-1 configuration, with atoms surrounded entirely by dislike nearest neighbour atoms.

The same process may be employed with the columnar and layered structures on the *A*-sites: Ca atoms are paired with an arbitrary atomic species of type 'X', and alternating layers or columns of *A* site atoms are generated in equal quantities (approximately 1680 atoms for each atomic species). The configurational enhancements for these structures are presented in Figure 5.13(b). As is apparent, the layered structure shows strong enhancement to the primitive C3 configuration, while the columnar structure shows enhancement to the primitive C-3 configuration. These configurations are presented in Figure 5.13(c). By extension, ordering on *both* *A*- and *B*-sites can be analysed in isolation from one another, with the option remaining to combine both sites via site equivalency.

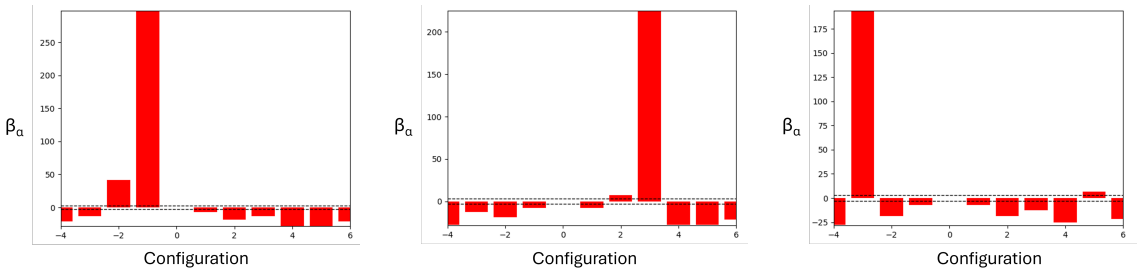

((a)) Rock Salt ((b)) Layered ((c)) Columnar

Figure 5.13: Enhanced configurations for the ordered Perovskite structures.

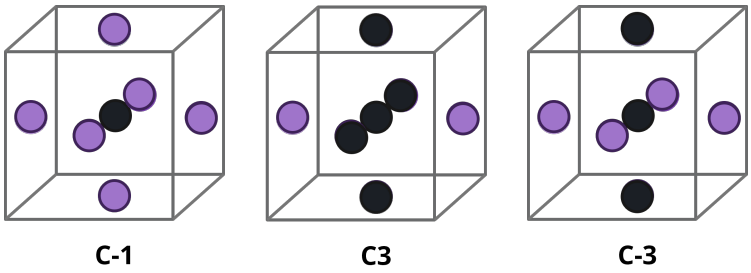

Figure 5.14: The major enhanced configurations for the rock salt (C-1), layered (C3), and columnar (C-3) perovskite structures, from right to left.

5.5.3 Ordering in Doped Ceria

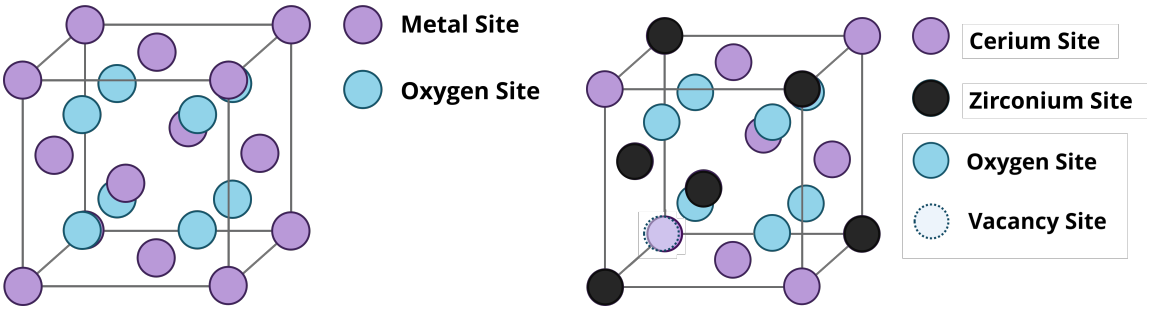

((a)) Cerium zirconium oxide structure

((b)) A fraction of the pyrochlore unit cell

Figure 5.15: The modelled structures of cerium zirconium oxide, with associated labelling for atomic occupations

Cerium oxides are naturally occurring compounds widely studied for their oxygen storage capabilities, and the application of these properties to catalysis [80]. Cerium zirconium oxides ($Ce_{1-x}Zr_xO_2$) are a mixed-oxide branch of these materials commonly used in the manufacture of catalytic converter components, comprising a solid soluton of ceria (CeO_2) and zirconia (ZrO_2) [81]. The concentration of Ce and Zr relative to one another in a given oxide influences the structure of the material considerably: Ce-rich compositions adopt a cubic structure; Zr-rich compositions are capable of forming both tetragonal and monoclinic phases.

In the simple Ce-rich case, the cerium zirconium oxide presents as a cubic lattice in the fluorite structure; cerium and zirconium cations effectively form an $Fm\bar{3}m$ FCC-type structure, with oxygen atoms occupying the interstitial sites (Figure 5.15(a)). The methodology outlined above allows for the analysis of configurational enhancements on the cation sub-lattice by ignoring the presence of the oxygen sub-lattice. Generating a 10×10×10 supercell (12,000 atoms: 8000 O atoms; 1984 Zr atoms; 2016 Ce atoms), we can select a site-equivalency for the cation sub-lattice and generate an FCC dictionary of atomic configurations.

For a random distribution of atoms across the sublattice, we find no particular configurational enhancement, as demonstrated in Figure 5.16(a). We may, however, demonstrate the formation of a pyrochlore structure on the same sub-lattice. Pyrochlore structures may be thought of as an ordered derivative of the fluorite structure, in the $Fd\bar{3}m$ space group. Where the Fluorite structure possesses disordered, highly mobile vacancies - leading to strong ionic conductivity - the pyrochlore structure necessarily introduces order to the oxygen-vacancy sub-lattice, effectively reducing the vacancy mobility by increasing the activation energy of diffusion. A visualisation of the structure is provided in Figure 5.15(b).

Configurational analysis of the Ce-Zr sub-lattice shows strong enhancement to the C82 structure (Figure 5.16(b)), clearly demonstrating the alternation of chemical occupancy.

Additionally, the framework is capable of demonstrating vacancy ordering behaviours in large box models using this method. The substitution of vacancies on to the oxygen sub-lattice of doped ceria structures can have a significant effect on material properties, including the improvement of ionic conductivity required for catalysis. Treating vacancies as unique 'atom types' ('Va') in both the large-box .rmc6f file produced by RMCProfile and the .cif file used to generate the structure allows for the selection of equivalent positions on the oxygen sites. The following arbitrary example of pyrochlore vacancy ordering demonstrates the formation of planar or columnar vacancy structures in the cerium zirconium oxide described above, with particular enhancements to the C3 configuration on a primitive oxygen sub-lattice (Figure 5.16(c)).

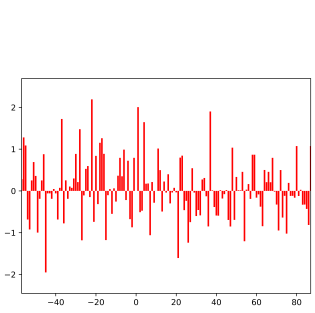

((a)) Randomly distributed

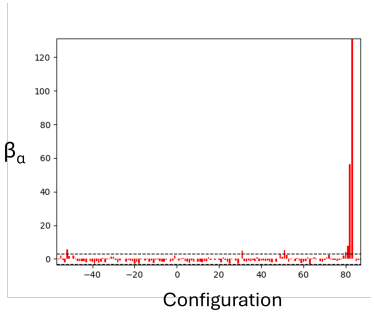

((b)) Ordered Ce and Zr atoms

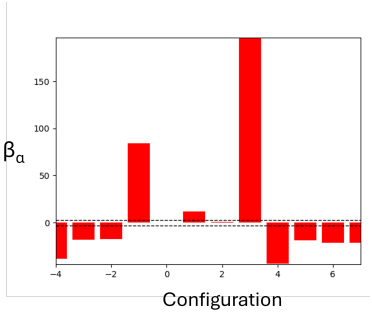

((c)) Sub-lattice with vacancies

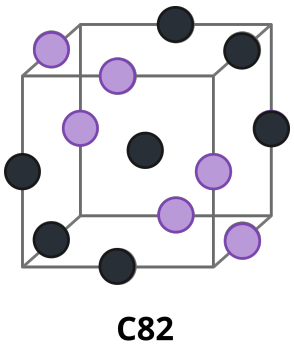

((d)) The C82 configuration ($Fm\bar{3}m$)

Figure 5.16: Enhanced configurations for the various structural models of cerium zirconium oxide and an example of the C82 configuration for the ordered structure.

5.5.4 Tetragonal Systems (and Beyond)

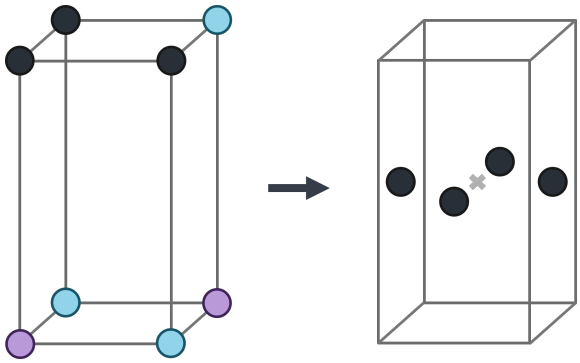

Figure 5.17: The primitive tetragonal structure, and its associated nearest neighbour configurational shape.

The final test case, though not complex, demonstrates the generalisation of the configurational analysis method to non-cubic systems. As previously described, Clapp enumerated only the configurations for the FCC and BCC crystal structures, at least in part due to their ubiquity in the field of crystallography. However, many materials demonstrate non-cubic structures - including the hexagonally close packed and orthorhombic space groups - and large lattice distortions can even lead to the formation of non-cubic phases in otherwise cubic materials. It stands to reason, therefore, that any analytical framework for the investigation of local atomic ordering effects ought to extend equally to non-cubic materials.

The primitive tetragonal system (Figure 5.17) is used in this instance as an illustration of this extension. The following simple table (Table 5.2) therefore contains the nearest neighbour configurations for the system, as provided by the software outlined above, with their composition and multiplicities. The extension of the unit cell along the 'c' unit vector direction leaves 'squares' of four nearest neighbour atoms (Figure 5.17), for which the number of enumerated configurations is only six [2]. These configurations appear to superficially 'match' those outlined in Section 5.4 for the $L1_0$ sub-lattice structure, due to the similarity in atomic planar structures.

[2] In actual fact, unit cells of greater complexity typically possess fewer nearest neighbour configurations, due to their reduced symmetry.

Tetragonal Configurations		
Clapp Configuration	No. dislike nearest neighbours	Multiplicity, W_k
	Total	
-2	3	4
-1	4	1
1	0	1
2	1	4
3	2	2
4	2	4

Table 5.2: A table enumerating the configurations for the tetragonal crystal system, with total composition and multiplicity to demonstrate associated ordering rules.

5.6 Summary

In conclusion, the above work has adapted the methods originally outlined by Clapp to provide a new and generalised analytical framework for the analysis of chemical short range order in crystalline materials. Where previously the application of Clapp configurational analysis was only applicable to the cubic systems - and only truly enumerated for the BCC and FCC structures - this analytical method has been extended to cover every space group, with associated conventions for the labelling and ordering of symmetrically equivalent atomic configurations. The new framework also resolves some of the existing complications in the ordering structure originally employed by Clapp, simplifying a number of the rules - particularly regarding the occupation of higher-order coordination shells - to allow for broad generalisation.

The use of pseudo-binary analysis, and the ability to segregate structures into their constituent sub-lattices, now also provides an accessible and intuitive method for the analysis of complex multi-component systems. The ability to select site equivalencies allows for the isolated analysis of ordering using specific chemical species (and vacancies), extending beyond the simple binary systems originally characterised by Clapp *et al.* This analysis is aided by the generation of atomic basis set files, allowing for the reconstruction and comparison of atomic structures across unique instances of modelling and simulation.

Further work is still required in the formalisation of input structures, particularly with regards to the format of .cif files. Though intended to standardise the reporting of crystallographic information, the generation of these files can vary from programme to programme, and in the extent of their content and descriptive information. This can occasionally be problematic for the handling of

dictionaries in the software described above. Resolving this concern would greatly benefit the reporting of crystallographic investigations as a whole, with the added benefit of simplifying the analysis contained herein. There are equally further avenues to explore in the presentation of configurational results, particularly with regards to the interface of the visualisation software. The statistical analysis of enhanced structures - such as providing users with an optimal degradation pathway for the most enhanced configurations as default - also remains an option.

Chapter 6

Conclusions & Future Work

6.1 Conclusions

The primary objectives of the experimental work were twofold: firstly, to determine the validity of applying total scattering techniques and Clapp configurational analysis to chemically complex metallic materials; and secondly, should this first objective be met successfully, to determine the local ordering behaviour of select multi-principal element alloys. To this end, a series of large-box atomic models have been generated from neutron total scattering data using a Reverse Monte Carlo fitting approach, and subsequently analysed for their short-range order.

As a first step towards applying these techniques to systems of greater complexity, neutron total scattering experiments were performed using a powder sample of the ternary CrCoNi MPEA from cryogenic temperatures (4.2 - 300 K) in Chapter 3. Traditional Rietveld refinement techniques and diffuse scattering analyses of the data were shown to provide an incomplete description of atomic ordering for the purportedly randomly-distributed metallic system. GSAS-II Rietveld refinement revealed a single-phase FCC structure as expected. PDFGui small-box (unit cell) modelling in particular highlighted the shortcomings of small-box modelling methods, with discrepancies between the overall fit to the PDF and the calculated structure likely demonstrating chemical ordering effects that can only be captured over larger distances. Reverse Monte Carlo large-box modelling via RMCProfile, however, demonstrated a stronger fit to PDF data using random atomic boxes constructed from $20 \times 20 \times 20$ unit cells. The impact of the scale and instrument resolution correction parameters on the quality of fitting has been demonstrated, and the 'best fit' parameter suite subsequently selected using a combination of χ^2 analysis and investigation of atomic off-site displacements. Fitting over 15 Å was shown to provide sufficient local ordering information, with

fitting over 40 Å introducing a larger degree of uncertainty in the final result.

With PDF-fitting performed successfully, it was necessary to describe and quantify the extent of ordering in the system using the generated large-box models. To this end, Clapp configurational analysis was applied to the averaged boxes, with the overall statistical enhancement of atomic configurations (β) calculated. The Clapp method was successfully applied to system of greater complexity (i.e. larger than the originally labelled binary systems), with constituent elements collapsed into three pseudo-binary cases (Cr:Ψ, Co:Ψ, and Ni:Ψ) for analysis. This method demonstrated the formation of an $L1_2$-type local structure at all temperatures: Cr and Co atoms appear to commonly segregate towards the corners of the unit cell, with Ni atoms demonstrating an approximately random distribution across the lattice. The enhancements to local nearest-neighbour atomic configurations associated with the $L1_2$ structure - i.e. the family of configurations along a degradation pathway differing by the presence of only one or two dislike atoms - also demonstrate a 'sawtooth'-like patterning, potentially suggesting a larger role for ordering within the first coordination shell. This aligns well with existing studies into the CrCoNi system, which have commonly inferred the presence of an $L1_2$-type structure in the material, and a number of which have specifically demonstrated the segregation of Cr in the bulk. There is a small amount of evidence for potential ordering changes at very low temperature (approximately 4.2 K) that may be linked to the magnetic properties of the material. Given the known behaviour of this material, the present model goes a significant way towards explaining the impressive mechanical performance of the CrCoNi alloy. Specifically, the presence of an $L1_2$ structure in the alloy likely hinders the motion of dislocations in the material, improving the strength-ductility ratio accordingly. Thus, the power of the total scattering technique and subsequent RMC refinement is demonstrated: it is possible to extract meaningful mechanical information from an atomistic model of an alloy produced via neutron diffraction.

A new methodology for fitting was also employed to check the validity of results. 'Pastel' fitting - i.e. using combined pseudo-binary boxes with recalculated pair neutron coefficients as inputs for fitting - was applied to the dataset, to determine whether the configurational results for fitting would vary in the absence of all three constituent elements. The results for this fitting were encouraging, with the $L1_2$ structure reproduced for each of the Cr:Ψ and Co:Ψ pseudo-binaries as expected. Interestingly the Ni:Ψ pseudo-binary also demonstrated an equivalent $L1_2$-type structure, perhaps due to the large variation in constituent re-calculated neutron coefficients. Given current understanding of material properties. Leading on from this work, investigations into the impact of neutron coefficients on the form of reproduced ordering demonstrated *some* role for the ratio of constituent neutron coefficients in the success of fitting. It was found that particular paired ratios of neutron coefficients are better able to reproduce known ordering in a given model, potentially indicating the unsuitability of the method in the analysis of alloys with certain compositions.

Expanding upon this work, the investigation presented in Chapter 4 introduced an incremental increase in chemical complexity to the method. Neutron total scattering data were successfully collected for a powder sample of the equimolar CrFeCoNi MPEA across a range of elevated temperatures (300 - 1273 K). Rietveld refinement of the data successfully demonstrated a single-phase FCC structure as anticipated. Small-box modelling in PDFGui once again demonstrated a disparity between the calculated fit and experimental PDF, indicating a potential chemical short-range ordering effect. Reverse Monte Carlo large-box modelling using a $20 \times 20 \times 20$ unit cell supercell produced an improved fit to data when optimised (χ^2) for the scale and instrument resolution correction fitting parameters over 15 Å.

The introduction of greater chemical complexity naturally simultaneously increases the complexity of configurational analysis. It was demonstrated that - for a four element structure - the number of pseudo-binary analyses rises to seven: Fe:Ψ, Cr-Fe:Co-Ni, Cr-Co:Fe-Ni, and Cr-Ni:Fe-Co, in addition to those outlined for the CrCoNi system. The extraction of meaningful results from this form of analysis was demonstrated successfully: of the seven pseudo-binary analyses, four were shown to possess essentially random structures; three - Cr:Ψ, Fe:Ψ and Cr-Co:Fe-Ni - showed strong statistical enhancement (β). This statistical enhancement was found to correspond once again to the $L1_2$ family of atomic configurations, with particular enhancements to the C16, C34, and C58/59 configurations. As described in the prior CrCoNi analysis, this corresponds to the segregation of atoms to the corners of the unit cell; specifically, it was found that Cr and Fe atoms preferentially segregate to the unit cell corners, with Co and Ni atoms demonstrating little preference by comparison. Instances of this segregation were shown to be distinct; Cr and Fe do not appear to share the corners of individual unit cells. This result was subsequently validated using the 'pastel' fitting method, with pseudo-binary and pseudo-ternary analyses demonstrating equivalent ordering behaviours to the original fitting.

The formation of the $L1_2$ structure was shown to match expected ordering behaviours from literature, and - given the compositional link to CrCoNi - Interestingly, analysis of fitting over 40 Årevealed 'double-minima' in the χ^2 results for the CrFeCoNi system. The quality of fit for two pairs of scale and resolution correction appeared near-equivalent, suggesting the potential existence of two 'best fit' configurational solutions. Subsequent analysis shows an approximate 'match' between the enhanced configurations in both solutions: both sets of fitting parameters demonstrate the emergence of the $L1_2$ structure, with Cr and Fe showing strong enhancements to the C16 configuration. One set of parameters, however, introduces a greater degree of uncertainty in the results, with co-enhancements to a larger number of similar configurations. Given the overall success of fitting over 15 Å by comparison - converging upon a single solution and set of fitting parameters - fitting over much larger distances for reportedly random structures remains an open question.

Finally, Chapter 5 outlined a novel, generalised methodology for the analysis of short-range order

in crystalline materials, building upon the work of Clapp *et al.* Atomic configurational labelling conventions were successfully reworked to accommodate systems of decreased symmetry, expanding from the originally outlined FCC and BCC configuration lists. Furthermore, a software package has been produced to enable analysis using standardised .cif files and the large-box outputs of RMCProfile (.rmc6f). It is now possible to analyse the ordering of non-cubic structures on their constituent sub-lattices through the specification of equivalent lattice sites, with associated statistical enhancement factors calculated per box to demonstrate enhancement. Example test cases in the form of tetragonal phases, Heusler phase transitions, ordered perovskites, and doped ceria were also presented.

6.2 Future Work

A significant portion of future work on the CrCoNi and CrFeCoNi systems would likely be dedicated to the collection of more neutron scattering data, to confirm the results established herein. In the case of the CrCoNi alloy - which demonstrated signs of a potential magnetic transition at very low temperature - this would likely involve a further cryogenic study, and a number of associated SEM/TEM and magnetic analyses. Equally, in the case of the CrFeCoNi alloy - which demonstrated a potential increase in ordering at high temperature, against expected thermodynamic behaviour - this would likely require an increased number of heating steps, to establish the point at which the system is expected to disorder fully.

Further work is also required in assessing the impact of neutron coefficients on the success of RMC fitting. Studies from the CrCoNi system showed limited capability for RMCProfile to reproduce the known ordering of boxes produced by machine-learning potentials, with the potentials themselves having produced structures that do not match those found during total scattering analysis. While it could be stated that the results taken from experimental data are likely to be 'closer' to reality, this discrepancy remains a concern. Equally, investigations into particular ratios of neutron coefficients in the system show improved agreement between datasets for particular pairs of constituent atom types, without a particularly identifiable 'pattern' or trend to assign this improvement to. It is therefore imperative that future studies address not only the gap between calculated datasets, but also the overall applicability of the method to a wider range of chemical compositions, to determine the role that variation in atomic species plays in the success of the method.

As a final experimental note, the calculation of Warren-Cowley parameters for the systems produced by RMCProfile remain an open area for investigation. The spread of calculated values across literature remains a concern for researchers - though improvements in machine-learning methods are closing this gap - and therefore requires further analysis. Indeed, trends in the Warren-Cowley parameters calculated for particular atomic pairs and their associated pair neutron coefficients

appear to show weaker ordering correlations for very high or very low neutron coefficients, which could theoretically skew structural results if found to be consistently true.

Though the novel analytical framework presented above is robust, there are a number of future improvements to consider. Basic quality of life updates to the software could improve the overall experience of users. The files are currently separated into individual python batching scripts - for high-throughput, rapid analysis of many configurational studies - and a separate, contained batch file that runs the software through the terminal for single analyses. Both options could be made more intuitive through the appropriate labelling of filenames, sub-lattices and pseudo-binaries in the generated files; users are, for instance, thus far expected to establish which pseudo-binary corresponds to which atomic species themselves. Making this more intuitive for the user is likely to increase adoption of the method. The latter terminal option also provides all three scripts (i.e. the generation of configurational dictionaries, configurational analysis of .rmc6f boxes, and a configurational visualiser) as interactive commands, and allows for the interactive selection of files and equivalent atomic positions. This could be substantially improved through the creation of a properly formatted GUI, with a file selector, that could be downloaded for any OS system. This would also provide more options for the visualiser, which at present relies on python graphing through the terminal.

The application of the above methods to a wider range of materials over large compositional spaces will, naturally, improve the understanding of their efficacy and repeatability. A natural next step for investigation would be the CrMnFeCoNi quinary MPEA, and associated transition/refractory metal derivatives. Many of these alloys are as yet unexplored for their local ordering behaviour, with many of their unique or exceptional properties remaining unexplained. These studies would therefore begin to bridge gaps in the wider research community, and would act to assess the suitability of the RMC fitting and pseudo-binary Clapp methods for systems of even greater chemical complexity.

Appendix A

Appendix

A.1 RMCProfile Fitting Regimes

In order to identify the best set of fitting parameters (i.e. the scale and resolution correction parameters that provide the lowest χ^2-fit to the data), a grid-search is performed. An analysis of 10 scale and 10 resolution correction parameters therefore produces 100 large-box simulations, each with some pairwise combination of parameters.

Multiple fitting regimes are performed during RMCProfile analysis, in order to increase confidence in the produced large box model. *Grey* fitting is performed by constraining the degrees of freedom when fitting using a *single atom type*. A good fit in this regime would likely indicate that the data is well fitted as a random distribution of constituent elements, as the absence of chemical complexity has no impact on the final result. *Colour* fitting reintroduces all three constituent elements, and will ideally provide a physically valid reconstruction of atomic ordering from experimentation. *Pastel* fitting then reduces the input boxes into their constituent pseudo-binary representations (i.e. two elements, Cr:Ψ, Co:Ψ and Ni:Ψ) as a subsequent validation of the pseudo-binary analyses performed on the *full colour* boxes. This final regime is performed identically to the *colour* fitting, with fewer constituent elements.

A.1.1 Grey atom runs

For the CrCoNi data, *grey* (single atom) RMC refinements were carried out as follows:

1. $20 \times 20 \times 20$ *fcc* supercells were produced using a single, arbitrary atom type (nickel, 'Ni') with averaged properties. A small gaussian displacement of atoms away from their idealised

lattice positions are applied.

2. Total scattering functions $G(r)$ and $F(Q)$ were calculated and processed using SToG (accounting for offsets). Importantly, some of the parameters in PDFGui were approximately equivalent to fitted parameters in RMCProfile: it is possible to use the scale value from PDFGui as an initial estimate for the scale parameter in RMC fitting, providing a reasonable 'window' within which the χ^2 minimum for that system might be anticipated. The scale factor was therefore varied from 0.92-1.02 in steps of 0.01, and $Q_{\max} = 36$ Å.

3. RMC refinements were performed, fitting to the normalised $D(r)$ using 2,000,000 translational moves. Two data sets were used as input: a) normalised $D(r)$ to 15 Å, and b) the first peak in the $D(r)$. Limiting the fit to 15 Å helped to correct for high Q resolution effects whilst capturing short-range order effects to a sufficient distance. The Q_{damp} term from PDFGui fitting was then used as an approximation for the instrument resolution correction parameter in RMCProfile. Both perform high-r corrective roles to account for noise in the high Q-region of the scattering function, providing an equivalent initial value estimate. The resolution correction parameter was therefore varied from 0.02-0.03 in steps of 0.001.

4. By considering the resultant χ^2 values for each refinement, suitable scale and resolution correction factor ranges were selected for further investigation.

A.1.2 Colour atom runs

For the CrCoNi data, *colour* (all constituent elements) RMC refinements were performed as follows:

1. An initial grey run was performed. $20 \times 20 \times 20$ *fcc* supercells were produced using a single, arbitrary atom type (nickel, 'Ni') with averaged properties. A small gaussian displacement of atoms away from their idealised lattice positions was applied.

2. Total scattering functions $G(r)$ and $F(Q)$ were calculated and processed using SToG (accounting for offsets). Importantly, some of the parameters in PDFGui were approximately equivalent to fitted parameters in RMCProfile: it is possible to use the scale value from PDFGui as an initial estimate for the scale parameter in RMC fitting, providing a reasonable 'window' within which the χ^2 minimum for that system might be anticipated. The scale factor was therefore varied from 0.92-1.02 in steps of 0.01, and $Q_{\max} = 36$ Å.

3. RMC refinements were performed, fitting to the normalised $D(r)$ using 2,000,000 translational moves. Two data sets were used as input: a) normalised $D(r)$ to 15 Å, and b) the first peak in the $D(r)$.

4. The supercell is then 'updated' to contain all three atom types in the system (chromium, cobalt, nickel) distributed randomly according to their atomic fraction (0.2582 Cr - 0.3488 Co - 0.3930 Ni), with the newly refined offsite displacements and associated properties. Refinements now require an input range of resolution correction parameters. The Q_{damp} term from PDFGui fitting could then be used as an approximation for the instrument resolution correction parameter in RMCProfile. Both perform high-r corrective roles to account for noise in the high Q-region of the scattering function, providing an equivalent initial value estimate. For the purposes of this experiment, therefore, a range of 0.02-0.03 in increments of 0.001 was selected, bringing the total number of simulations to 100 per colour run.

5. Boxes were then refined for a further 8,000,000 moves, allowing both translations and the swapping of atomic species. Swaps were performed with a probability of 0.2 per atomic species, such that an overall 3:2 swap to translation ratio was achieved.

6. By considering the resultant χ^2 values for each refinement, a suitable scale and resolution correction factor were selected for further investigation.

7. Once an appropriate suite of scale and resolution correction parameter values was selected, each refinement was performed identically on 40 *fcc* supercells ($20 \times 20 \times 20$ unit cells) for averaging.

A.1.3 Pastel atom runs

For the CrCoNi data, *pastel* (pseudo-binary reduction) RMC refinements were performed as follows:

1. An initial grey run was performed. $20 \times 20 \times 20$ *fcc* supercells were produced using a single, arbitrary atom type (nickel, 'Ni') with averaged properties. A small gaussian displacement of atoms away from their idealised lattice positions was applied.

2. Total scattering functions $G(r)$ and $F(Q)$ were calculated and processed using SToG (accounting for offsets); the best scale factor from prior colour fitting was used in this instance (0.95), and $Q_{\mathrm{max}} = 36$ Å.

3. RMC refinements were performed, fitting to the normalised $D(r)$ using 2,000,000 translational moves. Two data sets were used as input: a) normalised $D(r)$ to 15 Å, and b) the first peak in the $D(r)$.

4. The supercell was then 'updated' to contain atom types according to the possible pseudo-binary reductions in the system (in this instance, Cr:Ψ, Co:Ψ, Ni:Ψ). These atom types were distributed randomly across newly refined atomic positions according to their atomic fractions, with Ψ combined atom types possessing the averaged properties of their constituent elements. For the purposes of this experiment, the best fit resolution correction parameter value from colour fitting was found to be 0.029.

5. Boxes were then refined for a further 8,000,000 moves, allowing both translations and the swapping of atomic species. Swaps were performed with a probability of 0.2 per atomic species, such that an overall 2:3 swap to translation ratio was achieved.

6. By considering the resultant χ^2 values for each refinement, a suitable scale and resolution correction factor were selected for further investigation.

7. Once an appropriate suite of scale and resolution correction parameter values was selected, each refinement was performed identically on 10 *fcc* supercells ($20 \times 20 \times 20$ unit cells) for averaging.

A.2 Analysis Code

The software produced for the framework in Chapter 5 may be found at:

`https://github.com/BJolly-97/Gen_Config`

Bibliography

[1] E. P. George, D. Raabe, and R. O. Ritchie, "High-entropy alloys," *Nature reviews materials*, vol. 4, no. 8, pp. 515–534, 2019.

[2] I. Toda-Caraballo, J. S. Wróbel, S. L. Dudarev, D. Nguyen-Manh, and P. E. Rivera-Díaz-Del-Castillo, "Interatomic spacing distribution in multicomponent alloys," *Acta Materialia*, vol. 97, pp. 156–169, 2015, ISSN: 13596454. DOI: 10.1016/j.actamat.2015.07.010. [Online]. Available: http://dx.doi.org/10.1016/j.actamat.2015.07.010.

[3] Y. Rao and W. A. Curtin, "Analytical models of short-range order in FCC and BCC alloys," *Acta Materialia*, vol. 226, Mar. 2022, ISSN: 13596454. DOI: 10.1016/j.actamat.2022.117621.

[4] L. R. Owen, H. Y. Playford, H. J. Stone, and M. G. Tucker, "A new approach to the analysis of short-range order in alloys using total scattering," *Acta Materialia*, vol. 115, pp. 155–166, Aug. 2016, ISSN: 13596454. DOI: 10.1016/j.actamat.2016.05.031.

[5] S. Guo et al., "Overcoming strength-ductility trade-off in high-entropy alloys by tuning chemical short-range order and grain size," *Intermetallics*, vol. 150, p. 107 693, 2022.

[6] Y. Li et al., "Chemical ordering effect on the radiation resistance of a CoNiCrFeMn high-entropy alloy," *Computational Materials Science*, vol. 214, p. 111 764, 2022.

[7] T. Rouxel, "Elastic properties and short-to medium-range order in glasses," *Journal of the American Ceramic Society*, vol. 90, no. 10, pp. 3019–3039, 2007.

[8] Z. Lei et al., "Enhanced strength and ductility in a high-entropy alloy via ordered oxygen complexes," *Nature*, vol. 563, no. 7732, pp. 546–550, 2018.

[9] S. Chen et al., "Simultaneously enhancing the ultimate strength and ductility of high-entropy alloys via short-range ordering," *Nature communications*, vol. 12, no. 1, p. 4953, 2021.

[10] R. Sabban, K. Dash, S. Suwas, and B. Murty, "Strength–ductility synergy in high entropy alloys by tuning the thermo-mechanical process parameters: A comprehensive review," *Journal of the Indian Institute of Science*, vol. 102, no. 1, pp. 91–116, 2022.

[11] E. J. Pickering and N. G. Jones, "High-entropy alloys: A critical assessment of their founding principles and future prospects," *International Materials Reviews*, vol. 61, pp. 183–202, 3 2016, ISSN: 17432804. DOI: 10.1080/09506608.2016.1180020.

[12] J. W. Yeh et al., "Nanostructured high-entropy alloys with multiple principal elements: Novel alloy design concepts and outcomes," *Advanced Engineering Materials*, vol. 6, pp. 299–303, 5 2004, ISSN: 14381656. DOI: 10.1002/adem.200300567.

[13] B. Cantor, I. T. Chang, P. Knight, and A. J. Vincent, "Microstructural development in equiatomic multicomponent alloys," *Materials Science and Engineering: A*, vol. 375-377, pp. 213–218, 1-2 SPEC. ISS. Jul. 2004, ISSN: 09215093. DOI: 10.1016/j.msea.2003.10.257.

[14] J. Chen et al., "A review on fundamental of high entropy alloys with promising high–temperature properties," *Journal of Alloys and Compounds*, vol. 760, pp. 15–30, 2018, ISSN: 09258388. DOI: 10.1016/j.jallcom.2018.05.067. [Online]. Available: https://doi.org/10.1016/j.jallcom.2018.05.067.

[15] K.-Y. Tsai, M.-H. Tsai, and J.-W. Yeh, "Sluggish diffusion in Co-Cr-Fe-Mn-Ni high-entropy alloys," *Acta Materialia*, vol. 61, no. 13, pp. 4887–4897, 2013.

[16] J. B. Seol et al., "Mechanically derived short-range order and its impact on the multi-principal-element alloys," *Nature communications*, vol. 13, no. 1, p. 6766, 2022.

[17] R. D. Shannon, "Revised effective ionic radii and systematic studies of interatomic distances in halides and chalcogenides," *Foundations of Crystallography*, vol. 32, no. 5, pp. 751–767, 1976.

[18] N. Argaman and G. Makov, "Density functional theory: An introduction," *American Journal of Physics*, vol. 68, no. 1, pp. 69–79, 2000.

[19] C. Jiang, C. Wolverton, J. Sofo, L. Q. Chen, and Z. K. Liu, "First-principles study of binary BCC alloys using special quasirandom structures," *Physical Review B - Condensed Matter and Materials Physics*, vol. 69, 21 Jun. 2004, ISSN: 01631829. DOI: 10.1103/PhysRevB.69.214202.

[20] C. Huang and B. M. Rubenstein, "Machine Learning Diffusion Monte Carlo Forces," *Journal of Physical Chemistry A*, vol. 127, pp. 339–355, 1 Jan. 2023, ISSN: 15205215. DOI: 10.1021/acs.jpca.2c05904.

[21] K. Ryczko, J. T. Krogel, and I. Tamblyn, "Machine Learning Diffusion Monte Carlo Energies," *Journal of Chemical Theory and Computation*, vol. 18, pp. 7695–7701, 12 Dec. 2022, ISSN: 15499626. DOI: 10.1021/acs.jctc.2c00483.

[22] Y. Wu et al., "Short-range ordering and its effects on mechanical properties of high-entropy alloys," *Journal of Materials Science & Technology*, vol. 62, pp. 214–220, 2021.

[23] J. Gryboś, P. Indyka, and Z. Sojka, "Morphology, structure, and chemical composition: Transmission electron microscopy and elemental analysis," in *Metal Oxide Nanoparticles*. Wiley, Sep. 2021, pp. 349–382. DOI: 10.1002/9781119436782.ch10.

[24] V. Dolique, A.-L. Thomann, P. Brault, Y. Tessier, and P. Gillon, "Thermal stability of AlCoCrCuFeNi high entropy alloy thin films studied by in-situ XRD analysis," *Surface and Coatings Technology*, vol. 204, no. 12-13, pp. 1989–1992, 2010.

[25] F. Walsh, M. Zhang, R. O. Ritchie, A. M. Minor, and M. Asta, "Extra electron reflections in concentrated alloys do not necessitate short-range order," *Nature Materials*, vol. 22, pp. 926–929, 8 Aug. 2023, ISSN: 1476-1122. DOI: 10.1038/s41563-023-01570-9. [Online]. Available: https://www.nature.com/articles/s41563-023-01570-9.

[26] B. K. Teo, *EXAFS: basic principles and data analysis*. Springer Science & Business Media, 2012, vol. 9.

[27] H. Joress et al., *Why is EXAFS for complex concentrated alloys so hard? challenges and opportunities for measuring ordering with X-ray absorption spectroscopy*, Nov. 2023. DOI: 10.1016/j.matt.2023.09.010.

[28] A. Iglesias-Juez, G. L. Chiarello, G. S. Patience, and M. O. Guerrero-Pérez, "Experimental methods in chemical engineering: X-ray absorption spectroscopy—XAS, XANES, EXAFS," *The Canadian Journal of Chemical Engineering*, vol. 100, no. 1, pp. 3–22, 2022.

[29] C. Martineau, J. Senker, and F. Taulelle, "NMR crystallography," *Annual Reports on NMR Spectroscopy*, vol. 82, pp. 1–57, 2014.

[30] D. L. Bryce, "NMR crystallography: Structure and properties of materials from solid-state nuclear magnetic resonance observables," *IUCrJ*, vol. 4, no. 4, pp. 350–359, 2017.

[31] L. R. Owen, "The analysis of local structural effects in alloys using total scattering and reverse Monte Carlo techniques," Ph.D. dissertation, Apollo - University of Cambridge Repository, 2018. DOI: 10.17863/CAM.20814. [Online]. Available: https://www.repository.cam.ac.uk/handle/1810/273748.

[32] W. Lefebvre, F. Vurpillot, and X. Sauvage, *Atom probe tomography: put theory into practice*. Academic Press, 2016.

[33] M. P. Moody, B. Gault, L. T. Stephenson, D. Haley, and S. P. Ringer, "Qualification of the tomographic reconstruction in atom probe by advanced spatial distribution map techniques," *Ultramicroscopy*, vol. 109, no. 7, pp. 815–824, 2009.

[34] D. A. Keen, "Total scattering and the pair distribution function in crystallography," *Crystallography Reviews*, vol. 26, no. 3, pp. 143–201, 2020.

[35] L. Owen, H. Playford, H. Stone, and M. Tucker, "A new approach to the analysis of short-range order in alloys using total scattering," *Acta Materialia*, vol. 115, pp. 155–166, 2016.

[36] L. R. Owen and N. G. Jones, "Lattice distortions in high-entropy alloys," *Journal of Materials Research*, vol. 33, no. 19, pp. 2954–2969, 2018. DOI: 10.1557/jmr.2018.322.

[37] J. Cowley, "Short-range order and long-range order parameters," *Physical Review*, vol. 138, no. 5A, A1384, 1965.

[38] P. C. Clapp, "Atomic configurations in binary alloys," *Physical Review B*, vol. 4, pp. 255–270, 2 1971.

[39] L. R. Owen, H. Y. Playford, H. J. Stone, and M. G. Tucker, "Analysis of short-range order in Cu_3Au using X-ray pair distribution functions," *Acta Materialia*, vol. 125, pp. 15–26, Feb. 2017, ISSN: 13596454. DOI: 10.1016/j.actamat.2016.11.048.

[40] W. Fu et al., "Cryogenic mechanical behaviors of CrMnFeCoNi high-entropy alloy," *Materials Science and Engineering: A*, vol. 789, Jul. 2020, ISSN: 09215093. DOI: 10.1016/j.msea.2020.139579.

[41] L. Yang et al., "High He-ion irradiation resistance of CrMnFeCoNi high-entropy alloy revealed by comparison study with ni and 304ss," *Journal of Materials Science and Technology*, vol. 35, pp. 300–305, 3 Mar. 2019, ISSN: 10050302. DOI: 10.1016/j.jmst.2018.09.050.

[42] M. Mizuno, K. Sugita, and H. Araki, "Prediction of short-range order in CrMnFeCoNi high-entropy alloy," *Results in Physics*, vol. 34, Mar. 2022, ISSN: 22113797. DOI: 10.1016/j.rinp.2022.105285.

[43] H. Luo et al., "A strong and ductile medium-entropy alloy resists hydrogen embrittlement and corrosion," *Nature Communications*, vol. 11, 1 Dec. 2020, ISSN: 20411723. DOI: 10.1038/s41467-020-16791-8.

[44] S. S. Sohn et al., "Ultrastrong medium-entropy single-phase alloys designed via severe lattice distortion," *Advanced Materials*, vol. 31, 8 Feb. 2019, ISSN: 15214095. DOI: 10.1002/adma.201807142.

[45] S. Chen et al., "Chemical-affinity disparity and exclusivity drive atomic segregation, short-range ordering, and cluster formation in high-entropy alloys," *Acta Materialia*, vol. 206, Mar. 2021, ISSN: 13596454. DOI: 10.1016/j.actamat.2021.116638.

[46] X. Wang, H. Huang, J. Shi, H. Y. Xu, and D. Q. Meng, *Recent progress of tungsten-based high-entropy alloys in nuclear fusion*, Jun. 2021. DOI: 10.1007/s42864-021-00092-8.

[47] B. Zhang, J. Ding, and E. Ma, "Chemical short-range order in body-centered-cubic TiZrHfNb high-entropy alloys," *Applied Physics Letters*, vol. 119, 20 Nov. 2021, ISSN: 00036951. DOI: 10.1063/5.0069417.

[48] Y. Tong et al., "Evolution of local lattice distortion under irradiation in medium- and high-entropy alloys," *Materialia*, vol. 2, pp. 73–81, Oct. 2018, ISSN: 25891529. DOI: 10.1016/j.mtla.2018.06.008.

[49] L. R. Owen, N. G. Jones, H. J. Stone, and H. Y. Playford, "Separation of static and dynamic displacements in the CrMnFeCoNi high entropy alloy," *Acta Materialia*, vol. 262, Jan. 2024, ISSN: 13596454. DOI: 10.1016/j.actamat.2023.119164.

[50] P. Thirathipviwat, S. Sato, G. Song, J. Bednarcik, K. Nielsch, and J. Han, "Compositional complexity dependence of lattice distortion in FeNiCoCrMn high entropy alloy system," *Materials Science and Engineering: A*, vol. 823, Aug. 2021, ISSN: 09215093. DOI: 10.1016/j.msea.2021.141775.

[51] M. M. Nygård et al., "Local order in high-entropy alloys and associated deuterides – a total scattering and Reverse Monte Carlo study," *Acta Materialia*, vol. 199, pp. 504–513, 2020, ISSN: 13596454. DOI: 10.1016/j.actamat.2020.08.045.

[52] W. E. I. Guo, W. Dmowski, J.-y. Noh, P. Rack, and P. K. Liaw, "Local atomic structure of a high-entropy alloy : An X-Ray and neutron scattering study," *Metall Mater Trans*, vol. 44, pp. 1994–1997, 2013. DOI: 10.1007/s11661-012-1474-0.

[53] R. I. Smith et al., "The upgraded Polaris powder diffractometer at the ISIS neutron source," *Review of Scientific Instruments*, vol. 90, 11 Nov. 2019, ISSN: 10897623. DOI: 10.1063/1.5099568.

[54] R. B. Toby and B. H. V. Dreele, "GSAS-II: The genesis of a modern open-source all purpose crystallography software package," *Journal of Applied Crystallography*, vol. 46, pp. 544–549, 2 2013.

[55] R. A. Young, *The rietveld method*. International union of crystallography, 1993, vol. 5.

[56] A. Soper, "GudrunN and GudrunX: Programs for correcting raw neutron and X-ray diffraction data to differential scattering cross section," *RAL Report RAL-TR-2011-013*, 2011. [Online]. Available: http://purl.org/net/epubs/work/56240.

[57] M. G. Tucker, D. A. Keen, M. T. Dove, A. L. Goodwin, and Q. Hui, "RMCProfile: Reverse Monte Carlo for polycrystalline materials," *Journal of Physics Condensed Matter*, vol. 19, 33 2007, ISSN: 09538984. DOI: 10.1088/0953-8984/19/33/335218.

[58] C. L. Farrow et al., "PDFgui user guide," *PDFGUI User Guide*, April 2009.

[59] W. A. Sławiński et al., "RMCProfile7: Reverse Monte Carlo for multiphase systems," *Applied Crystallography*, vol. 57, no. 4, pp. 1251–1262, 2024.

[60] B. Yin, S. Yoshida, N. Tsuji, and W. A. Curtin, "Yield strength and misfit volumes of NiCoCr and implications for short-range-order," *Nature Communications*, vol. 11, 1 Dec. 2020, ISSN: 20411723. DOI: 10.1038/s41467-020-16083-1.

[61] L. Zhou et al., "Atomic-scale evidence of chemical short-range order in CrCoNi medium-entropy alloy," *Acta Materialia*, vol. 224, Feb. 2022, ISSN: 13596454. DOI: 10.1016/j.actamat.2021.117490.

[62] B. Uzer et al., "On the mechanical response and microstructure evolution of NiCoCr single crystalline medium entropy alloys," *Materials Research Letters*, vol. 6, pp. 442–449, 8 Aug. 2018, ISSN: 21663831. DOI: 10.1080/21663831.2018.1478331.

[63] Z. Zhang et al., "Dislocation mechanisms and 3d twin architectures generate exceptional strength-ductility-toughness combination in CrCoNi medium-entropy alloy," *Nature communications*, vol. 8, no. 1, p. 14 390, 2017.

[64] R. Zhang et al., "Short-range order and its impact on the CrCoNi medium-entropy alloy," *Nature*, vol. 581, pp. 283–287, 7808 May 2020, ISSN: 14764687. DOI: 10.1038/s41586-020-2275-z.

[65] F. G. Coury, C. Miller, R. Field, and M. Kaufman, "On the origin of diffuse intensities in FCC electron diffraction patterns," *Nature*, vol. 622, pp. 742–747, 7984 Oct. 2023, ISSN: 0028-0836. DOI: 10.1038/s41586-023-06530-6. [Online]. Available: https://www.nature.com/articles/s41586-023-06530-6.

[66] V. P. Bacurau et al., "Comprehensive analysis of ordering in cocrni and crni2 alloys," *Nature Communications*, vol. 15, 1 Dec. 2024, ISSN: 20411723. DOI: 10.1038/s41467-024-52018-w.

[67] K. Sheriff, Y. Cao, T. Smidt, and R. Freitas, "Quantifying chemical short-range order in metallic alloys," *Proceedings of the National Academy of Sciences*, vol. 121, no. 25, e2322962121, 2024.

[68] C. D. Woodgate, D. Hedlund, L. Lewis, and J. B. Staunton, "Interplay between magnetism and short-range order in medium-and high-entropy alloys: CrCoNi, CrFeCoNi, and CrMnFeCoNi," *Physical Review Materials*, vol. 7, no. 5, p. 053 801, 2023.

[69] O. Arnold et al., "Mantid—data analysis and visualization package for neutron scattering and SR experiments," *Nuclear Instruments and Methods in Physics Research Section A: Accelerators, Spectrometers, Detectors and Associated Equipment*, vol. 764, pp. 156–166, 2014, ISSN: 0168-9002. DOI: https://doi.org/10.1016/j.nima.2014.07.029. [Online]. Available: http://www.sciencedirect.com/science/article/pii/S0168900214008729.

[70] T. Cao et al., "Dynamic deformation behaviors and mechanisms of CoCrFeNi high-entropy alloys," *Acta Materialia*, vol. 260, p. 119 343, 2023.

[71] A. Tamm, A. Aabloo, M. Klintenberg, M. Stocks, and A. Caro, "Atomic-scale properties of Ni-based FCC ternary, and quaternary alloys," *Acta Materialia*, vol. 99, pp. 307–312, 2015.

[72] Q. He and Y. Yang, "On lattice distortion in high entropy alloys," *Frontiers in Materials*, vol. 5, Jul. 2018, ISSN: 22968016. DOI: 10.3389/fmats.2018.00042.

[73] C. Niu, A. Zaddach, C. Koch, and D. Irving, "First principles exploration of near-equiatomic NiFeCrCo high entropy alloys," *Journal of Alloys and Compounds*, vol. 672, pp. 510–520, 2016.

[74] T. Fukushima, H. Katayama-Yoshida, K. Sato, M. Ogura, R. Zeller, and P. H. Dederichs, "Local energies and energy fluctuations—applied to the high entropy alloy CrFeCoNi," *Journal of the Physical Society of Japan*, vol. 86, no. 11, p. 114 704, 2017.

[75] B. Schönfeld et al., "Local order in cr-fe-co-ni: Experiment and electronic structure calculations," *Physical Review B*, vol. 99, 1 Jan. 2019, ISSN: 24699969. DOI: 10.1103/PhysRevB.99.014206.

[76] P. J. Webster, "Heusler alloys," *Contemporary Physics*, vol. 10, no. 6, pp. 559–577, 1969.

[77] K. Elphick et al., "Heusler alloys for spintronic devices: Review on recent development and future perspectives," *Science and technology of advanced materials*, vol. 22, no. 1, pp. 235–271, 2021.

[78] S. Maier, S. Denis, S. Adam, J.-C. Crivello, J.-M. Joubert, and E. Alleno, "Order-disorder transitions in the fe2val heusler alloy," *Acta Materialia*, vol. 121, pp. 126–136, 2016.

[79] G. King and P. M. Woodward, "Cation ordering in perovskites," *Journal of Materials Chemistry*, vol. 20, pp. 5785–5796, 28 Jul. 2010, ISSN: 13645501. DOI: 10.1039/b926757c.

[80] E. W. McFarland and H. Metiu, "Catalysis by doped oxides," *Chemical reviews*, vol. 113, no. 6, pp. 4391–4427, 2013.

[81] A. Summer et al., "Order and disorder in cerium-rich ceria-zirconia solid solutions revealed from reverse Monte Carlo analysis of neutron and X-ray total scattering," *APL Materials*, vol. 11, 3 Mar. 2023, ISSN: 2166532X. DOI: 10.1063/5.0139567.